

The Adsorption and Charge-Transfer Dynamics of Model Dye-Sensitised Solar Cell Surfaces

by Louise Charlotte Mayor, MSci. (Hons.)

Thesis submitted to The University of Nottingham
for the degree of Doctor of Philosophy, August 2009

Contents

1	Dye-sensitised solar cells	1
1.1	Introduction	1
1.2	The need for cost-effective photovoltaic cells	2
1.3	The Grätzel cell	2
1.4	The McFarland and Tang cell	11
1.5	Future prospects for dye-sensitised solar cells	12
1.6	Topics researched in this thesis	14
2	Synchrotron radiation	16
2.1	Introduction	16
2.2	Synchrotron layout	18
2.3	Wigglers and undulators	19
2.4	Beamline I511	21
2.5	End station I511-1	23
2.6	The importance of grazing incidence	25
3	Adsorption of molecules to surfaces	27
3.1	Introduction	27
3.2	Photoemission spectroscopy	29
3.3	Near-edge x-ray absorption fine structure spectroscopy	47
3.4	X-ray emission spectroscopy	50
3.5	Density functional theory	53
3.6	Scanning tunnelling microscopy	56
4	Molecule-to-substrate charge transfer	59
4.1	Introduction	59
4.2	Energy level alignment	61
4.3	Core-level resonant electron spectroscopy	65
4.4	Core-level resonant x-ray emission spectroscopy	75

5	Ultra-high vacuum electrospray deposition	80
5.1	Background	80
5.2	Motivation	81
5.3	Apparatus and physical processes	82
5.4	Summary	89
6	N3 on TiO₂(110)	91
6.1	Introduction	91
6.2	Method	94
6.3	Results	97
6.4	Conclusions	118
7	N3 on Au(111)	122
7.1	Introduction	122
7.2	Method	123
7.3	Results	125
7.4	Conclusions	140
8	Summary	142
8.1	List of publications	145
8.2	List of acronyms	148
	List of Figures	149
	References	154

Abstract

In this thesis, the dye molecule cis-bis(isothiocyanato)bis(2,2'-bipyridyl-4,4'-dicarboxylato)-ruthenium(II) (N3) is studied on the rutile $\text{TiO}_2(110)$ and Au(111) surfaces. The molecules were deposited onto the surfaces using an ultra-high vacuum (UHV) electrospray deposition system. Thermally labile molecules such as N3 cannot be deposited using the typical method of thermal sublimation, so development of this deposition technique was a necessary step for entirely *in situ* experiments.

The geometric and electronic structure of the samples are characterised using core-level and valence band photoemission spectroscopy, x-ray absorption fine structure spectroscopy, density functional theory, resonant x-ray emission spectroscopy and scanning tunnelling microscopy. These reveal that N3 bonds to $\text{TiO}_2(110)$ by deprotonation of the carboxyl groups of one bi-isonicotinic acid ligand so that its oxygen atoms bond to titanium atoms of the substrate, and one of the thiocyanate groups bonds via a sulphur atom to an oxygen atom of the substrate. N3 bonds to Au(111) via sulphur atoms with no deprotonation of the carboxylic groups, and at low coverages decorates the Au(111) herringbone reconstruction. For N3 on TiO_2 , a consideration of the energetics in relation to optical absorption is used to identify the main photoexcitation channel between occupied and unoccupied molecular orbitals in this system, and also to quantify the relative binding energies of core and valence excitons. For N3 on Au(111), the energetics show that the highest occupied molecular orbital overlaps with the Au conduction band.

The transfer of charge between the N3 molecule and the $\text{TiO}_2(110)$ and Au(111) surfaces was studied using resonant photoemission spectroscopy and resonant x-ray emission spectroscopy. These techniques, combined with knowledge gained about the geometric and electronic structure, are used to determine the locations and electronic levels of N3 from which charge is readily transferred to the substrate. The core-hole clock implementation of resonant photoemission spectroscopy is used to reveal that electron delocalisation from N3 to $\text{TiO}_2(110)$ occurs within 16 femtoseconds.

Acknowledgements

First and foremost I would like to thank my supervisor James O’Shea. Not only did he provide me with an interesting and rewarding project, but he has been supportive throughout and always ready with a smile to answer my many questions.

Much of my experimental work was carried out at synchrotrons. Thanks to James O’Shea, Ben Taylor, Janine Grattage, Achim Schnadt and Karina Schulte for patiently explaining to me the principles behind synchrotron techniques and how to apply them without causing something to explode, receiving an electric shock, or even worse, causing the wrath of other users should you shut the whole thing down by mistake. Thanks go to Graziano Magnano, Anna Rienzo and Chris Satterley, along with the aforementioned, for their excellent company and hard work during beam-times. I would also like to thank Alex Saywell for his scanning tunnelling microscopy work included in Chapter 7.

The majority of my PhD was spent in Nottingham in the company of the Nano-science group. Thanks to members of the group, past and present, who have always been willing to discuss or explain some physical concept, but more importantly are happy to sit and chat for a while over a cup of tea at work, or a pint of beer at the pub. In particular I would like to thank Alex Saywell, Adam Sweetman, Chris Martin, Andy Stannard, Nick Smith, and Andy Pollard.

A happy worker is a good worker, and I couldn’t have managed to do this PhD without the sterling support of friends, and many a fun time spent in their company. In particular I would like to acknowledge my appreciation to Claire Stevenson, Beth Hughes, Kim Cresswell, Robin Scott, Laura Martin, Mary Stephenson, Maria Tito, Kate Prayle, Jon Grattage, James Leggett, Simon White, Charlotte Eichler, Ricky Chaggar, Dave Smith, James Clewett, Hayley Pollard, Gemma Whiley, Emma Williams and Nick Hutton.

Finally I would like to thank my mum, dad and brother David for their ongoing love and support.

CHAPTER 1

Dye-sensitised solar cells

1.1 Introduction

Solar cells are devices that absorb electromagnetic radiation from the sun and transform it into electrical energy. The energy is converted via the photovoltaic effect, so solar cells are also known as photovoltaic cells. Traditionally, a narrow band gap semiconductor such as silicon is used in such a device. A *dye-sensitised solar cell* (DSC) is a more recent invention in which a wide band gap semiconductor such as titanium dioxide is made light-sensitive by staining its surface with dye. In this work, DSC surfaces are investigated using mainly experimental methods. It is at the DSC surface that light is absorbed and photovoltaic energy conversion takes place. A greater understanding of the physics at these surfaces gives an insight into why the currently most efficient DSCs work so well, and could lead to finding more efficient DSCs in the future.

In this chapter dye-sensitised solar cells are introduced in a general context for the interest of the reader, before explaining how they work and then outlining the particular versions studied here. In the second chapter synchrotron radiation is introduced, as it forms the foundation of many of the experimental techniques which are used in the work. In the third and fourth chapters, experimental and theoretical techniques are described that have been used here to study the adsorption (bonding) of molecules to surfaces and to study the transfer of charge between a molecule and a surface to which it is adsorbed. In chapter five the technique we have used to deposit molecules

onto surfaces – ultra-high vacuum electrospray deposition – is explained. It is this technique, developed at Nottingham, that has allowed us to prepare DSC surfaces at ultra-high vacuum for the first time. In chapters six and seven, the results of the work carried out are presented, and in the final chapter this thesis is summarised.

1.2 The need for cost-effective photovoltaic cells

Generating electricity using solar cells is a popular method compared with contentious renewable energy sources such as wind and hydroelectric, and the polluting non-renewables of oil, coal, gas and nuclear. So it may come as a surprise that solar energy contributes less than 0.1% to the world's current electricity use, especially as the sun radiates approximately 100,000 TW of energy onto the earth's surface per year (which is $\sim 10,000$ times more than the 13 TW we currently use).[1] The problem that holds back a solar energy revolution is the cost-efficiency of commercial solar cells. Although these have reached high efficiencies of 12-17%,[1] the cost of US\$0.25-0.65 per kWh of energy is not economically competitive with the price of utility grid electricity at \$0.05 per kWh. The price of solar-grade silicon remains high, causing devices based on crystalline and polycrystalline silicon to cost above \$5 per watt of generating capacity.[1] This would have to drop to \$1 per watt to compete with grid electricity.[1] The driving forces of finite oil, coal and gas supplies, combined with environmental concerns over the greenhouse effect, maintain the push to develop renewable energy sources which will one day need to support the world's energy use. In the solar cell industry, with silicon prices remaining high, this has stimulated research into solar cells using different materials and consequently, in some cases, different operating principles.

1.3 The Grätzel cell

Along with the high cost of silicon, a significant disadvantage of using silicon in a solar cell is that it is unstable against photocorrosion,[2] i.e. it degrades in sunlight over time. A solution to both of these problems would be to use a cheap, wide band

gap semiconductor. The size of the band gap is a measure of the chemical bond strength in a semiconductor,[2] and hence the wider the band gap the more stable the material.

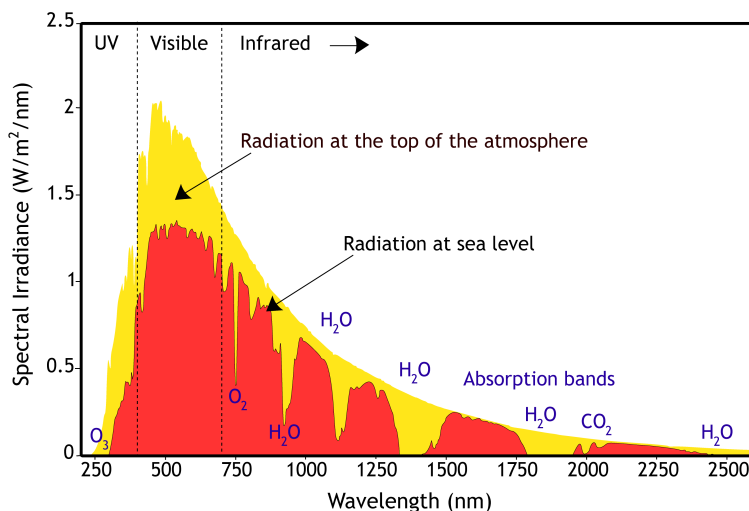


FIGURE 1.1: Spectrum showing the amount of electromagnetic radiation at the top of the earth's atmosphere and at sea level. Regions for ultraviolet (UV), visible and infrared light are indicated, as well as absorption bands caused by the earth's atmosphere.[3] The figure is adapted from Reference [4].

One semiconductor fitting the criteria of being cheap and having a wide band gap is titanium dioxide (TiO_2). TiO_2 is the most widely used white pigment[5] and is found in many everyday items such as paint, paper, toothpaste and sun cream. However, being white is a clue to the fact that titanium dioxide does not absorb visible light, but instead reflects it – this is a problem for a solar cell! TiO_2 does not absorb visible light because its band gap is large at ~ 3.1 eV, which corresponds to light in the ultraviolet part of the electromagnetic radiation spectrum. Figure 1.1 shows the amount of light reaching the earth's surface as a function of wavelength. It can be seen that while we do receive some ultraviolet light, it is only a small fraction of the amount of visible light shining upon us. In order to allow titanium dioxide to absorb visible light, a physical change has to be made: dye is added to its surface. Since dyes have colour rather than being white, this shows that they absorb at least some part of the visible spectrum. The phenomenon of sensitising semiconductors

to light using dyes was first discovered by Vogel in 1883 who used dyes to sensitise the silver halide emulsions in photographic films to longer wavelengths, enabling the image to capture more red light.[6]

In 1991 O'Regan and Grätzel developed a solar cell based on dye-sensitised TiO_2 that had a promising energy conversion efficiency due to the combination of a high TiO_2 surface area, obtained using a film of TiO_2 nanoparticles, and a dye with ideal spectral characteristics.[7] In respect to the creation and continued development of this DSC by Michael Grätzel and co-workers, it is often referred to simply as a Grätzel cell. Once a semiconductor has been dye-sensitised to visible light, it can absorb visible light which can be then converted into electrical energy. In order to use this energy, the dye/semiconductor surface must be connected in a closed electrical circuit. The cell in its entirety, including physical structure and processes, is described in detail in the following section.

1.3.1 Physical structure and processes of the Grätzel cell

Figure 1.2 is a schematic diagram showing the structure of a Grätzel cell and the physical steps by which it absorbs electromagnetic radiation from the sun and transforms this into electrical energy. Various materials can be used for the different cell components. Here the examples chosen are some that have been popular and widely used for many years. The bottom part of the figure shows the overall architecture of the cell, and the top part shows a magnification in which a dye molecule is bonded to a titanium dioxide particle. This is where the photovoltaic process begins.

1. A photon of visible light is absorbed by a dye molecule.
2. The energy of the absorbed photon is used to move an electron from the valence band of the dye molecule to one of its unoccupied levels. The dye molecule goes from being in its ground state to being in an excited state.
3. The electron now has an energy which overlaps with the TiO_2 conduction band, and can therefore transfer to it. Previously the electron could not make this

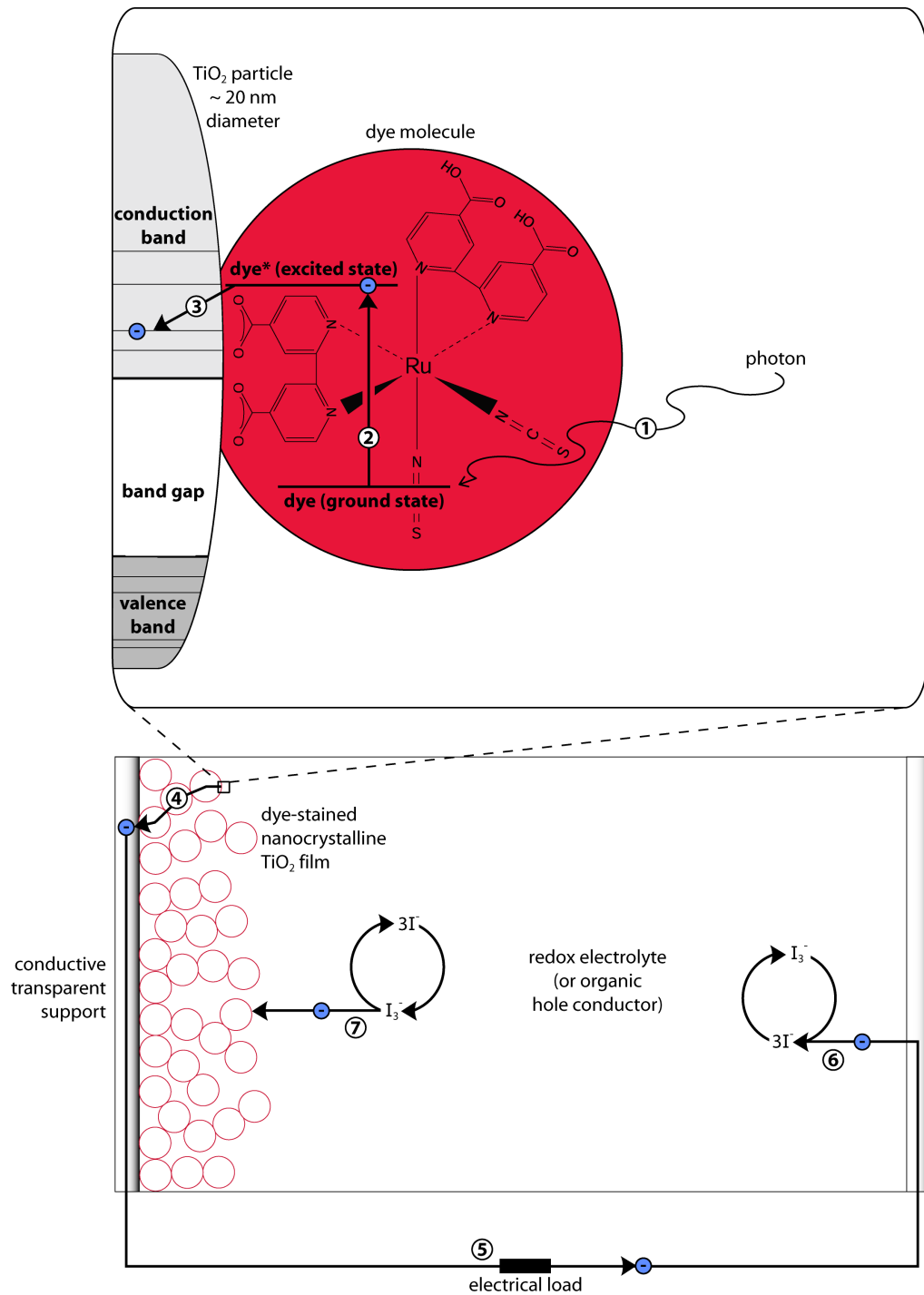


FIGURE 1.2: Schematic diagram showing the structure of a Grätzel cell and the physical steps by which it absorbs electromagnetic radiation from the sun and transforms this into electrical energy. The steps are labelled 1-7 and are explained in the main text.

transition as it was in the dye valence band, which does not overlap with the TiO_2 conduction band.

4. The electron diffuses through a network of interconnected TiO_2 particles until it reaches a conductive transparent support which is the anode of the electrical circuit.
5. The electron travels through an external load such as a battery charger, and in doing so gives it power.
6. At the cathode – also a transparent conductive layer – the electron reduces an electrolyte molecule such as iodide.
7. An iodide molecule is then oxidised into triiodide when it meets a dye molecule containing a hole, created when an electron left the molecule to travel round the circuit in step 3. The dye molecule, now with its charge regenerated, is ready to absorb another photon and begin the cycle again.

1.3.2 Materials used

In this subsection the various choices for the different Grätzel cell components are discussed starting with the dye, and then the semiconductor, anode/cathode and electrolyte.

Dye

There are certain characteristics in a dye that make it a good candidate for use in a Grätzel cell. The dye should have an absorption spectrum that covers as much of the visible region as possible, since this is the most intense part of the electromagnetic spectrum reaching the earth's surface. The dye molecules should be small so that they have a large packing fraction, increasing the chance of photon absorption. The dye should be stable to repeated oxidation and reduction cycles. The excited states of the dye must overlap energetically with the conduction band of the semiconductor so that electron injection from the dye into the semiconductor is possible. The

best dyes have a lowest unoccupied molecular orbital (LUMO) located close to the dye→semiconductor electron injection site and a strong chemical coupling to the surface. The better a dye is at electron injection, the more stable it is in light. This is because in the solar cell the excited electrons that cause the damage are quickly transferred into the substrate; the only reason that the most efficient solar cell molecule survives photoabsorption is that it is an efficient solar cell molecule. The position of the highest occupied molecular orbital (HOMO) is best situated away from the surface where it is accessible to the electrolyte, in order to allow efficient charge replenishment of the HOMO hole.

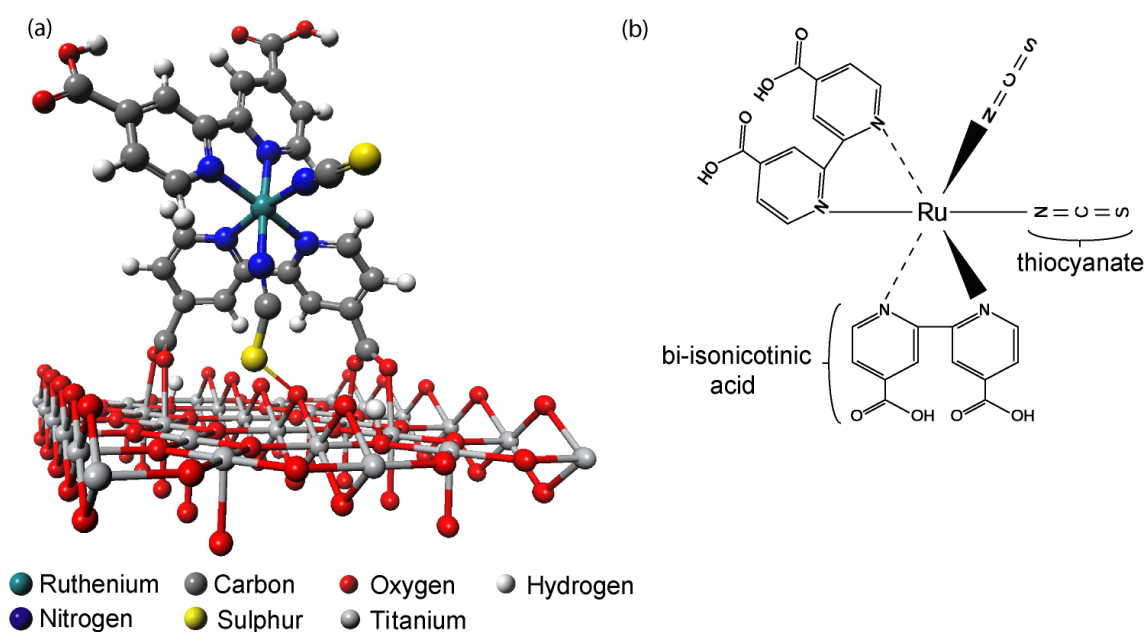


FIGURE 1.3: a) N3 molecule adsorbed on rutile TiO₂(110), calculated using CASTEP[8] at the DFT-GGA level (see Section 6.2 for details), and b) chemical structure of the N3 molecule.

The most widely used dye molecule in the Grätzel cell is known as ‘N3’ and was discovered in 1993 by Nazeeruddin and co-workers.[10] The full chemical name of the dye is RuL₂(NCS)₂ where L=4,4’-COOH-2,2’-bipyridine, and its structure can be seen in Figure 1.3 where it is shown both attached to the rutile TiO₂(110) surface and by itself. The combination of N3 as the dye and TiO₂ as the semiconductor has

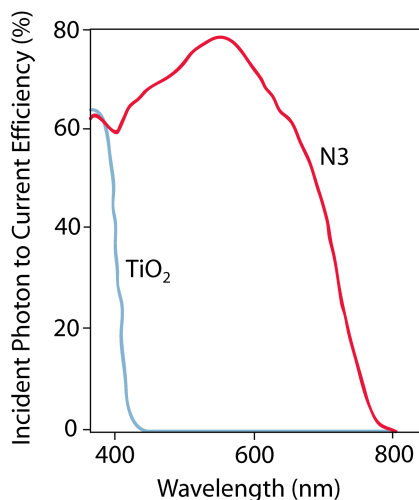


FIGURE 1.4: Incident-photon-to-current efficiency as a function of wavelength for TiO_2 and N3-sensitised TiO_2 . Figure adapted from Reference [9].

been used to give cell efficiencies of over 11%. This high efficiency warrants much interest in the dye itself, but also in why it is so well-matched with TiO_2 . What we do know is that N3 has near-ideal spectral characteristics, as shown in Figure 1.4. The dye exhibits a broad absorption curve over the 400-700 nm region, covering much of the visible spectrum. The molecule is also fairly small and has a high absorption coefficient. It also has a high chemical stability. The energy levels of N3 match incredibly well with TiO_2 such that electrons excited to any unoccupied level of the dye can transfer to the TiO_2 conduction band. The molecular LUMO is situated right next to a molecule-semiconductor bonding site, and the HOMO is amply exposed to the electrolyte. These characteristics lead to fast electron injection and high cell efficiency, and will be investigated further in the results chapters.

There are fears about ruthenium being too expensive, or that there would not be enough of it to support its widespread use in N3 DSCs. However, while ruthenium is expensive, the cells only use a small amount equivalent to less than \$0.02 per peak-watt[1] and methods are being investigated for possible retrieval of ruthenium from cells that have eventually degraded.

Following the discovery of N3 its photovoltaic performance was unmatched for eight years by hundreds of other chemicals that were synthesised and tested until in

2001 a chemical known as the ‘black dye’, or $\text{RuL}'(\text{NCS})_3$ where $\text{L}'=4,4',4''\text{-COOH-}2,2':6',2''\text{-terpyridine}$, was discovered that at the time beat N3, achieving 10.4% solar to power conversion efficiency.[9, 11] The record was broken again a few years later by using N3 in conjunction with guanidinium thiocyanate, a self-assembly facilitating additive.[9] Black dye remains an interesting contender though, as it extends the absorption range further into the UV range than N3. Other newer sensitiser being currently researched include complexes of Ru and Osmium, organic dyes and semiconductor quantum dots.[9]

Semiconductor

We have learnt that a semiconductor surface can be dye-sensitised to absorb visible light and thus be exploited in photovoltaics. However, on a flat surface a monolayer of dye molecules absorbs at most a few percent of incident light,[1] giving devices with quantum efficiencies of $\leq 0.1\%$.[12] The absorption is weak because the area that a single molecule takes up is hundreds of times larger than its optical absorption cross-section.[13] This was seen as a limiting factor in using wide band gap semiconductors to absorb visible light, until in 1976 Matsumura and Tsubomura made a breakthrough discovery.[12, 14] By using a zinc oxide (ZnO) electrode made of sintered ZnO powder in conjunction with a dye and electrolyte they achieved a 1% conversion efficiency, smashing the previous record. Sintering a powder, or nanoparticles, involves applying heat and pressure so that the particles ‘weld’ together forming a solid mass, while keeping below the material’s melting point so that the particle/gap structure is retained. Such structures are described as being mesoporous, as liquid can penetrate the network of joined particles.

The dye molecules are deposited by soaking the mesoporous semiconductor layer in a solution containing the dye. The dye molecules bond to the semiconductor surface, which through being mesoporous has a thousand-fold increased surface area compared with a flat surface.[2] The mesoporous layer has a porosity of approximately 50% and a thickness of 10 μm .[2] Photons of visible light can penetrate the mesoporous semiconductor because optical photons can penetrate materials to a thickness

approximately equal to their wavelength ($\lambda_{\text{visible}} \sim 0.5\mu\text{m}$). Any dye molecules that a photon does excite are bonded directly to the semiconductor. Those that are not bonded to the semiconductor are very unstable in light, and soon decompose. Once an electron has been injected into the semiconductor network, it ‘percolates’ through the network until it meets the conducting back contact where it is safe from recombination with dye molecules or the electrolyte.

The most commonly used semiconductor in DSCs is TiO_2 . ZnO is also a popular choice. Nanostructured TiO_2 is made up of nanoparticles for which the crystal facets are predominantly the anatase (101) surface. In the work performed in this thesis, however, the substrate of choice is single crystal (flat) rutile $\text{TiO}_2(110)$. The benefit of using a single crystal surface over a nanostructured surface is that it has a well-defined periodic structure, which is required to get molecules in the same adsorption state to study. The rutile $\text{TiO}_2(110)$ surface is chosen here over the anatase $\text{TiO}_2(101)$ surface for reasons of both practicality and cost. (This is discussed further in Section 6.1.) In the experiment using TiO_2 , the primary objective is to examine the interaction between N3 and the TiO_2 surface and then to draw conclusions relevant to the N3/nanostructured TiO_2 used in DSCs. The substrate substitution can be made because the bonding geometry of the primary binding ligand of N3 to the surfaces of both rutile $\text{TiO}_2(110)$ [15] and anatase $\text{TiO}_2(101)$ [16] is of essentially the same character, and the optical band gaps of the different phases are close at 3.05 [17] and 3.20 eV [7], respectively.

Electrodes

The cathode, which must electrically contact the electrolyte, must be transparent in order to let visible light through to the dye-sensitised surface. The anode, which electrically contacts the semiconductor, is often made translucent as well so that the cell is more aesthetically pleasing. Typical materials used are a glass or flexible plastic support coated with a transparent conducting layer of fluorine-doped tin oxide or tin-doped indium oxide.[13]

Electrolyte

The most successful combination of DSC materials to date has been the dye N3 adsorbed to the semiconductor TiO_2 along with the electrolyte redox couple iodide/triiodide. Other materials being researched that can replace the electrolyte component are ionic liquids,[18] polymer electrolytes,[19] and hole-conducting solids.[20, 21, 22] The requirement for this component of the solar cell is that it acts as a redox agent, i.e. it reduces at the cathode to carry electrons, and oxidises at the dye molecules where it gives an electron to return charge-depleted dye molecules back to their ground state. It is also important that it is both in contact with the cathode, and permeates the TiO_2 network to make full contact with the dye molecules. Although electrolytes produce cells with high efficiencies, there is a move away from using them because solvents do not make the most robust cells since they can cause leakage to occur. This is combatted by use of the more recently researched hole-conducting solids such as p-type semiconductors. Establishing an intimate contact of the hole-conducting solid with the porous network can be achieved by spin-coating the hole-conducting solid in its liquid phase.[23] The electrolyte component chosen must suit the semiconductor in terms of electronic energy levels, as the difference between the electron Fermi level in the semiconductor and the redox potential of the electrolyte corresponds to the open circuit voltage of the system.

1.4 The McFarland and Tang cell

In 2003 McFarland and Tang proposed a DSC that uses a slightly different cell architecture to the Grätzel cell.[24, 25] Their cell consists of the four layers $\text{Ti}/\text{TiO}_2/\text{Au}/\text{dye}$, the Au taking the place of an electrolyte to replenish the dye. It was proposed that photoexcited electrons in the dye travel ballistically through an ultra-thin Au layer before being injected into the TiO_2 . A photovoltage is produced by contacting the Ti and Au layers. For a device using merbromin as the dye, 10% of the absorbed photons gave rise to an electric current.

The exact nature of how the solid state device works is still under investiga-

tion. Two different theories are illustrated in Figure 1.5. The Au film is described as being $\sim 10\text{--}50$ nm thick, as illustrated in 1.5 (a). It has been shown however, that rather than being a layer of uniform thickness, Au deposited on $\text{TiO}_2(110)$ by sublimation[26, 27, 28] and sputtering[29] results in Au islands and networks with a significant proportion of the TiO_2 surface still exposed. Dye molecules could then interact simultaneously with the Au islands/networks and the TiO_2 surface. This interpretation is illustrated in 1.5 (b).

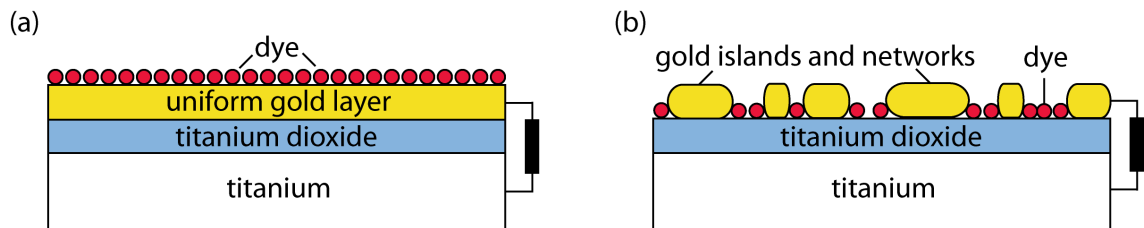


FIGURE 1.5: Schematic figure illustrating the different theories regarding the Au layer in the McFarland and Tang cell. In (a) the Au film is of uniform thickness and electrons must travel ballistically through it from the dye molecules to the TiO_2 in order to complete the circuit. In (b) the Au forms islands and networks on the TiO_2 and the dye molecules are able to bond directly to the TiO_2 surface, while also being in contact with the Au.

1.5 Future prospects for dye-sensitised solar cells

1.5.1 Existing solar cell technologies

It is clear that the performance of conventional silicon solar cells is reaching a plateau and that with silicon prices remaining high, the low cost-effectiveness of these cells limits their widespread use. In the 1970s a second generation of thin film solar cells emerged, including amorphous and thin film silicon, $\text{CuIn}(\text{Ga})\text{Se}_2$ and CdTe films, and DSCs.[1] There is now a third generation of solar cells which have multiple junctions rather than a single junction, so can achieve efficiencies higher than the 31% efficiency measured for single junction converters under standard test conditions.[30] Third generation cells currently being researched include multi-gap tandem cells, hot electron converter cells and quantum dot solar cells which multiply photoexcited

electrons.[1]

1.5.2 Benefits of dye-sensitised solar cells

Dye-sensitised solar cells can be fabricated cheaply compared to conventional silicon solar cells which have a high cost in terms of both energy and money, due to the high temperatures and high-vacuum processes required to obtain solar grade silicon. To illustrate this, construction of a DSC has been used by the project supervisor as an undergraduate laboratory project. The cells are stable under long-term illumination and exposure to high temperatures. The use of a solvent-free electrolyte component improves this stability further. Silicon cells and DSCs that are rated equally under standard test conditions perform differently under realistic outdoor conditions, in which DSCs have been shown to produce 20-30% more energy than their equally rated polycrystalline counterparts.[1] This is because DSC performance is practically unaltered by temperature whereas silicon cells produce approximately 20% less electrical energy in hot, sunny conditions. Also, the DSC is less dependent upon the sunlight's angle of incidence, and performs better than silicon under cloudy conditions with diffuse light.

The current top DSC efficiencies are 11% for the Grätzel cell, 4.2% for solid-state equivalents using organic hole-conductors, 4.8% for organic photovoltaic cells based on blends of fullerene derivatives, and 5-6% for nanocomposite films comprising only inorganic materials. To improve DSC performance, new dyes or combinations are being developed, with the aim being to increase optical absorption cross-sections and broaden the radiation absorption band into the near-infrared.

1.5.3 Commercial interest and predicted future use

A notable benefit of DSCs is that they can be made to be transparent, so are generally considered to be more aesthetically pleasing than conventional silicon cells. An example of a DSC suitable for commercial use is shown in Figure 1.6. The cells are tinted the colour of the dye used, and here are examples showing orange, burgundy, turquoise and green colours. The cells can be produced in a variety of styles that can

be incorporated into roofs or windows.

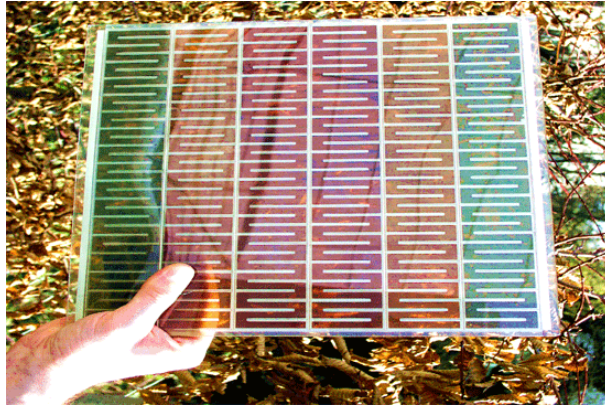


FIGURE 1.6: A dye-sensitised solar cell.[31]

Commercial interest in DSCs is steadily rising, including the Welsh company G24innovations who produce DSCs by the roll and have developed products such as portable solar chargers and lighting systems. The Australian company Dyesol also has operations in the UK, Italy and Switzerland, and produces DSC components that can be incorporated directly into buildings. The Toyota Dream House,[32] built with the objective of being an energy-saving intelligent house supporting the latest network computing technologies, had DSC panels installed in its walls. Konarka, USA, produce flexible cells which they call ‘power plastic’ for the commercial market. The expansion of commercial interest in photovoltaics, combined with environmental concerns and increasingly proactive environmental policies, suggest that photovoltaics will have a significant role to play in our future energy supply. It is calculated that by 2065 the whole world’s energy demands *could* be supplied by photovoltaic cells.[33, 1]

1.6 Topics researched in this thesis

In the effort to discover more efficient DSCs, there are two routes that one can take: the empirical trial and error of different dyes, semiconductors, electrolytes and additives, or research into understanding why certain materials produce superior cells,

and using this knowledge to engineer new dyes. While brute force empirical methods have been a major factor in the discovery of new efficient dyes and material combinations, they rely somewhat on chance, and can be better guided by a sound understanding of scientific fundamentals found through more targeted research. In this work the second approach is used.

Chapters 1-5 lead up to results chapter 6 in which the popular and efficient combination of the dye molecule N3 with the semiconductor TiO_2 is investigated in great detail. The techniques used are mainly experimental, and uncover the geometric and electronic structure of N3 bonded to TiO_2 , as well as the dynamics of the electron injection from N3 into TiO_2 . The sample preparation was carried out under ultra-high vacuum (UHV) using a recently-developed UHV electrospray deposition system, described in Chapter 5. This is the first study of N3 on TiO_2 where the sample was both prepared and analysed under UHV; previous studies have used samples prepared at ambient to medium vacuum. Preparing samples under UHV largely eliminates the presence of atmospheric contaminants that can obscure the results one sees when measuring the sample properties. In Chapter 7 the combination of N3 and Au – relevant to the McFarland and Tang solar cell – is investigated in detail using the same deposition method and similar techniques as above.

CHAPTER 2

Synchrotron radiation

2.1 Introduction

The majority of the experimental work presented in this thesis was done using techniques that require intense, tunable electromagnetic radiation. The techniques are described in detail in chapters 3 and 4. But first, let us understand how this type of light is produced and controlled.

Charged particles travelling at relativistic speeds emit radiation when they change momentum. Radiation created in this way is called *synchrotron radiation*. For charged particles to move at speeds large enough to emit photons of significant energy, they must have long mean free paths, and this can only happen in vacuum. The two environments in which synchrotron radiation can occur, therefore, are deep space (see Figure 2.1) and man-made ultra-high vacuum chambers here on earth.

The first man-made synchrotron radiation was produced as a by-product of particle accelerator rings, where the main purpose was to study the particles themselves, not the light emitted from them. The synchrotron radiation produced was utilised via so-called *parasitic* ports. With the recognition of the importance of bulk and surface science techniques that use synchrotron radiation as an excitation source, there are now tens of dedicated synchrotron radiation sources throughout the world.

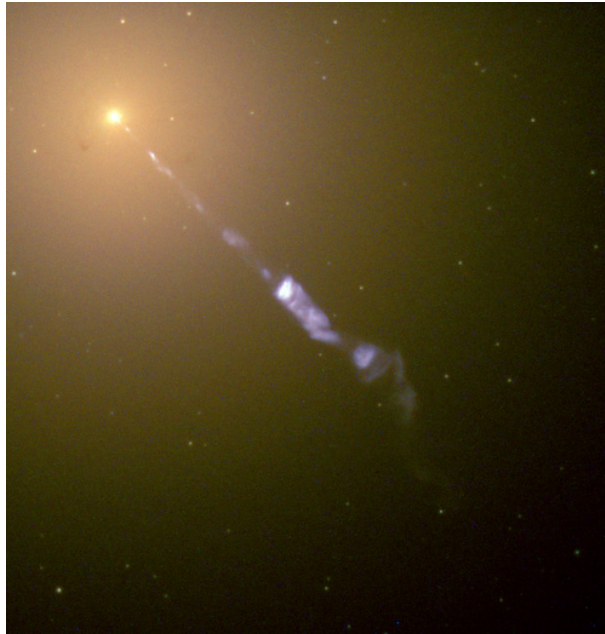


FIGURE 2.1: Hubble space telescope image of the M87 galaxy. Magnetic field lines, created by a supermassive black hole at the galaxy's centre, trap electrons which are sent out in relativistic jets. Spiralling at relativistic speeds, the electrons emit synchrotron radiation.[34]

2.2 Synchrotron layout

The various stages in the production of synchrotron radiation are now described,[35] starting with electrons leaving a hot filament, and ending with intense, polarised light, tunable over a large range of photon energies from visible light to hard x-rays. The stages 1-6 are labelled in the schematic Figure 2.2.

Electrons are generated using an electron gun (1) and are then accelerated to almost the speed of light by a linear accelerator (2) and a booster ring (3). The electrons are then transferred to the storage ring (4). The term ‘ring’ is a misnomer, as it is actually a polygon; electrons travel through vacuum in straight lines unless an electric or magnetic force is applied orthogonal to their motion. The electrons are made to turn using bending magnets, or insertion devices which are described in Section 2.3. As the electrons are deflected by the magnets, they change momentum and so give off synchrotron light at a tangent to the ring. The light then travels down a *beamline* (5) where it is made ready for use in experiments, and eventually arrives at an *end station* (6). This is where the experimentalists work and where the light finally reaches their samples.

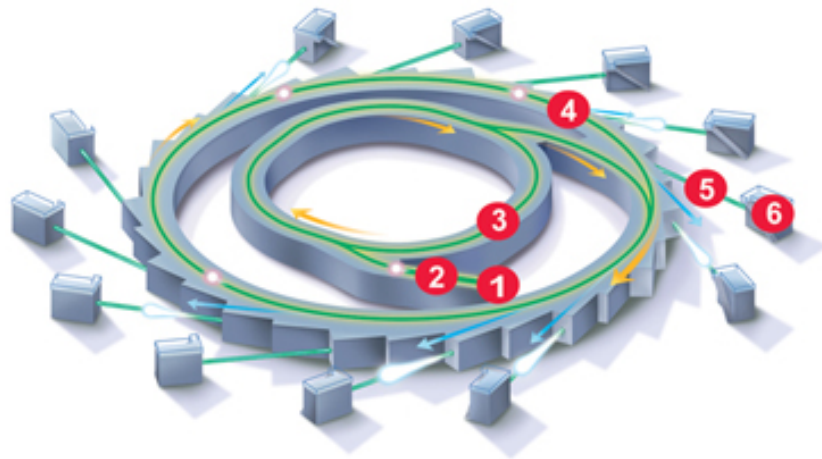


FIGURE 2.2: Schematic image of a synchrotron,[36] showing the (1) electron gun, (2) linear accelerator, (3) booster ring, (4) storage ring, (5) beamline and (6) end station.

2.3 Wigglers and undulators

The most simple way in which to deflect the electrons in the storage ring is to use a bending magnet, i.e. the electrons pass through a simple electromagnet with a ‘north’ on one side and ‘south’ on the other. As the electrons change momentum while turning, they emit radiation with a very broad energy spectrum. The emitted radiation is often described as being like a searchlight, pointing forwards along the tangent of the ring, and sweeping round as the electrons turn.

The more advanced insertion devices used in the storage ring to deflect the electron beam are called *wigglers* and *undulators*. Instead of the electrons illuminating the beamline once for every time they go around the storage ring, these devices cause the electrons to illuminate the beamline several times, or for one long pulse of light. This is done by forcing the electrons to oscillate using a series of magnets with alternating poles.

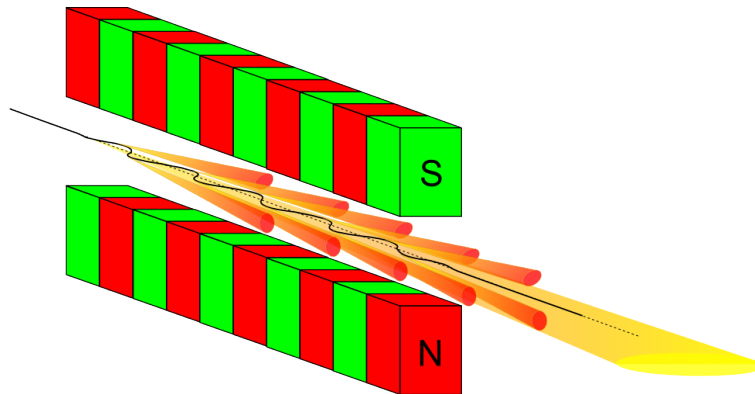


FIGURE 2.3: An undulator insertion device. An array of magnets guide electrons in a gently undulating path, causing them to emit forward-pointing radiation.[37]

In a wiggler, the oscillating motion of the electrons causes the radiation ‘searchlight’ to move from side-to-side so that it shines down the beamline many times, in quick succession. The beamline receives short pulses of light, the number of which being equal to the number of magnet pairs in the array. In an undulator, as illustrated in Figure 2.3, the magnets used are much weaker, such that the electrons do not move side-to-side so much and the radiation cone illuminates the beamline

constantly, resulting in one long pulse of light.

The distinction between how an electron moves in a wiggler and an undulator can be made using the dimensionless magnetic deflection parameter K :

$$K = \frac{eB\lambda_u}{2\pi m_e c}, \quad (2.1)$$

where e is the charge on an electron, B is the magnetic field, λ_u is the wavelength of the undulating electron motion (equal to twice the magnet spacing), m_e is the mass of an electron at rest and c is the speed of light. The maximum *excursion angle of the electrons* is $\frac{K}{\gamma}$ and the maximum *radiation emission angle* is $\frac{1}{\gamma}$, where γ is the Lorentz contraction factor. With a strong magnetic field, $K \gg 1$, and the excursion angle of the beam is much bigger than the radiation emission angle. This is the case for a wiggler, where the radiation is widely separated in angle and does not overlap spatially after some propagation distance. For a weaker magnetic field such that $K \leq 1$, the excursion angle of the beam lies within the radiation cone. This is the case for an undulator where the radiation continues to overlap spatially for a significant propagation distance, causing interesting interference effects.

With the small electron excursion angle produced by undulators, the photon energy range is small, resulting in a high photon flux within this energy range. Another feature of undulators is that the overlapping of the light cones means that constructive interference can occur; certain wavelengths are significantly enhanced. The energies that are enhanced can be tuned by the user by changing the geometry of the undulators. This is done by altering the gap between the top and bottom arrays of magnets. Occasionally a broad energy range of approximately constant intensity is required. This is achieved by tilting the magnet arrays with respect to each other, so that mixing occurs, and the peaks in flux at specific energies are smeared out.

The high intensity of photons produced by undulators is both a blessing and a curse. The high photon intensity means that a relatively high signal is measured in whatever technique one is using. But for fragile, organic samples there is a risk of *beam damage*. This is where the sample is changed by the beam, e.g. the beam might break chemical bonds. In this case, one must assess how long a sample can safely be

kept in the beam path, and either measure in a different place on the sample each time, or else continually move the sample throughout data acquisition.

2.4 Beamline I511

The purpose of a beamline is to make the radiation leaving the ring ready to be used in experiments at the end stations. In all the synchrotron experiments presented in this thesis, the undulator beamline I511 at the MAX II synchrotron of the National Swedish Laboratory MAX-lab was used. A schematic figure of beamline I511 is shown in Figure 2.4 and a photograph of the beamline is shown in Figure 2.5.

Curved mirrors are used at various stages to focus the light leaving the storage ring, in order to minimise loss of photons and to obtain an intense beam on the sample. The energy of the photons required by the user is selected at the monochromator using either a crystal or a grating. A grating is used on the I511 beamline and gives access to a photon energy range of 90-1500 eV.[38] A special feature of beamline I511 is that it splits at the end so that two different end stations can be used; these are the surface end station I511-1 and the bulk end station I511-3. The synchrotron light can either be pointed at one end station or the other using a flip mirror.

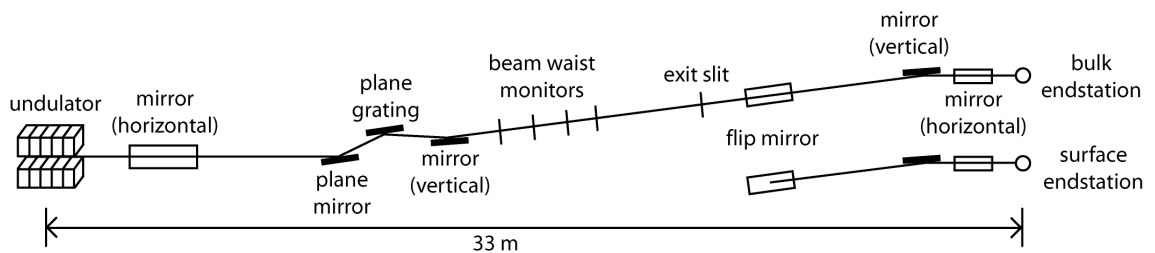


FIGURE 2.4: Schematic figure of the I511 beamline at the MAX-II synchrotron in MAX-lab, Sweden. The figure is adapted from reference [38].

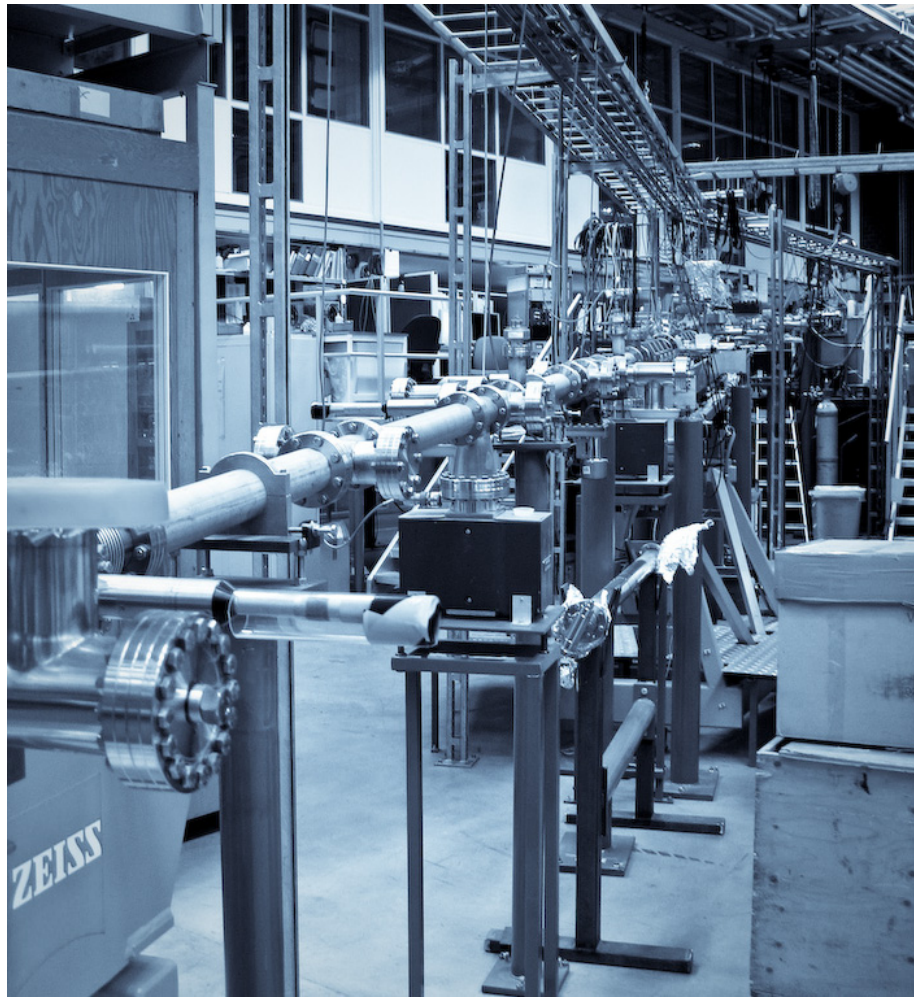


FIGURE 2.5: Photograph of the I511 beamline at the MAX-II synchrotron in MAX-lab, Sweden.

2.5 End station I511-1

At the end of each beamline is an end station consisting of various ultra-high vacuum chambers attached to each other. There is usually a chamber in which to prepare samples and a separate analysis chamber where the samples are exposed to synchrotron light, and emitted electrons or photons are collected and analysed. The end station used in this work was I511-1, shown in Figure 2.6. This end station was specifically designed for surface science experiments, as it was set up so that the photon beam is at *grazing incidence* to the sample surface. This is explained in the next section.

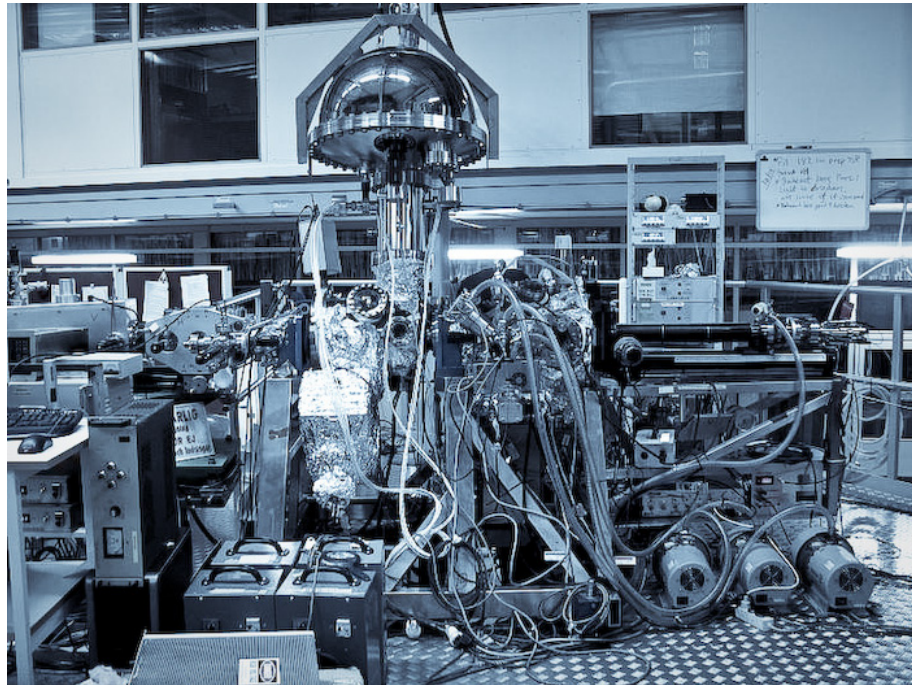


FIGURE 2.6: Photograph of the I511-1 surface science end station. The rotatable electron analyser can be seen in the top of the photograph.

The end station is equipped with a sputter gun. The gun uses an electric field to accelerate inert argon ions towards the sample, where they knock matter away from the top of the surface enabling samples to be atomically cleaned. A manipulator is used to move the sample in x, y and z, and also to rotate it about the beam axis. The manipulator also houses electric connections which can be used to heat the sample

using an electric current. This gives the sample thermal energy, allowing surface and bulk atoms in the sample to move around and repair surface defects caused by the argon sputtering.

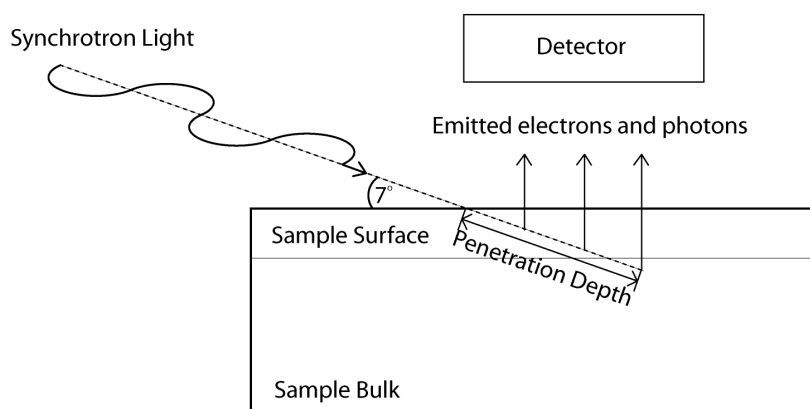
Also attached to the chamber is equipment used to measure what is emitted from the sample when the synchrotron light is shone onto it. The photoelectron analyser measures the kinetic energy of *electrons* leaving the sample, and the x-ray emission spectrometer measures the energy of *photons* leaving the sample. These analysers are described in more detail in chapter 3. A special feature of this end station is the ability to rotate the analysers around the beam axis, enabling the user to choose the detection direction with respect to the light polarisation vector, \mathbf{E} , of the light. Unless altered, this is horizontal due to the orientation of the storage ring. Some experiments may require the polarisation to be switched between horizontal and vertical for magnetic spectroscopy, or to be circularly or elliptically polarised to produce a very intense light beam. This is done by moving the undulator magnet arrays with respect to each other in the beam propagation direction.

It is important to have an ultra-high vacuum within the chambers during the experiment, typically around 1×10^{-10} mbar. This is because it is important to have a clean sample, free from atmospheric contaminants. If the vacuum is not high enough, the sample can be covered in a layer of contaminants from the air within a second; at ultra-high vacuum, the sample can stay clean for many hours. To achieve a high vacuum, the vacuum chambers must be baked to approximately 150 °C. This high temperature evaporates both water and volatile molecules that are still present on the inner surface of the vacuum chambers even after pumping out the air. The baking is done using heating tapes which are wrapped around the chambers and covered with layers of aluminium foil. The foil keeps the heat in and also ensures slow heating and cooling, so as not to damage windows and other fragile components by uneven thermal expansion and contraction. After several hours, the pressure within the chambers drops to below 1×10^{-7} mbar and the heating tapes are turned off. Once the system cools down, the pressure drops further to below 1×10^{-10} mbar. The experiments can then commence.

2.6 The importance of grazing incidence

Having the sample at *grazing incidence* to the synchrotron beam, as opposed to *normal incidence*, means that a larger proportion of electrons and photons emerge from the surface of the sample than from the bulk. This is illustrated in Figure 2.7. Synchrotron light penetrates samples to a sample depth of approximately 100 nm. The emitted photons and electrons have escape depths of approximately 100 nm and 10 nm respectively. At normal incidence the plane of the sample surface is positioned perpendicular to the incident synchrotron light. The light therefore penetrates to a depth of 100 nm, allowing photons and electrons to emerge from depths of 100 nm and 10 nm respectively. At grazing incidence the plane of the sample surface is positioned at a small angle with respect to the incident synchrotron light. On the I511-1 end station, this angle is fixed at 7° due to the geometry of the beamline. The light then penetrates to a shallower depth of $\sin(7^\circ) \times 100 \text{ nm} = 12 \text{ nm}$, and the incident photons spend more time travelling through the uppermost sample layers where they are potentially absorbed by electrons. A further benefit of grazing incidence is that the synchrotron beam is spread out on the surface creating a larger illuminated spot, thus reducing beam damage and exciting photoelectrons from more of the sample.

(a) Grazing Incidence



(b) Normal Incidence

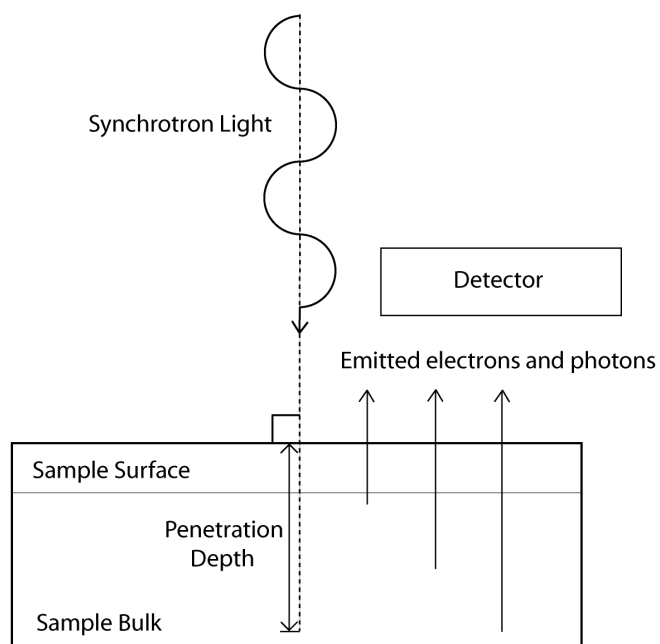


FIGURE 2.7: Schematic figure illustrating that when the synchrotron beam is at (a) grazing incidence to the sample surface, as opposed to (b) normal incidence, the emitted photons and electrons originate from higher up in the sample.

CHAPTER 3

Adsorption of molecules to surfaces

3.1 Introduction

This chapter describes the experimental and theoretical techniques used in this work to study the *adsorption* of molecules on surfaces. Adsorption is the process by which an atom or molecule – the adsorbate – forms a bond to a surface. A molecule adsorbed to a surface is illustrated in Figure 3.1. The techniques described here reveal information about the uppermost layers of a surface, and atoms or molecules that are adsorbed on it.

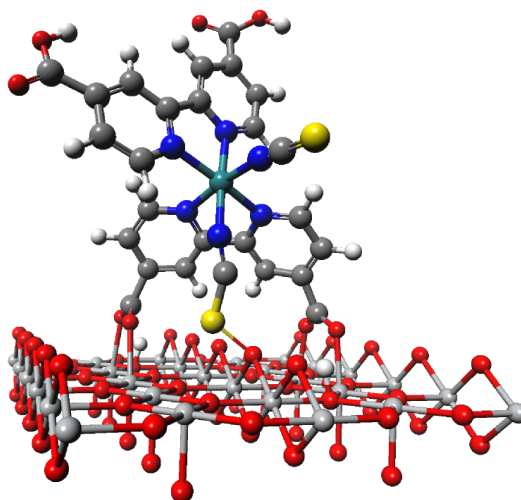


FIGURE 3.1: Image of an N₃ molecule adsorbed to the rutile TiO₂(110) surface, produced from density functional theory calculations which are described in Section 3.5; specific parameters for this particular calculation are given in Section 6.2.

Adsorption can be investigated in terms of both physical and electronic structure. Electron and photon spectroscopic techniques can unveil the electronic energy levels in a sample, both those that are occupied by electrons and those that are not. They can also be used to determine the bonds that exist between the adsorbate and the surface, and the orientation of the adsorbate with respect to the surface. To support these experimental techniques, the surface interface and adsorbate can be modelled using theoretical techniques. These calculations are useful to help to understand what is seen with experiment, or as a double-check to confirm interpretations from experiment. Finally, scanning tunnelling microscopy, a direct imaging technique, is used here to study the way in which molecules are distributed across a surface.

A surface is defined as the interface between a solid and either a vacuum, gas or liquid. When studying atoms and molecules on surfaces, a simple surface is desirable so as not to add extra complexity to the system. Typically, a flat crystal surface is used. Crystals have long-range order, and can be cut at an angle that exposes a particular crystal plane. The experiment can then begin with a known, well-defined, periodic structure. The crystal plane can be described using Miller indices; these are three integers that denote the reciprocals of the three Cartesian axis intercepts through which a crystal is cut. The $\text{TiO}_2(110)$ and $\text{Au}(111)$ crystal planes, used in this work, are shown in Figure 3.2.

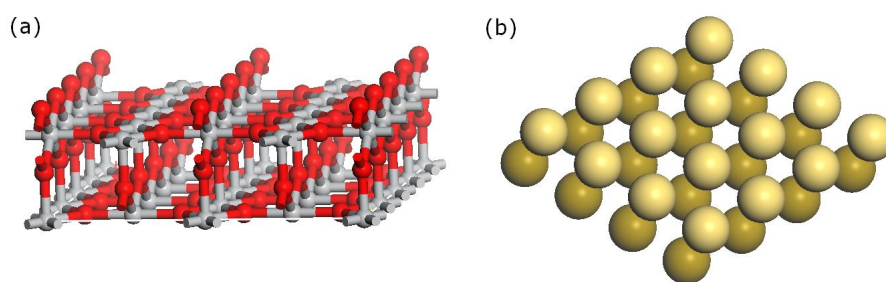


FIGURE 3.2: Structure of the (a) $\text{TiO}_2(110)$ and (b) $\text{Au}(111)$ crystal planes. In (a), red spheres represent O atoms and grey spheres Ti atoms. In (b), all spheres represent Au atoms.

In some cases the surface itself is studied, but in this work we study molecules

adsorbed on surfaces – a key component of dye-sensitised solar cells. This part of the cell is where light is absorbed by molecules, exciting electrons within the molecules before they then move into the surface, forming part of an electrical circuit. In other words, this is where solar energy is converted into electrical energy. The cell as a whole is of course also important, and there are ongoing studies into the best molecules, semiconductor and electrolyte to use, as well as studies into the introduction of new components such as extra layers in between the oxide and the molecules.

3.2 Photoemission spectroscopy

3.2.1 Bound electrons

As discussed in the previous section, the systems being studied here consist of a crystal with molecules adsorbed on its surface. In the crystal and the adsorbate, there exist many electrons which all have discrete energies. For example, in a TiO_2 crystal, each Ti atom has 22 electrons and each O atom has 8 electrons. Each electron has a particular *ionisation potential* that it would have to overcome in order to leave the atom or molecule to which it is bound. The ionisation potential energy can be split into the *binding energy*, which is the energy of the bound electron with respect to the Fermi level, and the *work function*, defined as the energy required to move an electron from the Fermi level to the vacuum level. These levels and energies are illustrated schematically in Figure 3.3. The Fermi level is the energy at which the probability of an electron being there is $\frac{1}{2}$. For metals it lies just above the highest occupied electronic level. For insulators and intrinsic semiconductors it lies at the centre of the band gap, and in doped semiconductors it moves closer to either the conduction band or the valence band depending on whether the doping is negative or positive. The vacuum level is the energy at which an electron is far enough away from neighbouring particles that it no longer feels an interaction with them, and the electron is at rest because it has no kinetic energy. Any further energy that the electron gained would be kinetic energy, allowing it to move through the vacuum, and placing it above the vacuum level on the schematic figure. Between the Fermi level and the vacuum level

there exist unoccupied, bound electronic levels.

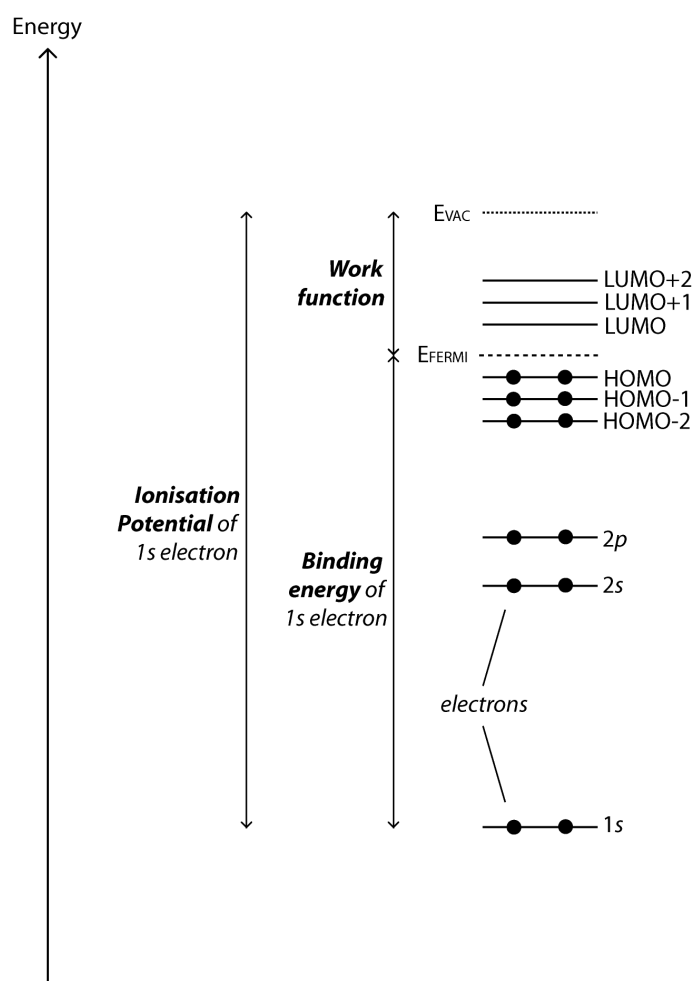


FIGURE 3.3: Definition of terms for bound electrons. Here the energy levels for a molecule are shown. LUMO and HOMO are the lowest unoccupied and highest occupied molecular orbitals, respectively.

Electrons exist either in atomic energy levels, or molecular energy levels where some atomic levels have mixed through bonding. The atomic energy levels are well-defined for an element. They are represented by the quantum numbers n and l , which are the principal quantum number (or shell number) and the azimuthal quantum number (or orbital angular momentum), respectively. For example, the $1s$ electrons have the highest binding energy, followed by the $2s$, then the $2p$ electrons etc. The atomic levels can be described either as *core levels*, where they have a high binding

energy and can be visualised as existing close to the nucleus, or they can be *valence levels* which are those with a low binding energy close to the Fermi level, and which are used for bonding between atoms.

Molecular energy levels, or molecular orbitals, contain weakly bound electrons in energy levels that are mixed, and are localised to not just a single atom, but spread over neighbouring atoms. In some cases, molecular orbitals can be spread over the entire molecule. The occupied molecular orbitals can often not be resolved, and are collectively called the *valence band*.

While the core levels are labelled specifically according to their quantum numbers, a different notation is used for mixed molecular orbitals. The highest occupied molecular orbital is called the HOMO, and the next highest is denoted the HOMO-1, then the HOMO-2 etc. As well as occupied molecular orbitals, there are also unoccupied molecular orbitals that although unoccupied, have a fixed ionisation potential and can only be filled with an electron with that energy. The lowest unoccupied molecular orbital is called the LUMO, and the next lowest denoted the LUMO+1, then the LUMO+2 etc. This notation system allows one to refer to mixed molecular orbitals for which one does not need to know anything about the quantum numbers involved.

3.2.2 Uses of photoemission spectroscopy

Photoemission spectroscopy is a powerful technique that allows one to measure the binding energy of electrons. The electronic signature of every element is unique, and the simplest use of photoemission spectroscopy is to identify the elements present in a sample. It could be used, for example, to find out which elements are present in an historical artifact such as a painting, giving clues to the paint used, and thus also to the era and geographical location in which it was produced.

Photoemission spectroscopy can also be used to discover the chemical states of bonded atoms. Atoms bond by their electrons rearranging themselves into more energetically favourable positions in the presence of other atoms. This causes the electrons to shift slightly in binding energy, and since one can measure the binding energy of electrons, this shift can be detected. For example, atoms with partially pos-

itive charges cause the binding energy of the electrons in core levels to shift to higher values, associated with an increase in Coulombic attraction between the electrons and the nucleus.

In this work, photoemission spectroscopy is used for elemental identification at the start of an experiment, to check that the surface is comprised of the expected elements and is free from contaminants. Its main use, however, is to identify the chemical states of the atoms in the molecules that are adsorbed to a crystal surface. This enables conclusions to be drawn about how the molecules bond to the crystal surface - through which of the molecule's atoms, and to which atoms of the crystal surface? This is an important step in understanding how charge moves between the molecules and the surface, which is fundamental in understanding the exact way in which dye-sensitised solar cells function. Techniques to study charge transfer are discussed in the next chapter.

3.2.3 The photoemission process

The basic principle underlying photoemission spectroscopy is the photoelectric effect,[39] in which electrons are emitted from matter following absorption of photons. The emitted electrons are termed photoelectrons. The energies of the photon absorbed, and the photoelectron, are related by the equation,

$$h\nu = E_B + \phi + E_K, \quad (3.1)$$

where $h\nu$ is the energy of the absorbed photon, E_B is the binding energy of the electron, ϕ is the work function of the surface, and E_K is the kinetic energy of the emitted photoelectron. The terms binding energy and work function were defined previously in Section 3.2.1, and shown schematically in Figure 3.3.

When a photon is absorbed by an electron, it transfers all of its energy to the electron. The electron can then expend this energy, if it is high enough, in overcoming its binding energy so that it is no longer bound to the atom or molecule it was in, overcoming the work function of the surface so that it is no longer bound to the surface, then any remaining energy the electron has becomes kinetic energy. The

electron is then free to travel through the vacuum. If the electron is incident upon an electron detector, it then gains energy equal to the work function of the detector, and its final kinetic energy can be measured. Through knowing the energy of the absorbed photon, the work function of the detector, and the measured kinetic energy, the binding energy of the electron can be determined from Equation 3.1.

An energy level diagram showing the photoemission process and other consequent processes is shown in Figure 3.4. Initially, the molecule is in its ground state; all of the electronic energy levels below the Fermi level are filled. Then, a photon is incident upon the system and a photoelectron is emitted. Photons are not always absorbed; the probability of absorption depends on the magnitude and polarisation of the photon's electric field vector, the initial and final electronic states of the atom or molecule, and the energy density of final states for the transition.

3.2.4 Relaxation processes

Once the photoelectron has left the atom or molecule, a valence or core hole remains. Having a core hole means that the system is in an unstable excited state with a finite lifetime. It is more energetically favourable to have a hole in a low binding energy state than in a high binding energy state, so the system stabilises by an electron dropping down from the valence band to fill the core hole. So that energy is conserved, the system must simultaneously *lose* energy at this step, and does so either by emission of an electron, termed Auger decay, or emission of a photon, termed fluorescent decay. For elements with a low atomic mass, Auger decay is the dominant process, which makes it easier to detect than x-ray fluorescence. A graph showing the probabilities of Auger and fluorescent decay as a function of atomic number is shown in Figure 3.5.

3.2.5 Loss processes

Not every electron that is emitted through photoemission or Auger decay makes it from its original energy level to the vacuum level unaffected. Along the way there are several potential interactions it can take part in which cause it to lose energy. Two

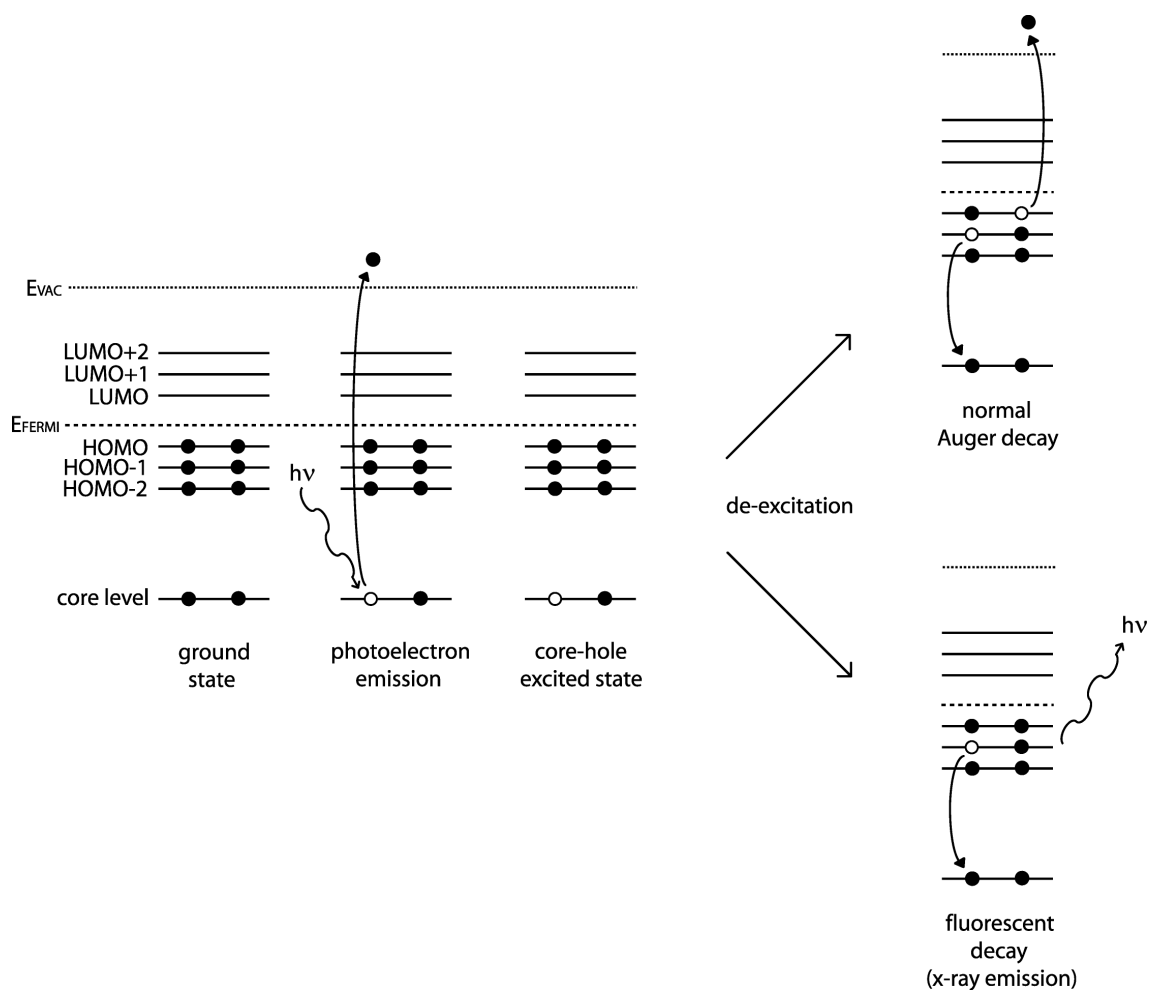


FIGURE 3.4: Electronic energy level diagrams depicting the photoemission process for a molecule. In its ground state, the molecule absorbs a photon with energy $h\nu$. This energy is transferred to an electron which becomes a photoelectron and is emitted from the molecule. This leaves the molecule in an excited state as it has a core hole, which is an energetically unstable state to be in. The molecule then relaxes as an electron drops from the valence band to fill the core hole, and either an electron or photon is emitted. These decay processes are termed Auger and fluorescent decay (x-ray emission), respectively.

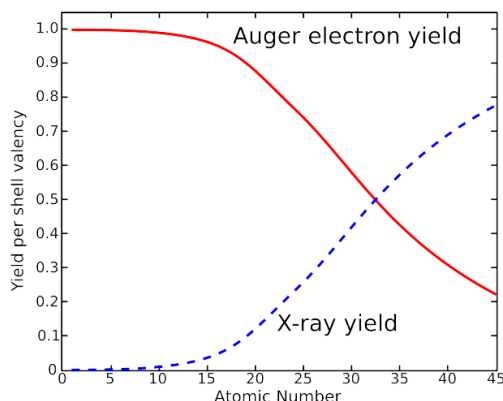


FIGURE 3.5: Comparison of Auger yield and fluorescence yield as a function of atomic number. Figure adapted from Reference [40].

of these interactions give rise to resolvable features in photoelectron spectra and are known as *satellite peaks*. The rest of the interactions do not give rise to resolvable features and the electrons are said to have been *inelastically scattered*.

The two resolvable loss processes are called *shake ups* and *shake offs*. These are depicted in Figure 3.6. As the primary photoelectron leaves the atom or molecule it excites another high-lying electron by giving it some energy. It may excite a high-lying electron into an unoccupied level – shake up – or it may excite a high lying electron to the vacuum level or above – shake off. The primary electron can be thought of as shaking an electron higher up the energy level diagram, or shaking an electron off the atom or molecule entirely. The primary electron then leaves the atom or molecule as usual and may be detected by an electron analyser, but through losing some energy it now has a lower kinetic energy. The kinetic energy deficit is equal to the amount it gave to the high-lying electron. When the spectra are switched from a kinetic energy scale to a binding energy scale any shake up or shake off peaks will appear to have higher binding energy than the main photoelectron peak. Shake off peaks appear to lie to higher binding energy than shake up peaks. These processes are called *final state effects* because the final state of the atom or molecule is different to how it would have been had the primary electron left unperturbed.

In the unresolvable loss processes, the primary electron is involved in interactions

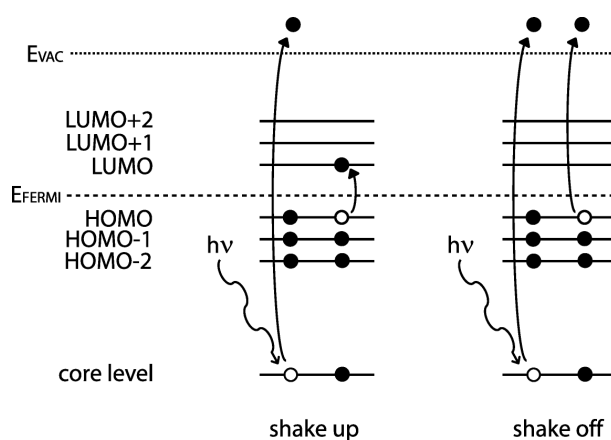


FIGURE 3.6: Electronic energy level diagrams depicting the shake up and shake off loss processes in photoemission spectroscopy. Here a molecule in its ground state absorbs a photon with energy $h\nu$. This energy is transferred to an electron which becomes a photoelectron and is emitted from the molecule. On its way out however, the photoelectron gives some energy to an electron which is either promoted to an unoccupied level (shake up) or ejected from the molecule altogether (shake off). Because the primary photoelectron loses some kinetic energy in the process, it is measured accordingly and when on a binding energy axis appears to higher binding energy than those photoelectrons that did not lose any energy.

once it has left its atom or molecule and is travelling through the bulk. Interactions it may have include the excitation of phonons and surface or bulk plasmons. A phonon is the quantisation of a sound wave in matter and a plasmon is the quantisation of some electron density oscillating around stationary positive ions. Since these excitations can take a wide range of incrementally different energies from the electron, these features cannot be resolved and usually result in a smooth background. Additionally, once an electron has slowed down through losing significant energy, it is more likely to be involved in further interactions. These electrons have then lost the information about the energy level or Auger transition from which they came, and contribute to a background of ‘uninformative’ secondary electrons.

3.2.6 *l-s* spin-orbit coupling

Electrons sharing an electronic orbital interact among themselves to conserve their total angular momentum, j . The total angular momentum is a combination of the orbital angular momentum, l , and the electron spin, s , in the relationship $j = l + s$. The properties l and s must interact, or *couple*, so that total angular momentum is conserved. When an electron is emitted from a core level it leaves behind another one which can either have spin up ($s = 1/2$) or spin down ($s = -1/2$) and therefore is involved in a magnetic interaction with l . For energy levels with $l > 0$ this interaction causes the energies of the two possible final states to split. Since electrons are then emitted with two different energies, the splitting is apparent in corresponding photoelectron spectra of that level which show two distinct peaks at different binding energies. Spin-orbit splitting doesn’t occur for the s levels for which $l = 0$, but it does for the p , d and f levels etc. for which $l = 1, 2$ and 3 etc., respectively.

For example, for any p level such as Ti $2p$, $l = 1$ and $s = \pm 1/2$. The total angular momentum, $j = l + s = (1) \pm 1/2$. Therefore $j = 1/2$ or $3/2$. The degeneracy, or number of electrons in each of these j states, is given by $2j + 1$, so is $2(1/2)+1 = 2$ for $j = 1/2$ and $2(3/2)+1 = 4$ for $j = 3/2$. In a fully occupied p level there would therefore be two electrons with $-1/2$ spin and four electrons with $+1/2$ spin. These two different energy levels would cause two photoelectron peaks with an intensity

ratio of 1:2. The state with the lower total angular momentum makes the smaller photoelectron peak of the two and has the higher binding energy.

3.2.7 Elemental identification

Figure 3.7 shows a *wide scan* electron spectrum of N3 on $\text{TiO}_2(110)$. This is a broad, low-resolution spectrum showing the number of electrons detected as a function of binding energy when a sample is illuminated with monoenergetic light.

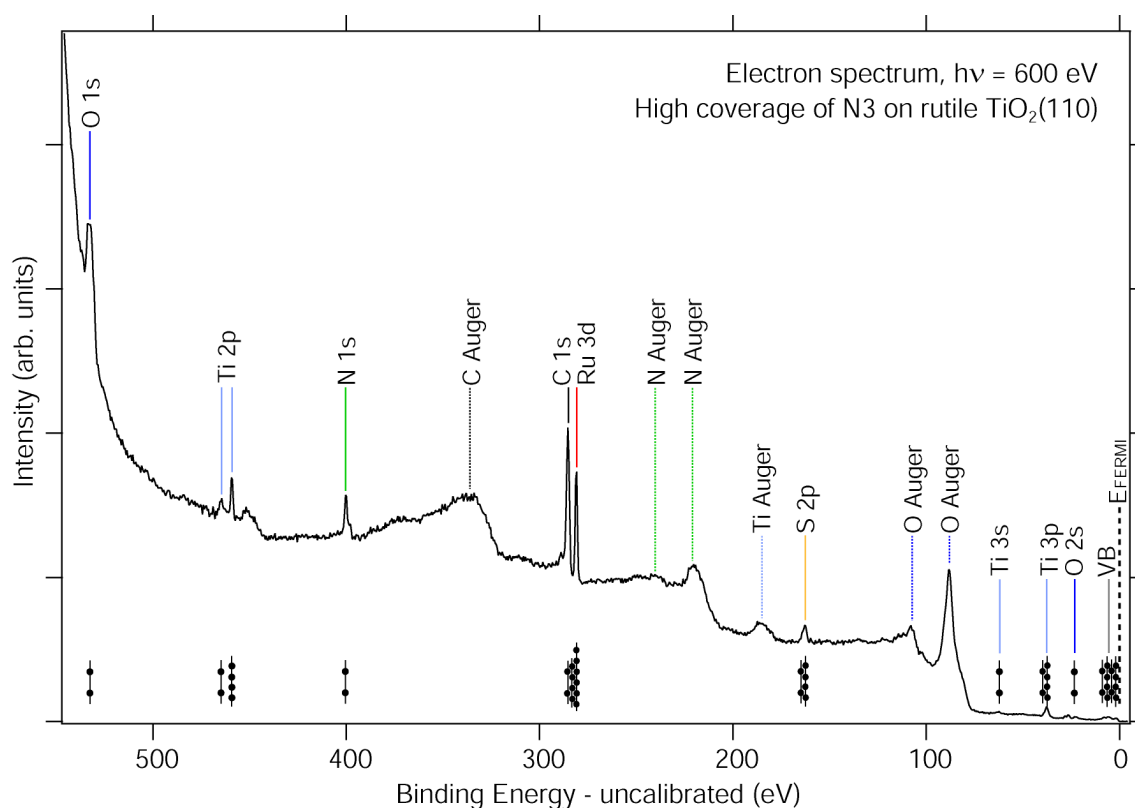


FIGURE 3.7: Wide scan electron spectrum, taken using photoemission spectroscopy. Here the sample is a high coverage of N3 on the $\text{TiO}_2(110)$ surface. The schematic electronic energy levels have been appended so that it is clear how this experimental plot relates to the energy level diagrams shown in Figure 3.4.

The background of the spectrum increases to higher binding energy, and is caused by *secondary electrons* that have been emitted, and then undergone inelastic scattering before leaving the surface. Secondary electrons that appear to have a high

binding energy do so because this is equivalent to being measured to have a low kinetic energy. The number of secondary electrons rises exponentially towards zero kinetic energy due to the many electrons in the crystal bulk that have been emitted and then undergone multiple loss processes before leaving the surface.

The photoelectrons that are emitted and leave the surface without undergoing loss processes produce intense, narrow photoelectron peaks. These are due to electrons leaving the sample in the ‘photoelectron emission’ step shown in Figure 3.4. These peaks can be identified by looking up the binding energy on reference tables, and hence this type of scan is useful in identifying what elements are present in a sample. Here the photoelectron peaks that can be identified are the Ti $2p$, $3s$ and $3p$, from the crystal surface, the O $1s$, $2s$ and valence band with contributions from both the surface and the adsorbate, and the N $1s$, C $1s$, Ru $3d$ and S $2p$ levels from the adsorbate. Note that the $2p$, $3p$ and $3d$ levels show spin-orbit splitting as explained in Section 3.2.6.

The photon energy used to illuminate the sample in this case was 600 eV. Electrons in various energy levels would then have absorbed a photon with its 600 eV of energy. An electron in the O $1s$ level for example, would then have used ~ 530 eV of this to overcome the binding energy of the O $1s$ level and the combined work function of the sample and the electron analyser, and then been left with a kinetic energy of ~ 70 eV which was measured by the analyser. In contrast, the electrons in the low binding energy valence levels would have used only a small amount of the 600 eV of energy they absorbed from the photon to leave the sample, leaving the emitted photoelectrons travelling fast with ~ 580 -600 eV of kinetic energy.

As shown in Figure 3.4, once a photoelectron has been emitted, the atom or molecule must then relax either via Auger decay or fluorescent decay. The electron analyser does not detect any photons emitted in fluorescent decay, but it does detect Auger electrons. Auger electron peaks can be seen in the wide scan, and are broad and intense. Although the Auger electrons are on a binding energy scale here, it does not make sense to think of them in terms of binding energy. While electronic core levels have a fixed binding energy, Auger electrons have a fixed kinetic energy independent of the ionising radiation. Once the photoelectron has been emitted, any

information about the energy of the absorbed photon is lost and all that remains is a hole that the photoelectron left behind. The energy of the Auger electrons that are then emitted depends only on the difference in energy between the energy levels involved in the decay. If a different photon energy was used to repeat the scan in Figure 3.7 the photoelectron peaks would remain at the same binding energy but the Auger electron peaks would appear shifted on the binding energy scale. This is the same as thinking of the Auger electrons as having a fixed kinetic energy, whereas the kinetic energy of the photoelectrons can change and is dependent upon the photon energy.

3.2.8 Chemical bonding

Figure 3.8 shows a high resolution photoelectron spectrum of a low coverage of N₃ on Au(111). This is an example of the type of spectrum used to obtain information about the chemical states of bonded atoms. These scans are taken using small increments in the measured kinetic energy, and with a high resolution, here ~ 0.15 eV. There are three resolvable peaks in this spectrum, all originating from the N 1s level. The peak types must be identified – photoelectron, Auger, shake up or shake off? In this case they are all photoelectron peaks and they imply that the nitrogen atoms in the molecule are making three different types of chemical bond.

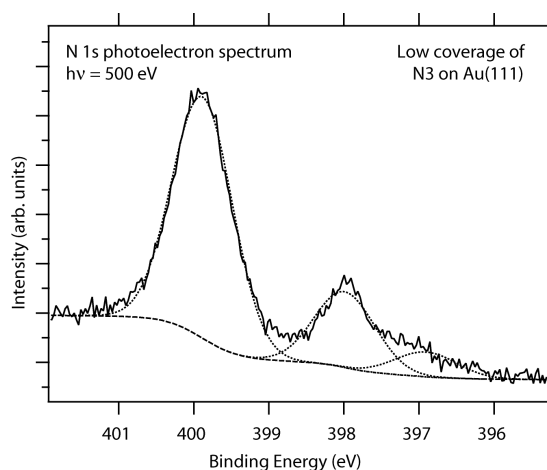


FIGURE 3.8: High resolution N 1s photoelectron spectrum. Here the sample is a low coverage of N₃ on the Au(111) surface.

Note that there is a structure to the background of the peaks. It is called a *Shirley background* and arises because for each extra electron energy level that is accessed, more secondary electrons are produced. An empirical approximation to this background can be fit using software, and removed so that all that remains are the photoelectron peaks. The peaks can then be fit using curve-fitting software. The shape of each peak is a convolution of Lorentzian and Gaussian peak shapes. The Lorentzian component is due to natural broadening of the states ($\Delta E \Delta \tau \leq \hbar/2$) and the Gaussian component to instrumental broadening of both the incident photon beam and the electrons as they pass through the electron analyser.

3.2.9 Data acquisition

In photoemission spectroscopy a sample is irradiated with monoenergetic light and the emitted photoelectrons and Auger electrons are analysed as a function of their kinetic energy. The kinetic energy of the electrons is measured using an electron analyser. An example of an electron analyser is shown schematically in Figure 3.9 and a photograph showing the electron analyser used in this work is shown in Figure 3.10.

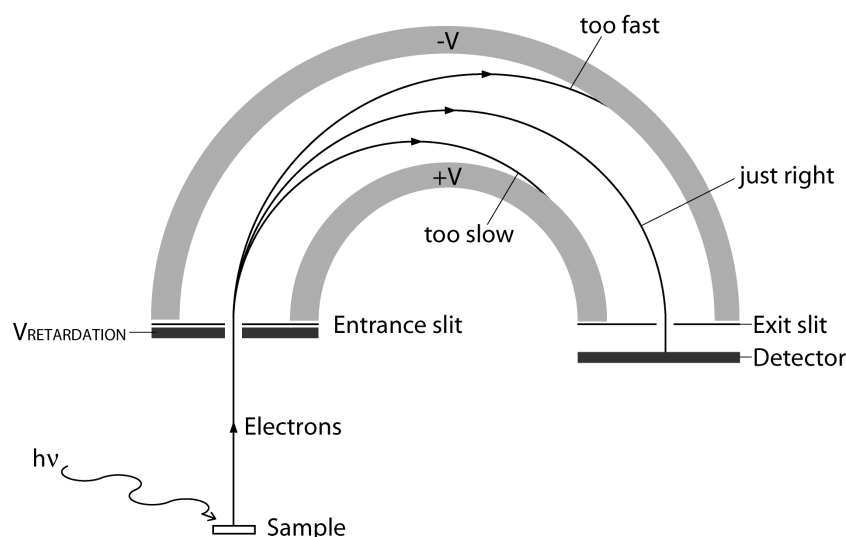


FIGURE 3.9: Hemispherical electron analyser.



FIGURE 3.10: Photograph showing the Scienta R4000 hemispherical electron analyser used in this work. The analyser is here mounted onto the I511-1 end station.

While electrons of all sorts of kinetic energy leave the sample at a given time, the analyser uses electrostatics to only accept electrons that are within a specific kinetic energy range. To get to the detector the electrons must first pass through a mesh held at a potential – the retardation voltage. This is used to accelerate or retard electrons to a kinetic energy suited to the chosen analyser settings. The electrons then pass through the analyser entrance slit, the size of which can be altered; a smaller slit

size gives a higher energy resolution but lowers the overall signal. The electrons then enter the analyser, in between the inner and outer metallic hemispheres. A voltage is applied between the hemispherical plates, the smaller inner plate positive with respect to the larger outer plate. The electric field between the two plates causes the path of the electrons to bend towards the inner positive plate. The faster the electron is travelling, the less its path will be forced to curve, and the slower it is going, the more dramatically its path will turn towards the inner plate. The electrons are therefore spread out spatially according to their kinetic energy. Electrons with too small a kinetic energy are incident upon the inner positive plate where they are neutralised, and similarly, those with too large a kinetic energy are incident upon the outer negative plate.

The electrons can be spread out as much or as little as the user requires by changing the voltage between the plates. The kinetic energy range of the electrons that are allowed to pass through the analyser is called the pass energy and is set to have values typically from 10 to 100 eV. The smaller the pass energy the higher the energy resolution, but fewer electrons reach the detector. The pass energy is therefore a compromise between resolution and signal-to-noise ratio.

Once through the hemispherical plates, the electrons pass through an exit slit and are incident upon a multi-channel plate detector. This is a 2d grid of electron multipliers, upon reaching which a single electron causes a cascade of many more electrons to be released. On the other side of the multi-channel plate detector is a phosphorescent screen, upon which the bursts of electrons are incident. When each multiplied electron event comes through, it causes a point on the screen to phosphoresce. A camera watches this screen and feeds the images into a computer which records the positions on the screen at which the events occur, which are a function of the initial electrons' kinetic energies. These events are accumulated to produce a spectrum of the number of electrons detected as a function of their kinetic energy.

If the voltage settings are left like this during data acquisition it is called fixed mode, with the measured kinetic energy range being defined by the pass energy. More typically, the retardation voltage is incremented by small amounts throughout

the scan so that the kinetic energy of the electrons incident upon the phosphor screen is changed at each increment. In this case the kinetic energy range measured is not limited by the pass energy. This is called swept mode. It has the advantage that long scan ranges can be chosen while maintaining a high resolution, and any non-uniform sensitivity in the phosphor screen is averaged-out.

Although the spectrum is measured as the number of electrons as a function of kinetic energy, for ease of interpretation the analyser software can display the spectrum as the number of detected electrons as a function of their binding energy. This is done *approximately* using the relation:

$$E_{\text{B(UNCALIBRATED)}} = h\nu - E_{\text{K}}. \quad (3.2)$$

The spectrum is then on a binding energy scale but its shift on that scale is not calibrated. This is because the work function of the analyser is not known and because the photon energy set by the user may not be the true photon energy shone upon the sample. The spectrum can be calibrated by using a known feature in the spectrum. For metals, the binding energy is referenced to the Fermi level defined to be at 0 eV. For semiconductors, it is either referenced to the Fermi level or the vacuum level. One cannot directly measure the Fermi level of a semiconductor since it has no density of states there, but the Fermi level of the metallic sample holder can be measured which is assumed to be aligned with that of the semiconductor crystal by virtue of being in contact with it. If the Fermi level cannot be measured, or if one prefers, binding energy can be referenced to the vacuum level. Figure 3.11 shows the steps involved in going from the measured kinetic energy spectrum to a calibrated binding energy spectrum.

3.2.10 Surface sensitivity

In surface science experiments it is important to try to obtain as much signal as possible from the surface region of the sample and as little as possible from the sample bulk. In Section 2.6 it was discussed how the geometry of sample illumination is important. Here, the choice of photon energy of the illuminating radiation is

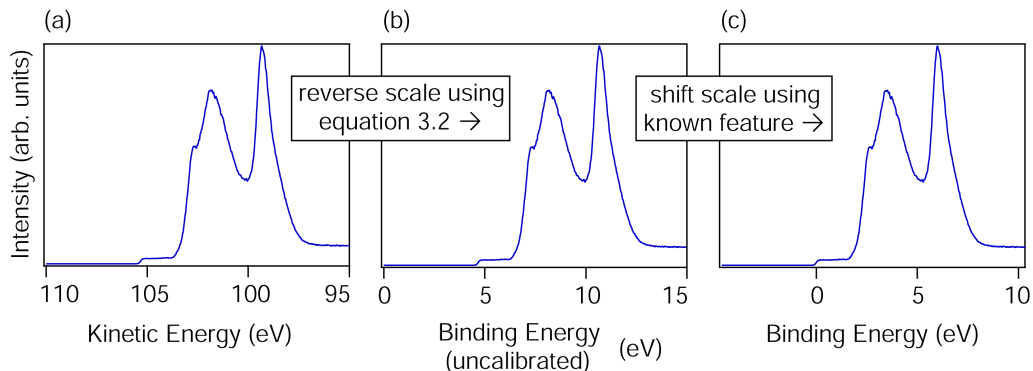


FIGURE 3.11: Steps to calibrate the binding energy of a photoelectron spectrum. Here a photoelectron spectrum was recorded of the Au(111) valence band, measured using $h\nu = 110$ eV. Graph (a) shows the photoelectron spectrum as directly measured on a kinetic energy scale, followed by (b) conversion to an uncalibrated binding energy scale via equation 3.2, and finally (c) calibration to a known feature, here the Fermi level at 0 eV binding energy.

discussed, in terms of how to obtain the most surface-sensitive results.

When electrons travel through a solid they can undergo loss processes, i.e. they can be *inelastically scattered*. These electrons have then lost the information about the energy level or Auger transition from which they came and contribute to a background of uninformative secondary electrons. As for the electrons that are *not* inelastically scattered, and contribute to photoelectron and Auger peaks, we want these to originate from as high up in the crystal as possible so that they come from the surface and not the crystal bulk. Electrons that travel a short distance before scattering are therefore preferred to those that travel a long distance before scattering and can thus come from deeper in the sample. A measure of how far an electron travels on average before losing energy is its *inelastic mean free path*, $\lambda(E)$. This is defined by the equation:

$$I(d) = I_0 \exp(-d/\lambda(E)), \quad (3.3)$$

where $I(d)$ is the intensity of an electron beam after travelling a distance, d , through a material, where the original intensity was I_0 . The inelastic mean free path, $\lambda(E)$, is therefore defined as the distance an electron beam travels before its intensity is

reduced to $\frac{1}{e}$ (~ 0.37) of its initial value.

The mean free path of electrons does not vary much depending on the material they are in but it does depend very much upon the kinetic energy of the electrons. This relationship is described by the empirically found *universal curve* shown in Figure 3.12 which shows the inelastic mean free path of an electron in a solid as a function of its kinetic energy.

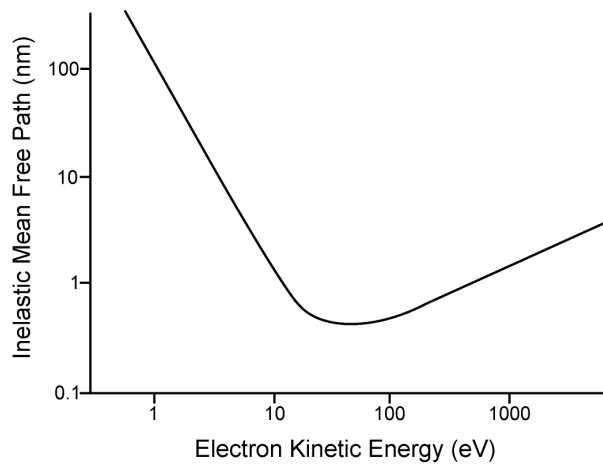


FIGURE 3.12: Universal curve showing the inelastic mean free path of an electron in a solid as a function of its kinetic energy. Figure adapted from Reference [41].

Recall that for the most surface-sensitive results, the shortest possible mean free path is required. The shortest mean free path is seen as the minimum on this plot, in the kinetic energy region of approximately 40-100 eV. Either side of this minimum there are two competing processes causing the inelastic mean free path to increase. To higher kinetic energy, the electrons are travelling faster and are in the solid for less time so have less chance of an interaction. To lower kinetic energy, these low-energy electrons do not have *enough* energy to excite loss processes and so are also more likely to travel through the solid unperturbed, and hence can originate from lower in the sample. For the most surface-sensitive results possible then, the electrons should have approximately 50 eV kinetic energy. In experiments, a photon energy is chosen that is approximately 50 eV larger than the binding energy of the level being studied so that photoelectrons emitted from this energy level have approximately 50 eV kinetic energy.

3.3 Near-edge x-ray absorption fine structure spectroscopy

In Section 3.2 the technique of photoemission spectroscopy was described, in which one can experimentally determine the *occupied* electronic states of a sample. Here, a technique called near-edge x-ray absorption fine structure (NEXAFS) spectroscopy is described, with which one can experimentally determine the *unoccupied* electronic states of a sample. In photoemission spectroscopy, electrons are already in the levels of interest and simply need to be ejected, using photons, and have their kinetic energy measured. To measure the unoccupied states where there are no electrons to begin with is a little more complicated, but builds on the understanding of the processes described in Section 3.2.

Since an atom or molecule in its ground state has no electrons in its unoccupied levels, to find out information about these levels one has to first put electrons into them. This is done by photoexcitation of electrons from a well-defined core level, giving them enough energy to get above the Fermi level and into bound unoccupied states, but not so much energy that they go above the vacuum level and escape. A schematic energy level diagram showing the processes involved in NEXAFS spectroscopy is shown in Figure 3.13.

Once the photoexcitation step has taken place, the atom or molecule is then in a short-lived excited state, before decaying into a more stable state by an electron filling the core hole, and either an electron or photon simultaneously being ejected so that energy is conserved. The fluorescent decay is the same process as in photoemission except for the presence of an extra electron which has a small effect on the energy of the emitted particle. When an electron is emitted, the decay process either involves the originally excited electron, termed participator decay, or it does not, termed spectator decay. This differentiation becomes important in Chapter 4.

The key to understanding NEXAFS spectroscopy is that Auger electrons are only emitted, and measured, when the energy of the photon put into the system is exactly that required to move an electron from the core level of choice to an unoccupied level. If the photon energy does not match the energy difference between the core level and an unoccupied level, no photoexcitation occurs and no Auger electrons are emitted.

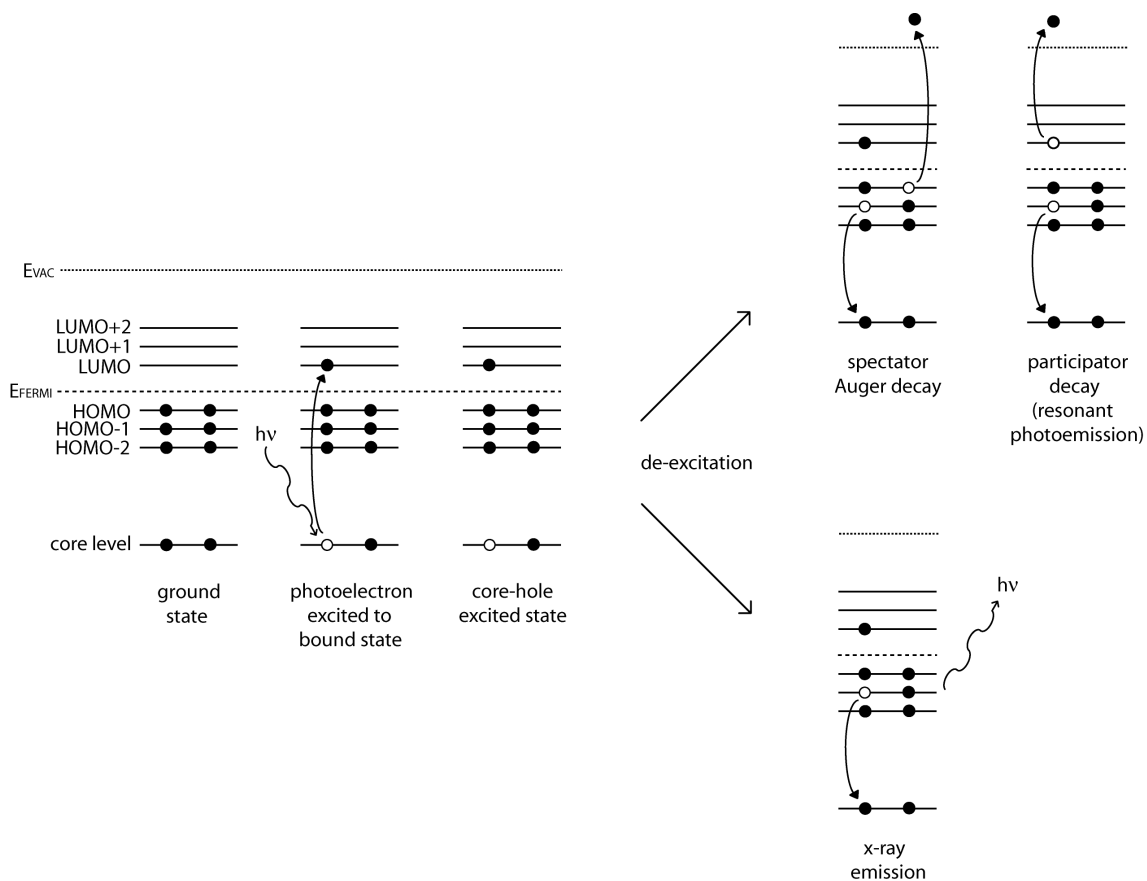


FIGURE 3.13: Energy level diagrams depicting the processes involved in NEXAFS spectroscopy for a molecule. In the molecule's ground state, an electron in a core level absorbs a photon with energy $h\nu$, the exact amount it needs to move to an unoccupied electronic energy level. This leaves the molecule in an excited state as it has a core hole. The molecule then relaxes via an electron dropping to fill the core hole, and either emission of an electron or a photon.

In data acquisition, one starts by illuminating the sample with a photon energy just smaller than that needed to excite an electron into the lowest unoccupied level. No photoexcitation can occur and thus no decay events occur and no Auger electrons corresponding to that particular decay channel are detected. The photon energy is incremented to higher values and eventually is large enough to excite an electron into an unoccupied level. Decay processes then occur at this photon energy, and electrons are detected. In NEXAFS spectroscopy it is not important what energy the emitted Auger electrons have, it is only important whether they are emitted or not. The unoccupied levels are mapped in this way, by incrementing the photon energy and measuring the number of electrons detected at each photon energy value. An example of a NEXAFS spectrum is shown in Figure 3.14.

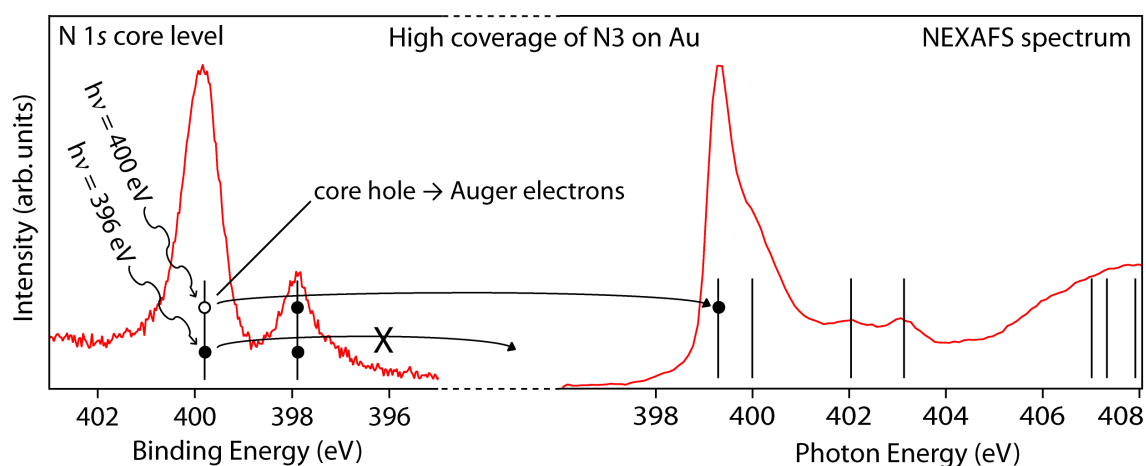


FIGURE 3.14: Experimental N 1s NEXAFS spectrum taken for a monolayer of N3 on TiO_2 . The N 1s core level and a schematic energy level diagram are superimposed, showing that no photoexcitation and subsequent decay events can occur when $h\nu$ is too small, but that when the photon energy is on-resonance, photoexcitation can occur (leading to decay events being detected).

Electrons can be collected using a partial yield detector, in which electrons of all kinetic energies are counted apart from those secondary electrons cut out by a retardation plate held at a positive potential. Another way to acquire a NEXAFS spectrum is to measure the current on the sample, as the number of electrons leaving the sample is enough to produce a measurable current. In this work an electron anal-

yser was used to take NEXAFS spectra. This technique gives the added information of the kinetic energy distribution of the electrons, which is useful to see whether a photoemission peak has drifted into the data which would give spurious results. Since the electron analyser can only measure a certain window of electron kinetic energies, it was used either in ‘Auger yield’ where Auger electrons associated with a certain core level are collected, or ‘secondary electron yield’ which counts the background secondary electrons, and uses the fact that when on resonance, more of these are produced.

3.4 X-ray emission spectroscopy

X-ray emission spectroscopy (XES) is a powerful technique that can be used as an ‘atom-specific probe’ of the valence band. If the valence band is studied using photoemission, valence electrons from all over the molecule are ejected and the full complement of valence levels is measured. In XES, one can choose to look at valence levels that are local to a particular element. The first step of the process, shown schematically in Figure 3.15, is to create a core hole by photoemission of a core electron to above the vacuum level. One can choose where to create the core hole by illumination with photons with an energy ~ 20 eV higher than the binding energy of the core level, ensuring that the core electron has enough energy to go above the vacuum level. The core hole then decays by a valence electron filling it, and an electron or photon being simultaneously ejected. In XES, the energies of the outgoing photons are measured and these correspond to energy differences between various levels in the valence band, and the core hole.

The atom specificity comes in because the valence electrons can only decay to a core hole if there is some spatial overlap of the valence orbital with the core level. The x-ray emission spectrum thus only shows those valence levels that are local to the atom containing the core hole. An additional constraint is that only certain electronic transitions are *allowed*, governed by the orbital rule, $\Delta l = \pm 1$, and the spin rule, $\Delta S = 0$. The orbital rule implies that transitions are only allowed between certain orbitals, and cannot occur within the same orbital. The spin rule implies that

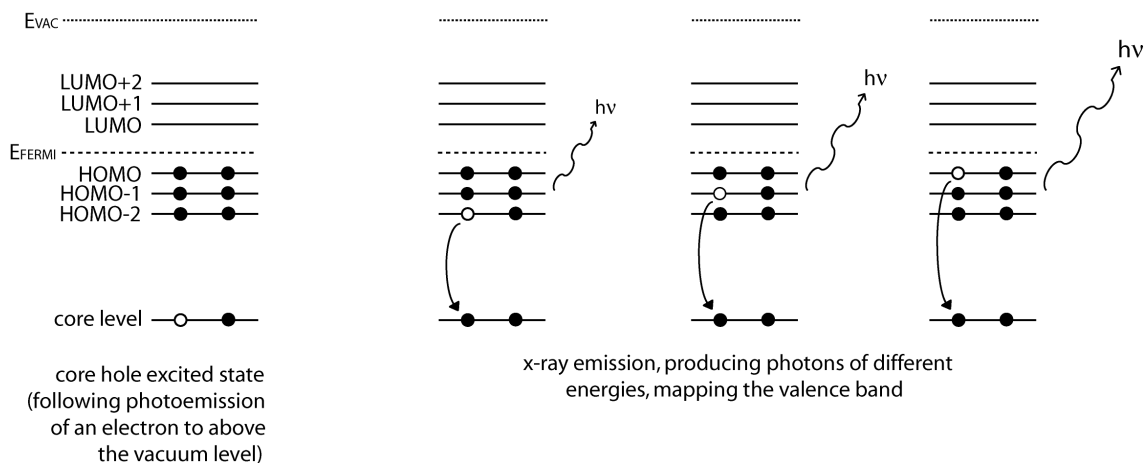


FIGURE 3.15: Energy level diagrams depicting the x-ray emission process for a molecule. A core hole is created by photoemission of an electron to above the vacuum level. The system is then in an excited state, and de-excites by an electron dropping from the valence band to fill the core hole, and simultaneous emission of a photon or electron. In x-ray emission, the emitted photon has the same energy that the electron lost, and the energies of these photons are measured to map the valence band.

electrons that make a transition do so without a change in their spin. For example, an electron can make a transition $s \rightarrow p$ or $d \rightarrow p$, but not $s \rightarrow s$ or $s \rightarrow d$. For C, N and O which only have electrons in the $1s$, $2s$ and $2p$ electronic levels, the orbital rule implies that the $1s$ core level can only be filled by molecular orbitals with $2p$ character.[42] The complicated valence band structure can thus be broken down so that peaks are identified as molecular orbitals that overlap with particular elements.

The technique of x-ray emission spectroscopy is not as widely used as photoemission spectroscopy because for elements of low atomic number a core hole decays predominantly by Auger decay rather than x-ray emission. A comparison of Auger yield and fluorescence yield as a function of atomic number has already been shown in Figure 3.5. Since interesting molecules often include atoms such as carbon, nitrogen and oxygen, with atomic numbers of 6, 7 and 8 respectively, x-ray emission spectroscopy of surfaces is often not considered a worthwhile use of time at a synchrotron because it takes so long to count enough photons to produce a spectrum with good signal-to-noise.

However, with a set-up designed specifically for x-ray emission of surfaces such as that at the I511-1 end station (described in Section 2.5), one can accumulate counts over several hours resulting in x-ray emission spectra with a fairly good signal-to-noise ratio. These spectra unveil information about the electronic structure of a sample that photoemission cannot. XES is usually considered to be a bulk technique because the escape depth of the emitted photons is large in comparison to the depth of the adsorbed layer(s). It can, however, be made surface-sensitive by using grazing incidence radiation as discussed in Section 2.6, and by exciting from core holes of elements that are only present in the adsorbate and not in the substrate. An example of an x-ray emission spectrum is shown in Figure 3.16.

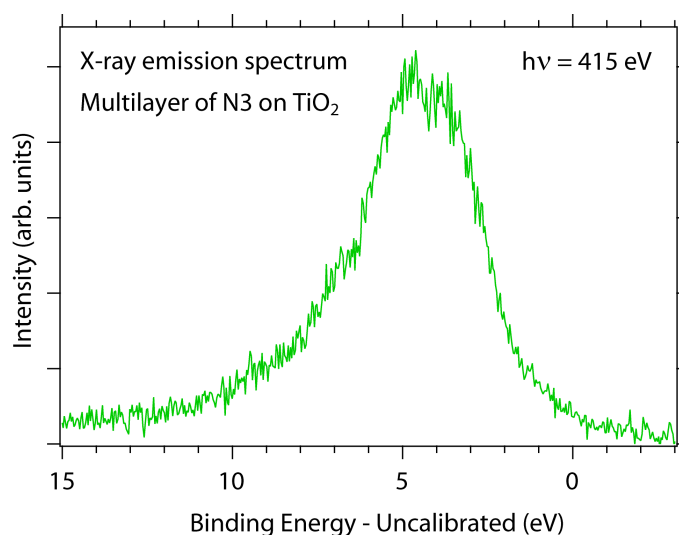


FIGURE 3.16: N $1s$ x-ray emission spectrum taken for a multilayer of N3 on TiO₂(110). The data was collected on a photon energy scale, and this has been converted to a binding energy scale by referencing to the binding energy of the N $1s$ core level, and reversing the scale.

3.5 Density functional theory

In this section a brief introduction to density functional theory (DFT) is given before explaining some of its uses. The theory is then described in a little more detail. Finally an overview is given of the particular formulation of DFT used in this work.

Density functional theory is a theoretical framework based on quantum mechanics, with which one can describe matter. Calculations made based on this theory predict observable quantities such as the positions of atoms in a molecule. These theoretical calculations help to increase understanding of how matter acts on the small length scales of atoms and molecules, and when calculations agree with experiment, one can have increased confidence in these results.

The simplest use of DFT is to calculate the geometry of a molecule. Calculations find the atomic positions that give the lowest total energy and therefore the most stable geometry. It can also be used to calculate the geometry of a molecule on a surface, which works with the same principles but has more atoms to consider. As well as predicting geometries, it can also be used to calculate properties of the electrons such as their binding energies and spatial distribution. Figure 3.17 shows the optimised geometry of a free N₃ molecule (i.e. an isolated N₃ molecule in vacuum) and also the spatial distribution of the HOMO, both calculated using the DFT software CASTEP[8]. The spatial coordinates that were calculated are rendered as an image using Materials Visualizer, software included in the DFT package Materials Studio.

DFT is not a full quantum mechanical description of matter, as to fully model a system comprising more than a few atoms would require too much computing power to perform. Constrained by computing power, approximations must be made to the full theory in order to run calculations. The trick is to cut out or simplify the parts of the theory that are computationally expensive, but only have a negligible effect on the end result.

Since DFT is not a primary focus of this work, a brief overview only is given here. The reader is directed to Capelle [43] if interested in a more thorough description.

All possible information about a single electron moving in a potential, $v(\mathbf{r})$, can be written in the Schrödinger equation:

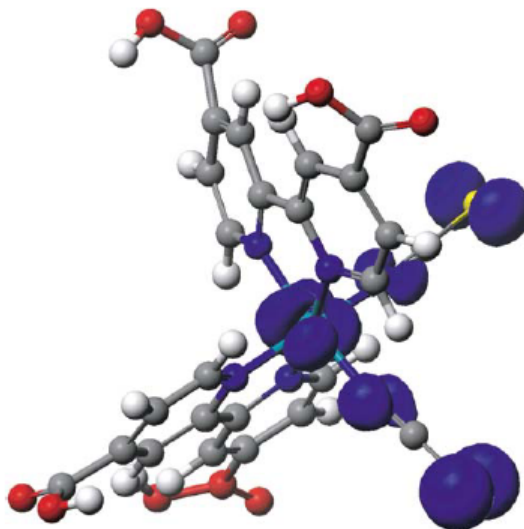


FIGURE 3.17: Geometry-optimised free N3 molecule showing the HOMO in blue, calculated using CASTEP[8].

$$\left[-\frac{\hbar^2 \nabla^2}{2m} + v(\mathbf{r}) \right] \Psi(\mathbf{r}) = \epsilon \Psi(\mathbf{r}), \quad (3.4)$$

where $-\hbar^2 \nabla^2 / 2m$ is the kinetic energy operator, and $v(\mathbf{r})$ the potential energy operator, both of which act on a wavefunction, $\Psi(\mathbf{r})$, that describes a single electron. The sum of the kinetic and potential energy of the electron is equal to ϵ , its total energy.

While this describes a single electron, an extra level of complexity is introduced when one considers, for example, a hydrogen atom. The addition of a nucleus contributes to the total energy of the system. Like an electron, a nucleus has kinetic and potential energy. This, however, is where one of the simplifications to the full theory is made. Since nuclei are very massive compared to electrons, they move much more slowly. As an approximation their velocities are treated as negligible in DFT, and the kinetic energy term for the nuclei is thrown away. This is called the Born-Oppenheimer approximation. There then remains a nuclear potential energy term which can be incorporated into the potential, $v(\mathbf{r})$, acting on the electron. The Schrödinger equation describing a hydrogen atom thus remains the same as that for an electron, with these approximations.

A further level of complexity comes when considering systems with more than one

electron, as then there is an additional energy term due to the interaction between the electrons. Schrödinger's equation becomes:

$$\left[\sum_i^N \left(-\frac{\hbar^2 \nabla_i^2}{2m} + v(\mathbf{r}_i) \right) + \sum_{i<j} U(\mathbf{r}_i, \mathbf{r}_j) \right] \Psi(\mathbf{r}_1, \mathbf{r}_2, \dots, \mathbf{r}_N) = \epsilon \Psi(\mathbf{r}_1, \mathbf{r}_2, \dots, \mathbf{r}_N), \quad (3.5)$$

where N is the number of electrons and $U(\mathbf{r}_i, \mathbf{r}_j)$ is the electron-electron interaction. The equation can be written more simply, in terms of operators:

$$\left[\sum_i^N (\hat{T} + \hat{V}) + \sum_{i<j} \hat{U} \right] \Psi(\mathbf{r}_1, \mathbf{r}_2, \dots, \mathbf{r}_N) = \epsilon \Psi(\mathbf{r}_1, \mathbf{r}_2, \dots, \mathbf{r}_N), \quad (3.6)$$

where for example, for a Coulombic potential and non-relativistic atomic system,

$$\hat{T} = -\frac{\hbar^2}{2m} \sum_i \nabla_i^2; \quad (3.7)$$

$$\hat{U} = \sum_{i<j} U(\mathbf{r}_i, \mathbf{r}_j) = \sum_{i<j} \frac{q^2}{|\mathbf{r}_i - \mathbf{r}_j|}; \quad (3.8)$$

$$\hat{V} = \sum_i v(\mathbf{r}_i) = \sum_i \frac{Qq}{|\mathbf{r}_i - \mathbf{R}|}, \quad (3.9)$$

where q and \mathbf{r} are the electronic charge and positions, and Q and \mathbf{R} are the nuclear charge and positions.

Note that \hat{T} and \hat{U} are universal, in that they apply for any Coulombic potential, non-relativistic atomic system. \hat{V} , however, is system-dependent, in this case depending upon the position of the nuclei. Usually then, when solving the Schrödinger equation one specifies the external potential, $v(\mathbf{r})$, to represent the system of choice, uses this to find the wavefunction, $\Psi(\mathbf{r})$, then calculates observables by taking the expectation values of operators such as \hat{T} and \hat{U} .

One of the observables that can be calculated in this way is the electron density,

$$n(\mathbf{r}) = N \int d^3r_2 \int d^3r_3 \dots \int d^3r_N \Psi^*(\mathbf{r}, \mathbf{r}_2, \dots, \mathbf{r}_N) \Psi(\mathbf{r}, \mathbf{r}_2, \dots, \mathbf{r}_N). \quad (3.10)$$

At the moment, the variable upon which everything depends is the positions of the electrons, \mathbf{r} . A mathematical step can be performed in which everything is made to depend on $n(\mathbf{r})$, rather than \mathbf{r} itself. Whereas previously the operators such as \hat{U} and \hat{V} depended on \mathbf{r} , they are now dependent upon $n(\mathbf{r})$, which is, itself, dependent upon \mathbf{r} . Since a function of a function is called a functional, and the new variable is the number density of the electrons, $n(\mathbf{r})$, the theory gets its name: density functional theory. Through making the approximations described and changing the key variable, the theory is simplified enough that calculations can be run to describe systems with many electrons and nuclei.

Within DFT there are many different variations that suit different types of physical system. In this work a software package called CASTEP[8] was used. In this formulation of DFT, Bloch's theorem is used in which the wavefunctions are made periodic by assigning a cell-periodic factor and a phase factor. This means that when modelling a surface it can be thought of as going out to infinity in all directions. Without the periodic boundary conditions a small piece of surface would curl at the edges, oblivious to the fact that in reality there would be more surface to interact with next to it. This cuts down calculation costs, as one can model the unit cell of a surface, containing only a few atoms, rather than a large chunk. Another way in which calculation costs are cut in CASTEP is to use pseudopotentials. These are equations used to replace both the potential from the nucleus and the interaction with core electrons with a single 'effective potential'.

3.6 Scanning tunnelling microscopy

Scanning tunnelling microscopy (STM) is an imaging technique that enables visualisation of surfaces on the nanometre scale. We are used to imaging techniques where photons of optical light are reflected from a surface, through lenses, into our eyes. This technique is different in that it does not 'look' at a surface, it 'feels' a surface. STM is in a family of microscopy techniques called scanning probe microscopy, in which probes are used to physically contact the surface.

In STM an atomically sharp, metallic tip is used to measure the electronic density

of states of a surface. A potential difference is applied between the tip and the surface, and the tip is very slowly brought towards the surface. Eventually, at a threshold distance, electrons can quantum-tunnel through the air or vacuum, and a current is measured. The closer the tip is to the sample, the higher the current. The STM tunnel current is exponentially dependent on the tip-sample separation distance which makes the technique very sensitive; close to the surface, a small change in separation is marked by a large change in current. By measuring the current at a grid of points covering the sample surface and feeding this information into a computer, an image can be formed showing the height of the uppermost electronic orbitals.

Since the values of current and distance involved in this microscopy are so small, it is important to cut out mechanical noise by mounting the microscope on a vibration-reducing device, and to cut out electrical noise as much as possible. As with all surface science techniques, the cleaner the surface the better, so for the best possible results the STM and sample are mounted within a vacuum chamber.

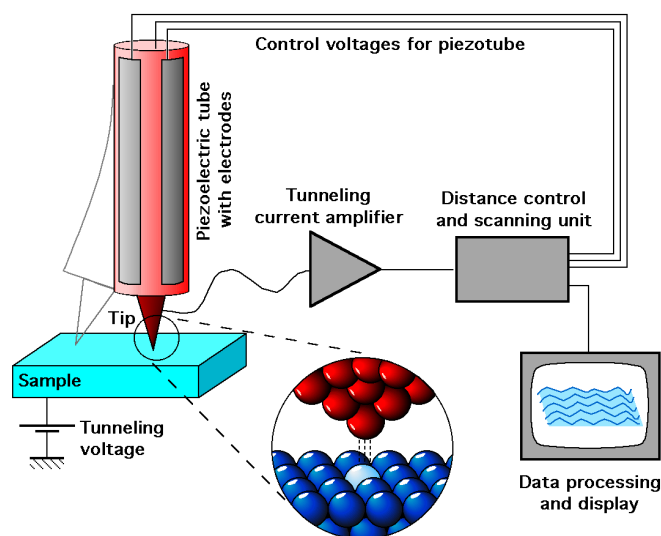


FIGURE 3.18: Schematic figure of an STM[44].

A schematic illustration of an STM is shown in Figure 3.18. To move the tip relative to the sample, either the tip or the sample is mounted on a piezoelectric crystal. This is a type of crystal that contracts or expands when a voltage is applied

across it, and they are used here as they can be moved accurately over small distances. The tip is rastered in the surface plane in order to build up an image line-by-line. So that the tip does not crash into the surface if it reaches a feature, the distance from the tip to the sample is continually adjusted according to the values of current measured. A fixed value for the current is chosen when using this ‘constant-current’ mode of operation. If the current measured is too high, this means that the tip is getting too close to the surface due a feature sticking out, and the tip-sample distance is increased. If the current measured is too low, a trough in the sample has been reached and the tip-sample distance is decreased.

With a very high-quality STM system, atomic resolution can be reached, or even sub-atomic resolution showing the shapes of electronic orbitals. In this work the purpose of using STM is to measure the distribution of molecules across a surface. Figure 3.19 shows images recorded of N₃ on the Au(111) surface. In 3.19 (a) it can be seen that the molecules are arranged in some ordered manner on the surface. Figure 3.19 (b) shows a smaller area of the sample in which the individual molecules can be resolved. These images are useful as they show the distribution of molecules across the surface at different coverages. STM images can be tied in with photoemission and DFT studies, and together these provide a broad complement of techniques revealing how molecules adsorb to surfaces.

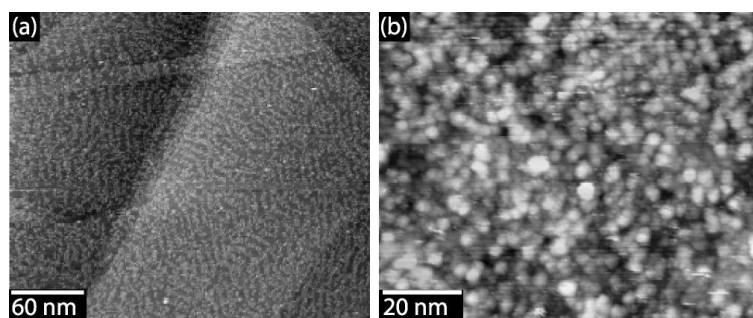


FIGURE 3.19: STM images showing (a) a sub-monolayer and (b) a monolayer of N₃ on Au(111).

CHAPTER 4

Molecule-to-substrate charge transfer

4.1 Introduction

This chapter describes the experimental techniques used in this work to study the transfer of charge between a molecule and a surface to which it is adsorbed. The molecule-surface systems studied here are models for parts of DSCs:

- The N3 molecule adsorbed to the $\text{TiO}_2(110)$ surface models the charge separation and electron injection part of what is the most efficient DSC to date.[9] The motivation for this work is to discover what makes this particular molecule-surface system so good at charge separation and electron injection. This must be understood as clearly as possible in order to fully appreciate the qualities that make an efficient DSC.
- The N3 molecule adsorbed to the Au(111) surface is a newly studied system which could potentially be used in future DSC designs. Here, it is suggested that Au could act in the role that the electrolyte usually serves – as a means to replenish the N3 molecules with electrons. In this case the study of electron injection from the Au surface into the N3 molecule is important.

In the previous chapter, techniques were described to study how molecules adsorb to surfaces. This work, interesting in itself, is also a precursor for trying to understand how charge moves in the systems studied. The techniques described in this chapter,

when combined with adsorption studies, can unveil the electronic and spatial journey that photoexcited electrons travel as well as the timescale on which they do so.

Chapter 1 described the way in which DSCs function; a photon of visible light is absorbed by a dye molecule, photoexciting an electron from the molecule's valence band to one of its unoccupied levels, from which the electron then transfers into the conduction band of the substrate. There are many energy levels in the valence band, so many different combinations of occupied and unoccupied levels are involved in the transitions. This would be a complicated process to extract charge transfer information from. Ideally, we would like to excite electrons from one, narrow, known energy level to the many unoccupied levels, to keep the process as simple as possible. The closest we can get to this in reality is to excite electrons from a core level. This mimics excitation of electrons from valence levels in the working DSC. Charge transfer from a core-excited state is expected to be very similar to that from valence-excited states.[45]

The experimental techniques described in this chapter are all resonant spectroscopies. These are spectroscopies for which the first step is photoexcitation of an electron from a core level to an unoccupied level, termed *x-ray absorption*. When the incident photon energy is tuned to the energy difference between a core level and an unoccupied level, x-ray absorption can occur. At this photon energy the recorded spectrum is said to be *on-resonance*.

So, what is special about resonant spectroscopies that means they can provide information about charge transfer? After x-ray absorption the molecule is in an excited state and needs to relax via some decay mechanism. Before that decay event occurs, it is possible that the electron in the unoccupied level transfers away, leaving the molecule entirely. One can detect the electrons or photons that are emitted in the subsequent decay events, and by analysing their energy can determine whether or not the photoexcited electron was still present when the decay event occurred. When the decay events show that the photoexcited electron was not present, we assume that the electron has either transferred to a neighbouring molecule, a neighbouring ligand on the same molecule, or into the substrate which in DSC language is referred to as *electron injection*.

The lifetime of a core hole is very short – on the order of a few femtoseconds. By comparing the number of decay events where charge transfer took place first, to the number where the core hole was filled first, one can measure charge transfer on the femtosecond timescale. Rather than timing the charge transfer event itself, we let it compete with the process of core-hole decay, and look at the emitted electrons or photons to deduce how much of each process occurred.

The next section of this chapter discusses energy level alignment diagrams, in which the occupied and unoccupied levels of an adsorbate are put onto a common energy scale, along with those of the substrate. This is an important step which allows one to see where the energy levels of the molecule lie with respect to those of the substrate. Resonant electron spectroscopy is then discussed, in which the energy of electrons emitted in core-hole decay are measured, before going on to describe the core-hole clock method, which enables quantification of the timescale on which charge transfer occurs. Finally, resonant x-ray emission spectroscopy is discussed, offering a further insight into charge transfer. In this technique, the energy of photons emitted in core-hole decay are measured.

4.2 Energy level alignment

When studying charge transfer between two systems it is useful to see how the electronic energy levels in each system overlap. In doing so, one discovers which transitions are possible; an electron can only tunnel into a neighbouring system if the energy level it is in overlaps with unoccupied levels of the neighbouring system. An electron cannot tunnel into a filled energy level or a band gap.

An energy level alignment diagram is shown in Figure 4.1 (a). The occupied levels of a clean surface, and of a surface with a layer of adsorbed molecules, can be measured using photoemission spectroscopy as described in Section 3.2. The unoccupied levels of the surface with molecules adsorbed to it can be found using NEXAFS spectroscopy, as described in Section 3.3. If the substrate has a band gap, this can be found through optical studies and placed at the top of the measured valence band. The top end of the band gap then defines the start of the substrate conduction band.

In a metallic substrate this last step is not necessary because there is no band gap, so the conduction band begins where the valence band ends. The spectra cannot immediately be placed on a common axis because the photoemission spectra are on a binding energy scale, whereas the NEXAFS spectra are recorded on a photon energy scale. First the NEXAFS spectra must be placed on a binding energy scale following the procedure outlined below. Once all spectra are on a binding energy scale they can be displayed on a common axis showing both the occupied and unoccupied levels.[46]

To help understand how the binding energy scale and photon energy scale are related, Figure 4.1 (b) shows schematic electronic energy level diagrams with the binding energy marked on the photoemission diagram and the exciting photon energy marked on the NEXAFS diagram. Figure 4.2 is included as an aid to understanding how to take a NEXAFS spectrum on a photon energy scale and transpose it onto a binding energy scale. The basic concept is that the unoccupied levels are initially measured relative to the core level, and to make them instead relative to the Fermi level one must take into account the binding energy of the core level referenced to the Fermi level. The individual steps involved are described below.

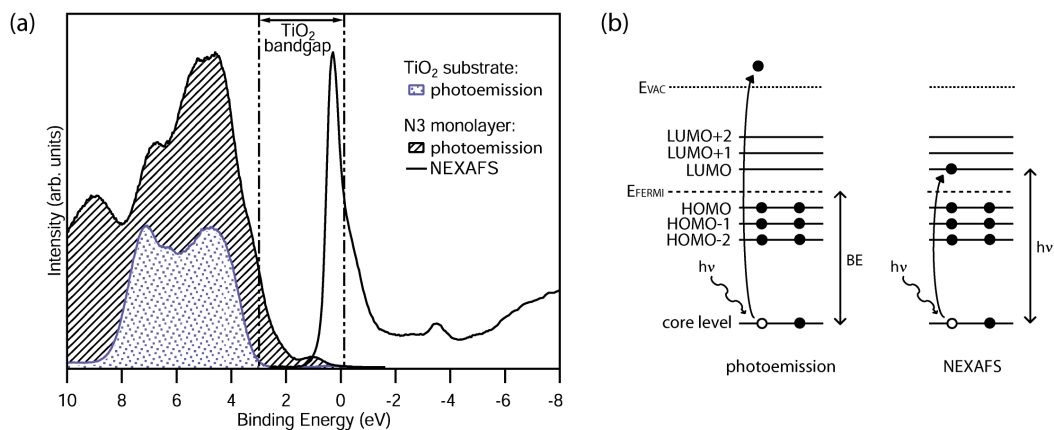


FIGURE 4.1: Part (a) shows valence band photoemission spectra of the clean $\text{TiO}_2(110)$ surface and of a monolayer of N3 adsorbed to this surface, adjacent to a N $1s$ NEXAFS spectrum of the N3 monolayer, converted from a photon energy scale to a binding energy scale. The band gap of the TiO_2 surface is shown,[17] with occupied levels to higher binding energy, and a continuum of unoccupied levels to lower binding energy. Part (b) shows schematic electronic energy level diagrams to illustrate how the different spectra are related.

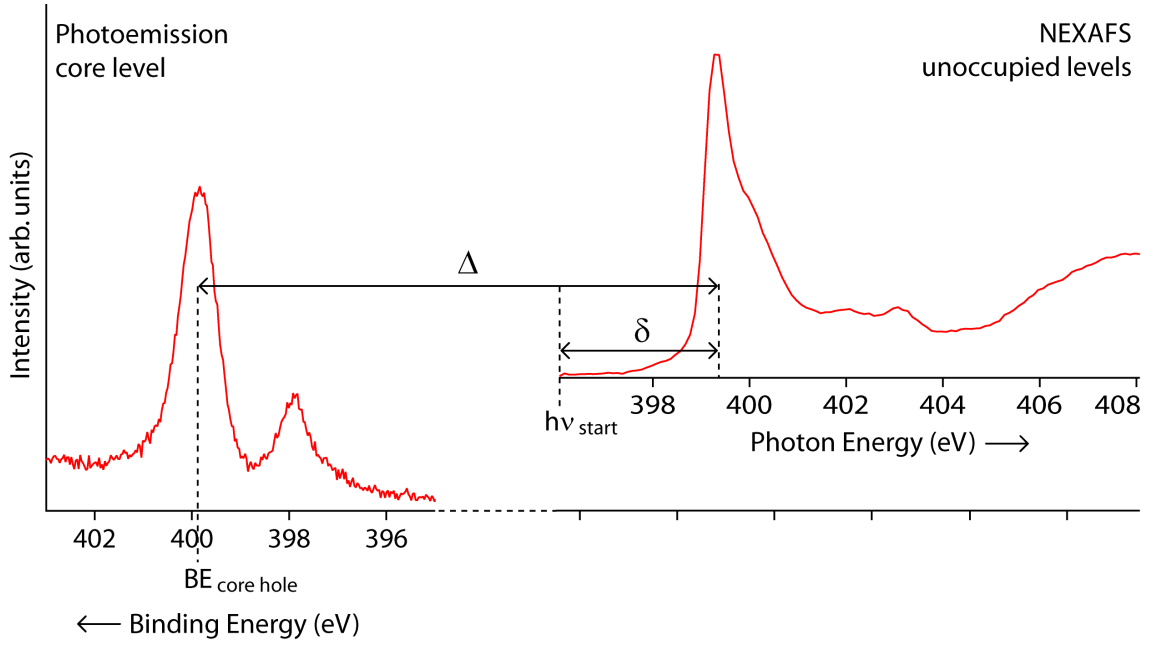


FIGURE 4.2: Schematic figure to illustrate how a NEXAFS spectrum can be put on a binding energy scale.

Let us define the binding energy of any point on the NEXAFS spectrum as being $-\Delta$ relative to the binding energy of the core hole:

$$BE_{\text{NEXAFS}} = -\Delta \text{ relative to } BE_{\text{core hole}} \quad (4.1)$$

The binding energy of the core hole can be calibrated relative to the Fermi level at 0 eV:

$$BE_{\text{core hole}} = BE_{\text{core hole}} \text{ relative to } 0 \text{ eV} \quad (4.2)$$

Equations 4.1 and 4.2 lead to Equation 4.3 being true.

$$BE_{\text{NEXAFS}} = (-\Delta + BE_{\text{core hole}}) \text{ relative to } 0 \text{ eV} \quad (4.3)$$

We can then substitute the definition of Δ (Equation 4.4) into Equation 4.3 to obtain Equation 4.5. The binding energy of the NEXAFS spectrum is then written in terms of known quantities, so that the unoccupied levels found through NEXAFS

can be transposed onto a binding energy scale, and put on a common axis with the occupied levels.

$$\Delta = h\nu_{\text{start}} + \delta \quad (4.4)$$

$$\text{BE}_{\text{NEXAFS}} = \text{BE}_{\text{core hole}} - h\nu_{\text{start}} - \delta \quad (4.5)$$

Note that the photon energy in the NEXAFS spectrum should be calibrated. This can be done, for example, by not moving the monochromator following the NEXAFS scan, and measuring the photoemission spectrum of a core level with both first and second order light. The shift in kinetic energy of these two spectra gives the true photon energy.

Figure 4.1 reveals from which levels it is possible to get charge transfer between the adsorbate and the surface. For the lowest unoccupied level of the adsorbate, seen here as the most intense peak in the NEXAFS spectrum, an electron excited to this level cannot transfer into the surface because its energy overlaps with the surface band gap. For adsorbate unoccupied levels with ‘binding energies’ lower than the surface conduction band edge at ~ 0 eV, electron injection from these levels into the surface can occur. In this example which uses a TiO_2 substrate, the Fermi level is very close to the top of the band gap due to doping. It is useful to have an adsorbate unoccupied level from which electron injection cannot occur, as the amount of decay events seen for this level can be used as a reference to which charge transfer from other levels can be compared.

It is important to note that these figures represent the energy alignment of core-excited systems, as opposed to systems in their ground state. The presence of a core hole shifts the unoccupied levels slightly higher on a binding energy scale, on the order of eV. This is taken into account and in fact used to discover extra information in the results chapters.

4.3 Core-level resonant electron spectroscopy

Core-level resonant electron spectroscopy is a very important technique in this work. It enables one to observe the delocalisation of electrons from unoccupied molecular levels. This allows quantification of electron transfer times in our model DSC systems. Here the different processes are described that can occur following an electron being resonantly excited from a core level to an unoccupied level. In this section, only those decay events that involve emission of an electron are discussed; the next section in this chapter looks at decay events involving emission of photons. Data acquisition and identification of features are then discussed, and finally the core-hole clock method is described, which allows one to extract charge transfer timescales from the data.

4.3.1 Resonant electron processes

The various processes that lead to an electron being ejected following x-ray absorption are shown in Figure 4.3. Here, semiconductor substrates are shown, which is relevant for the work involving TiO_2 . The work involving a Au substrate differs in terms of the energy level diagrams in that there is no band gap. Figure 4.3 (a) shows the case where a core electron is photoexcited to an unoccupied bound state that overlaps with the substrate band gap. No charge transfer can occur from the molecule to the substrate because there are no states for the excited electron to move to. The excited state then decays...

The first type of decay event illustrated is identical to normal Auger decay but for the addition of the photoexcited electron present in an unoccupied level, and is called *resonant Auger decay*. It is also called *spectator decay*, as the excited electron spectates but does not take part in the decay itself. Since the excited electron is not involved in the decay, no information about the absorbed photon energy is passed on to the emitted electron. The emitted electron therefore has constant kinetic energy independent of the incident photon energy, as with normal Auger decay. The only way that spectator decay and normal Auger decay can be distinguished is that the kinetic energy of the emitted electrons is slightly modified in the presence of a spectator electron. The spectator electron screens the core hole, so that the emitted electron

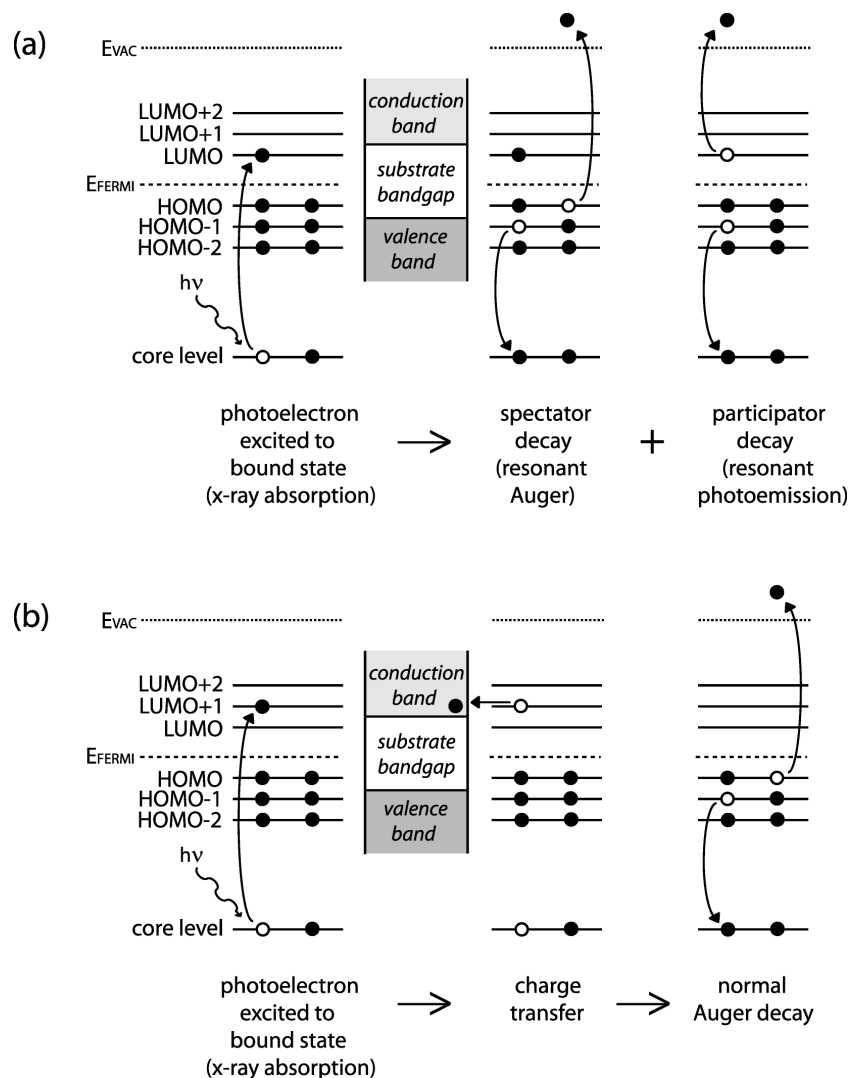


FIGURE 4.3: Electron excitation and de-excitation processes in resonant electron spectroscopy. Part (a) shows an electron being photoexcited to an unoccupied level within the molecule which overlaps with the substrate band gap, followed by the decay processes of spectator decay and participator decay. Part (b) shows an electron being photoexcited to an unoccupied level which overlaps with the substrate conduction band, followed by charge transfer and then normal Auger decay.

leaves with slightly higher kinetic energy than in normal Auger. This energy difference is termed the *spectator shift* and is usually too small to allow the two processes to be accurately resolved.[47]

The second type of decay event illustrated in Figure 4.3 (a) is called *participator decay*, because the photoexcited electron participates in the decay itself. As a result the emitted electron carries information about the unoccupied level that the excited electron was in, and hence about the illuminating photon energy. The emitted electron has constant binding energy, as with photoemission. In fact, the final state of participator decay is identical to that of photoemission. Here, the system is left with a hole in the HOMO-1 level, and is identical to how the system would look if a photoelectron had been directly emitted from that level. The final state is the same in both cases so the emitted electron appears to have the same binding energy. Since the decay occurs at the same binding energy as direct photoemission, but only happens on-resonance, the process is also called *resonant photoemission*.

Figure 4.3 (b) shows the case where a core electron is photoexcited to a bound state that overlaps with the substrate *conduction band*. This is where things get interesting. It is now possible for this electron to tunnel into the substrate conduction band. Note that it is not a certainty; the energy levels overlap energetically, but they may not overlap spatially, and from our information we don't know what is allowed or forbidden in terms of quantum selection rules. *Even if* all of these conditions are favourable, there is still a chance that the electron will take part in participator decay and leave the unoccupied level by those means. The amount of charge transfer events as opposed to participator decay events depends on the strength of the coupling between the molecule and substrate energy levels involved. The stronger the coupling, the higher the probability of charge transfer occurring before a decay event. If charge transfer does occur as shown in the figure, the system then relaxes via normal Auger decay.

If no charge transfer occurs, the processes in 4.3 (a) take place, and if charge transfer does occur, the processes in 4.3 (b) take place. If only some of the electrons tunnel away then a corresponding proportional mixture of decay events will result. To establish which decay events are taking place, one must measure the energy of the

emitted electrons. Since spectator decay as seen in (a) and normal Auger decay as seen in (b) cannot usually be resolved, they cannot be used to identify whether charge transfer is occurring. That leaves the participator decay in (a), versus charge transfer as in (b). The presence of a participator decay signal thus indicates that no charge transfer is occurring, and its absence indicates that charge transfer *is* occurring.

Figure 4.3 reiterates the importance of constructing an energy level alignment diagram as discussed in the previous section. The alignment diagram can tell us for which molecular levels charge transfer is possible.

4.3.2 Data acquisition and identification of features

Resonant electron spectra are acquired in the same way as normal electron spectra – by analysing the kinetic energy of emitted electrons using an electron analyser. The difference in applying the two techniques is in the chosen energy of the incident photons. For a *resonant* electron spectrum, a photon energy is chosen that resonantly excites electrons from a core level into an unoccupied molecular level.

To give a full overview of what is going on, one can record many spectra covering a range of photon energies and then display these together. This allows one to see the various resonances that occur at different photon energies. Such a data set is shown in Figure 4.4. Below ~ 399 eV photon energy there are no decay events because the photon energy isn't high enough to excite electrons from the chosen core level to any unoccupied levels. For this region the spectrum is said to be *pre-edge*. Then at ~ 399 eV, features rise out of the background due to many decay events happening, meaning that the spectrum is on-resonance. Since this is the lowest unoccupied level to be accessed, it is identified as the LUMO, with subsequent resonances being denoted the LUMO+1, LUMO+2 etc.

The different features can be identified with decay processes by the characteristics of their position and shape. Figure 4.5 shows a schematic top-down view of a resonant electron spectroscopy data set, for clarity of explanation, with lighter areas indicating protruding peaks. Features that are constant in binding energy and observed at all photon energies are due to direct photoemission. Features that are only observed

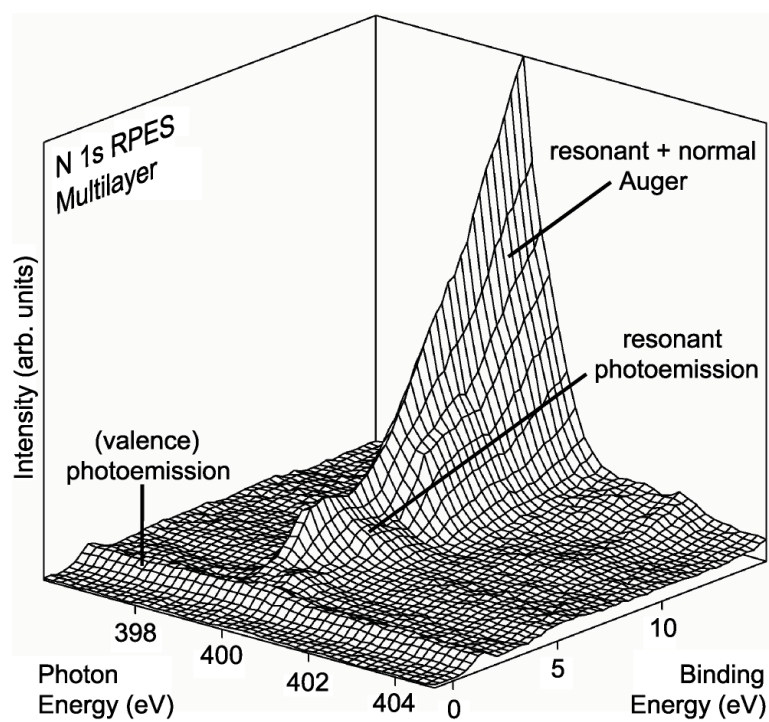


FIGURE 4.4: N 1s resonant electron spectroscopy data for a multilayer of N₃. Valence band spectra with a binding energy range of 4-20 eV were acquired over the photon energy range $h\nu = 397$ -405 eV.

on-resonance are due to either participator decay, spectator decay or normal Auger decay. As already discussed, spectator decay and normal Auger decay are not usually resolvable, differing only by a small spectator shift in their kinetic energy. This leaves the resonant peaks to be classified either as Auger-type peaks or participator peaks.

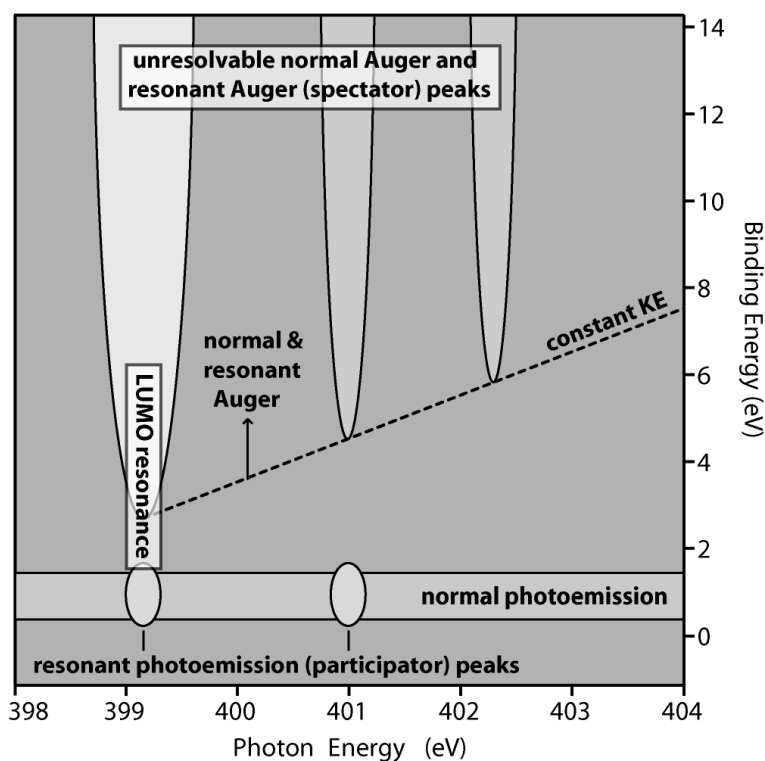


FIGURE 4.5: Schematic figure identifying the processes behind the different peaks seen in a resonant electron spectrum.

The participator peaks extend to lower binding energy than Auger-type peaks because both an unoccupied level and a valence level are involved in the decay, whereas in Auger decay both electrons involved are from valence levels. The unoccupied levels sit closer to the vacuum level than the valence levels and so have a lower binding energy. The binding energy of features thus gives us one way to distinguish the type of decay event by which they are caused.

Since normal Auger and spectator Auger decay do not involve the photoexcited electron, they are independent of the incident radiation and constant in kinetic energy. An exception to this behaviour occurs for the Auger resonant Raman (ARR)

regime,[47, 48] where in the event of intact coherence, i.e. with the electron localised, and for excitation to a particular electronic state, the resonant Auger disperses with constant BE. ARR requires that the photon energy bandwidth is narrower than the natural line width of the electronic energy levels, which is rarely the case. Additionally, the identification of different channels is often impractical due to the complexity of overlapping structures in a spectrum. The example plots shown are not in the ARR regime, so the Auger features drift diagonally along constant kinetic energy lines ($h\nu = E_B + E_K(\text{constant})$). The minimum separation between the Auger peaks and the participator peaks occurs at the LUMO where the participator energy levels are as close as possible to the Auger energy levels. This minimum separation is equal to the energy of the HOMO-LUMO gap. The Auger peak at the LUMO is usually very obvious, and one can define its low binding energy limit. If a line of constant kinetic energy is then drawn onto the plot, passing through this limit, all of the Auger features are to higher binding energy of this line, and any features to lower binding energy of this line that only occur on-resonance are due to participator decay.

4.3.3 Core-hole clock quantification method

While resonant electron spectroscopy enables one to observe the delocalisation of charge from unoccupied molecular valence levels, the core-hole clock implementation of it allows quantification of an upper time limit in which this occurs.

As discussed in Section 4.3.1, the presence of a participator decay signal indicates that *no* charge transfer is occurring, and its absence indicates that charge transfer *is* occurring, on a time scale competing with core-hole decay. But when presented with a resonant electron spectrum, how does one know whether a participator peak is absent or not? To observe the absence of peaks, one must make a comparison to a case where all the participator peaks are present because no charge transfer is occurring from any level. For this, a multilayer of dye molecules is prepared, because in its solid form the dye is non-conducting. By comparing a multilayer no-charge-transfer spectrum with a monolayer possible-charge-transfer spectrum, one can assess qualitatively whether participator peaks are absent in the latter case. By curve-fitting

the peaks and measuring their intensities, one can make a quantitative analysis of the amount of charge transfer occurring, and by taking into account the lifetime for core-hole decay, one can quantify an upper time limit in which charge transfer occurs. This approach to quantifying the timescale for charge transfer is called the core-hole clock method. The time for which the core hole exists – the core-hole lifetime – is like a clock counting down, and charge transfer either has to take place before the clock has counted down, or not at all.

In order to quantitatively analyse this situation, a model must first be developed based on some assumptions. The first assumption is that the charge transfer step and the core-hole decay step are independent of each other. Charge transfer either happens or it doesn't, and in either case is followed by core-hole decay. The second assumption is that the tunnelling probability for the charge transfer step is exponential as a function of time.[47, 49] The third assumption is that the probability of core-hole decay is exponential as a function of time.[47, 50, 51, 52] The number of molecular systems left in the excited state at time t ,

$$N(t) = N(0) \exp(-t/\tau), \quad (4.6)$$

where $N(0)$ is the number of systems in the decaying state at some arbitrary time 0, and τ is the characteristic timescale for the event of interest. The probability of core-hole decay *occurring* before time T is:

$$P_{\text{chd}}(T) = \int_0^T \frac{1}{\tau_{\text{chd}}} \exp(-t/\tau_{\text{chd}}) dt, \quad (4.7)$$

where τ_{chd} is the average time for core-hole decay. The probability of charge transfer *not occurring* before time T is:

$$P_{\text{no CT}}(T) = 1 - \int_0^T \frac{1}{\tau_{\text{CT}}} \exp(-t/\tau_{\text{CT}}) dt \quad (4.8)$$

where τ_{CT} is the average time for charge transfer. Since the two events are being considered as independent, to find out the probability that charge transfer occurs as well as core-hole decay, the probabilities must be combined:

$$P_{\text{chd \& no CT}}(T) = \int_0^T P_{\text{chd}}(t) P_{\text{no CT}}(t) dt. \quad (4.9)$$

Substituting Equations 4.7 and 4.8 into 4.9 gives:

$$P_{\text{chd \& no CT}}(T) = \int_0^T \frac{1}{\tau_{\text{chd}}} \exp(-t/\tau_{\text{chd}}) \left[1 - \int_0^t \frac{1}{\tau_{\text{CT}}} \exp(-t'/\tau_{\text{CT}}) dt' \right] dt \quad (4.10)$$

$$P_{\text{chd \& no CT}}(T) = \frac{\tau_{\text{CT}}}{\tau_{\text{chd}} + \tau_{\text{CT}}} \left[1 - e^{-(T/\tau_{\text{chd}} + T/\tau_{\text{CT}})} \right] \quad (4.11)$$

Spectra are measured in the limit $T \rightarrow \infty$, when the core-hole excited state has decayed. In this limit the above equation then becomes:

$$P_{\text{chd \& no CT}}(\infty) = \frac{\tau_{\text{CT}}}{\tau_{\text{chd}} + \tau_{\text{CT}}} \quad (4.12)$$

The probability of core-hole decay and no charge transfer can also be written as the branching ratio for the events that characterise this outcome. If no charge transfer occurs, the decay channel will be a resonant one (spectator or participator) and the recorded intensity of this channel is denoted I_{resonant} . When this is normalised by the summed intensity of the resonant and non-resonant decay channels, it is a fraction that mirrors the probability for no charge transfer:

$$P_{\text{chd \& no CT}}(\infty) = \frac{I_{\text{resonant}}}{I_{\text{resonant}} + I_{\text{normal Auger}}} \quad (4.13)$$

Equating equations 4.12 and 4.13 gives:

$$\frac{\tau_{\text{CT}}}{\tau_{\text{chd}} + \tau_{\text{CT}}} = \frac{I_{\text{resonant}}}{I_{\text{resonant}} + I_{\text{normal Auger}}} \quad (4.14)$$

As discussed in Section 4.3.2, it is often the case that normal Auger and spectator Auger peaks cannot be resolved. In this case one is left with the participator peaks to find out about charge transfer. In a monolayer where the molecules are coupled

to the surface, charge transfer can occur, but in a multilayer where the molecules are isolated, charge transfer cannot occur. As above, the spectral intensities can be used to mirror the branching ratio of events. If charge transfer occurs, this is reflected by the decrease in the participator intensity, $(I_{\text{isolated}}^{\text{participator}} - I_{\text{coupled}}^{\text{participator}})$. When this is normalised by the intensity for the isolated case in which no charge transfer occurs, it is a fraction that mirrors the probability for charge transfer:

$$P_{\text{chd \& CT}}(\infty) = \frac{I_{\text{isolated}}^{\text{participator}} - I_{\text{coupled}}^{\text{participator}}}{I_{\text{isolated}}^{\text{participator}}} \quad (4.15)$$

In the limit $T \rightarrow \infty$, either charge transfer has or has not occurred, and so the probabilities for each event add up to 1:

$$P_{\text{chd \& CT}}(\infty) = 1 - P_{\text{chd \& no CT}}(\infty) \quad (4.16)$$

Substituting in Equation 4.12 gives:

$$P_{\text{chd \& CT}}(\infty) = 1 - \frac{\tau_{\text{CT}}}{\tau_{\text{chd}} + \tau_{\text{CT}}} \quad (4.17)$$

$$P_{\text{chd \& CT}}(\infty) = \frac{\tau_{\text{chd}}}{\tau_{\text{chd}} + \tau_{\text{CT}}} \quad (4.18)$$

Equating Equations 4.18 and 4.15 gives:

$$\frac{\tau_{\text{chd}}}{\tau_{\text{chd}} + \tau_{\text{CT}}} = \frac{I_{\text{isolated}}^{\text{participator}} - I_{\text{coupled}}^{\text{participator}}}{I_{\text{isolated}}^{\text{participator}}} \quad (4.19)$$

which simplifies to an expression for the characteristic timescale for charge transfer,

$$\tau_{\text{CT}} = \tau_{\text{chd}} \frac{I_{\text{coupled}}^{\text{participator}}}{I_{\text{isolated}}^{\text{participator}} - I_{\text{coupled}}^{\text{participator}}} \quad (4.20)$$

The variables $I_{\text{coupled}}^{\text{participator}}$ and $I_{\text{isolated}}^{\text{participator}}$ can be found experimentally as the intensities of the participator peak in the dye monolayer and multilayer respectively. These

values are then normalised by the total cross-sections as provided by the NEXAFS intensities $I_{\text{NEXAFS}}^{\text{coupled}}$ and $I_{\text{NEXAFS}}^{\text{isolated}}$:

$$\tau_{\text{CT}} = \tau_{\text{chd}} \frac{\frac{I_{\text{coupled}}^{\text{participator}}}{I_{\text{coupled}}^{\text{NEXAFS}}}}{\frac{I_{\text{isolated}}^{\text{participator}}}{I_{\text{isolated}}^{\text{NEXAFS}}} - \frac{I_{\text{coupled}}^{\text{participator}}}{I_{\text{coupled}}^{\text{NEXAFS}}}} \quad (4.21)$$

4.4 Core-level resonant x-ray emission spectroscopy

Resonant x-ray emission spectroscopy is to x-ray emission spectroscopy as resonant electron spectroscopy is to photoemission spectroscopy. It involves measuring the energy of photons emitted following resonant excitation of electrons from a core level to an unoccupied level. Since, again, the electrons are being put into unoccupied levels, this gives them the opportunity to transfer from the molecule to the substrate conduction band if the energy level alignment allows this. The emitted photons reveal which decay events occurred, allowing one to distinguish whether or not the excited electron transferred into the substrate before the decay event took place.

In this section, first the different processes which lead to photon emission following resonant excitation are described. Then the acquisition of data is discussed, and how it can be qualitatively analysed to give information about charge transfer.

4.4.1 Resonant x-ray emission processes

The various events that lead to a photon being ejected following x-ray absorption are shown in Figure 4.6. Part (a) shows the case where a core electron is photoexcited to a bound state that overlaps with the substrate band gap. The electron cannot transfer from the molecule to the substrate because there are no states for it to move to. The excited state then decays via one of two processes. Either the excited electron drops back down to fill the core hole, or an electron from the valence band fills the core hole. This is analogous to participator and spectator decay in resonant electron spectroscopy. If, as in case (a), no charge transfer can occur due to the excited electron overlapping energetically with the substrate band gap, then both of these

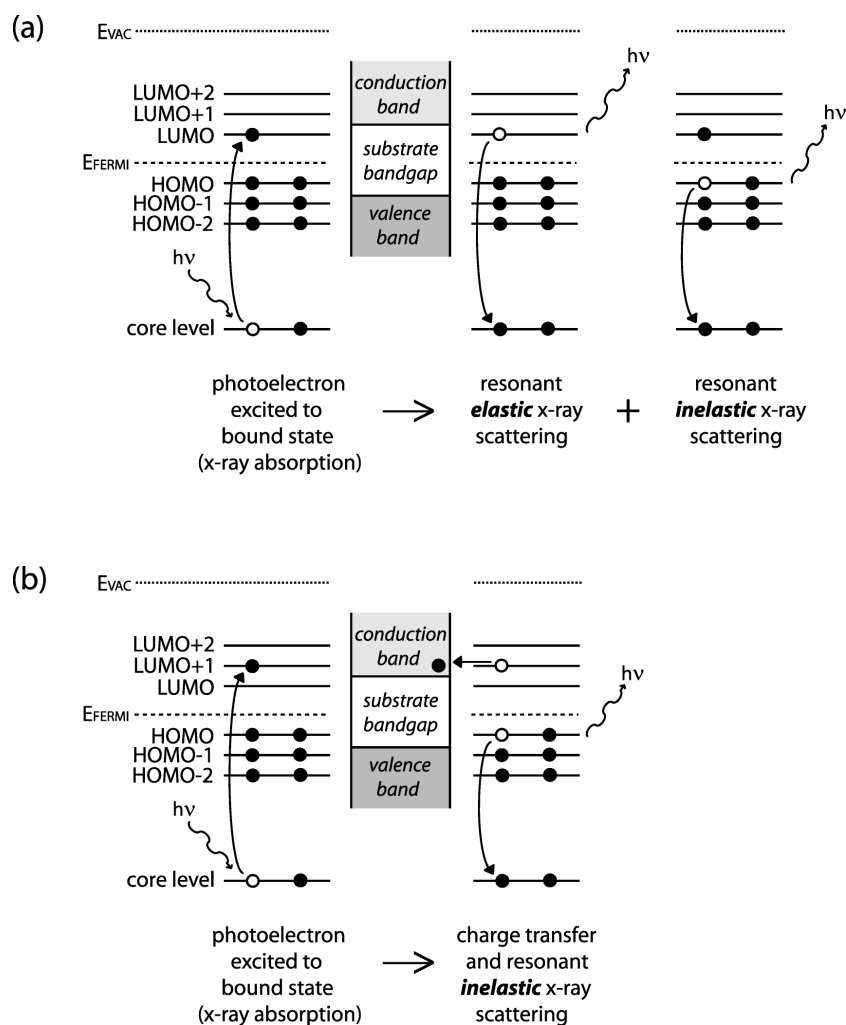


FIGURE 4.6: Electron excitation and de-excitation processes in resonant x-ray emission spectroscopy. Part (a) shows an electron being photoexcited to an unoccupied level which overlaps with the substrate band gap, followed by the decay processes of resonant elastic x-ray scattering and resonant inelastic x-ray scattering. Part (b) shows an electron being photoexcited to an unoccupied level which overlaps with the substrate conduction band, followed by charge transfer and resonant inelastic x-ray scattering only.

processes occur. In case (b) however, the molecular level that the electron is excited to overlaps with the substrate conduction band. The electron can transfer to the substrate, and if this happens then only one type of decay event can occur – where the core hole is filled by an electron from the valence band.

When the originally excited electron fills the core hole, this is the reverse process of the x-ray absorption step, and the emitted photon has the same energy as the absorbed photon. This is called *elastic* x-ray scattering, because the x-ray is scattered without losing any energy. The feature this process produces is called the *elastic peak*. Elastic scattering can only occur on-resonance, and does not occur for normal off-resonance x-ray emission spectroscopy. There may however be some photons measured at the position of the elastic peak that are due to reflection as opposed to absorption and re-emission. When an electron from the valence band fills the core hole rather than the originally excited electron filling the core hole, this is *inelastic* x-ray scattering because the emitted photon has less energy than the absorbed photon.

The different cases (a) and (b) can be distinguished depending on whether elastic scattering occurs. If an elastic peak is not present when measuring an on-resonance x-ray emission spectrum, this implies that the excited electron is leaving the unoccupied molecular level within the core-hole lifetime.

4.4.2 Data acquisition and analysis

Photons are analysed using an x-ray emission spectrometer which measures photons as a function of their energy. The spectrometer is a monochromator, similar in function to the one in the beamline. Since for elements of low atomic number, Auger decay is by far the dominant decay process over x-ray emission, it takes a long time to acquire enough photons to obtain a good signal-to-noise ratio. In resonant electron spectroscopy, spectra are recorded at increments in photon energy but for resonant x-ray emission the timescale for this would be unfeasible, so spectra are taken at single photon energies only. Even at a single photon energy, it can take several hours to obtain a clear spectrum.

Since single photon energies only are being used, first a NEXAFS spectrum is recorded to see the electronic structure of the unoccupied levels. An unoccupied level is then chosen to be studied, and the photon energy needed for this resonance is read off the scale on the NEXAFS spectrum. The sample is then illuminated with photons of this energy, and the emitted photons are analysed.

Examples of resonant x-ray emission spectra are shown in Figure 4.7. Two spectra are overlaid, taken using photon energies to excite the LUMO and the LUMO+1 resonances for a monolayer of N3 on TiO₂. As with x-ray emission spectroscopy, the spectrum is on a photon energy scale, but its shape represents the valence band of the system being measured. As with the normal version of x-ray emission spectroscopy, resonant x-ray emission spectroscopy is core-hole specific, in that excitation can only occur if the atom with the participating core level is local to the unoccupied level of the resonance. In this figure, electrons are excited from N atoms, but the spectra have different shapes due to the LUMO and the LUMO+1 being at different locations on the molecule, and hence being local to different occupied molecular orbitals.

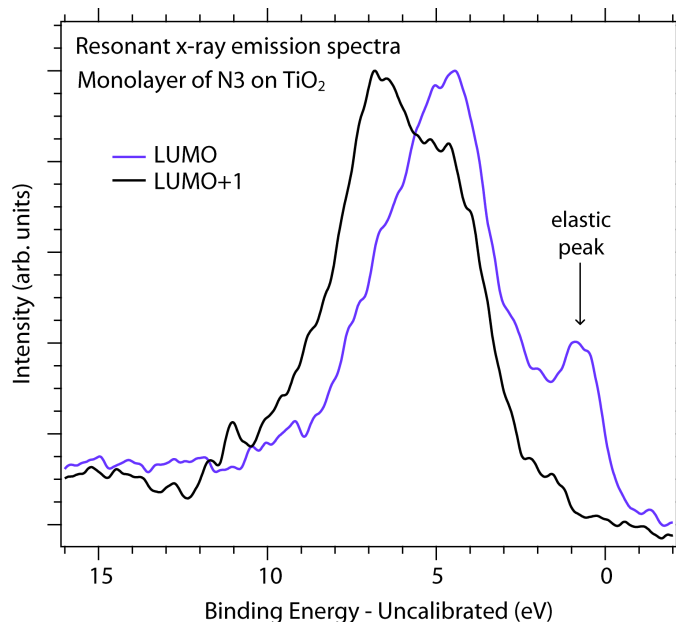


FIGURE 4.7: Resonant x-ray emission spectra for a monolayer of N3 on TiO₂. The spectra are taken using photon energies of 398.85 and 400.15 eV, to excite electrons from the N 1s core level to the LUMO and LUMO+1.

An important additional feature seen in *resonant* x-ray emission spectroscopy is the elastic peak. Recall from the energy level diagrams in Figure 4.6 that the presence of an elastic peak indicates no charge transfer, and the absence of an elastic peak indicates charge transfer. Here, the spectra show qualitatively that there is charge transfer to the substrate from the LUMO+1 but not from the LUMO.

To confirm that some other process is not causing the absence of an elastic peak, the monolayer spectra can be compared to multilayer spectra taken at the same energies, for which charge transfer should not occur due to the dye being non-conducting in its solid form. A multilayer spectrum is shown in Figure 4.8. Here, there are elastic peaks for both resonances because no charge transfer is occurring. That the elastic peak is smaller for the LUMO+1 than the LUMO here, is thought to be because the LUMO has a larger density of states than the LUMO+1. With more available states, the LUMO will be involved in more x-ray absorption events, resulting in increased emission events including the elastically scattered x-rays that cause the elastic peak.

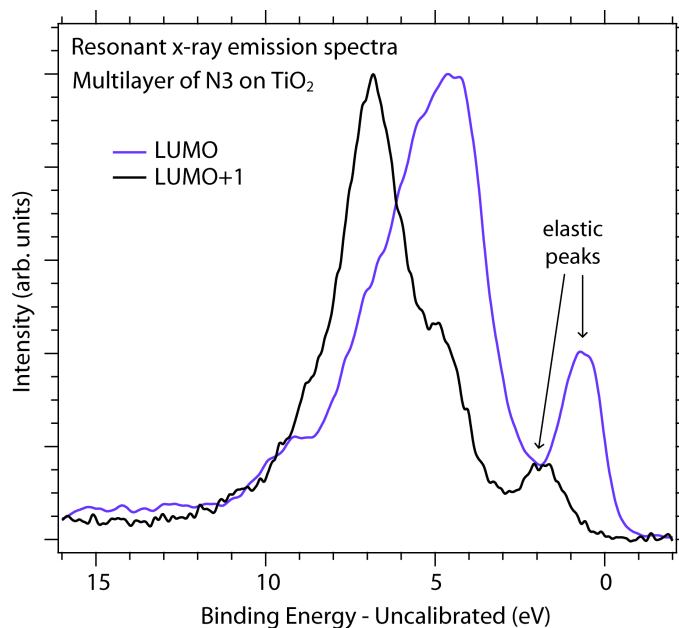


FIGURE 4.8: Resonant x-ray emission spectra for a multilayer of N3 on TiO₂. The spectra are taken using photon energies of 398.85 and 400.15 eV, to excite electrons from the N 1s core level to the LUMO and LUMO+1.

CHAPTER 5

Ultra-high vacuum electrospray deposition

In this chapter, the reader is introduced to the technique used in this work to deposit molecules onto surfaces. The technique is called ultra-high vacuum electrospray deposition (UHV-ESD). First, a brief background to the original, non-UHV electrospray deposition method is presented. Secondly, the motivation for developing a UHV version of electrospray deposition at Nottingham's Nanoscience Group is discussed. Thirdly, the details of the UHV-adapted electrospray apparatus used in this work are given, along with the physical principles by which the machine functions. Finally, the chapter is summarised.

5.1 Background

Electrospray ionisation was pioneered by Fenn and his co-workers in the 1980s,[53, 54] for which Fenn won a share of the Nobel Prize in Chemistry in 2002.[55] The technique was developed as a means of getting molecules into the gas phase so that they could be analysed with mass spectrometry. The process involves dissolving or suspending molecules in a liquid which is then passed through a small, electrically charged capillary. At the exit of the capillary the liquid forms an electrospray jet comprising single and multiple ionised molecules. The full details of how this occurs are described below. This gentle, liquid-based method enables thermally labile or non-volatile molecules, such as large biomolecules, to be introduced into the gas phase.[56] The technique is widely used in mass spectrometry and has also been successfully

developed for the ambient *deposition* of materials, with uses ranging from batteries to biological thin films.[57]

The first electrospray ionisation systems had pressures ranging from ambient to medium vacuum, and this precluded them for use in those surface science experiments that require a high vacuum. In recent years, the standard electrospray set-up has been developed at Nottingham and elsewhere as a deposition method used to deposit molecules at increasingly low pressures. Our most recent version successfully allows deposition of molecules onto surfaces at UHV pressures.

5.2 Motivation

In UHV surface science experiments, the most popular method of depositing molecular solids or metals onto surfaces is to use a Knudsen cell (K-cell).[58, 59] In this technique, the substance to be deposited is put into a clean crucible which is then secured within the K-cell's UHV housing. Once under vacuum, the crucible is heated by passing current through a wire coiled around the crucible. The substance being heated eventually reaches its sublimation temperature, at which point the molecules or atoms sublime (change state from the solid phase directly to the gas phase), travel through the vacuum in straight lines if unperturbed, and those with the correct trajectory are incident upon the sample surface.

The main benefit of this sublimation technique is that the deposition can be performed under UHV, and thus the sample remains UHV-clean. It also gives the user good control over the rate of deposition, so that the adsorbate can be built up gradually and methodically. Sublimation does however have limitations. If one wants to study what is put into the crucible, a requirement is that by the time that substance gets to the surface its chemical structure has not changed; this is not the case for many molecules. For example, the C_{60} molecule – a spherical cage of carbon atoms – can be successfully deposited using a K-cell, but if $N@C_{60}$ is deposited in this way, by the time it reaches the surface the nitrogen atom that was originally within the carbon cage will have ‘fallen out’. This problem arises when molecules decompose at a temperature lower than that at which they sublime. Subliming these

molecules causes fragments of the molecule to be deposited onto the surface rather than the intact molecules originally put into the K-cell's crucible. This is not usually the desired outcome.

One such molecule that is thermally labile, i.e. decomposes upon heating, is the dye molecule N3. As described in Chapter 1, N3 is currently the most efficient dye molecule that has been found for use in dye-sensitised solar cells. It is therefore the subject of much research. In particular, it is of great interest how the molecule bonds to and interacts with titanium dioxide, a metal oxide to which it is often bonded in the cell, as this is the key interface at which solar energy is transferred into electrical energy. Until now, the study of N3 on surfaces has been limited to *ex situ* preparations, i.e. non-UHV deposition methods. Ideally in surface science the surface and adsorbate should be clean, which simplifies the system so that only the clean surface and adsorbate of interest are studied, without the presence of atmospheric contaminants. The goal of depositing N3 *in situ* has been a large motivation in successfully developing UHV-ESD at Nottingham. The technique also opens up a huge range of potential experiments involving thermally labile molecules, which in the past have not been possible. The Nottingham Nanoscience Group has now successfully used the technique to deposit carbon nanotubes,[60] C₆₀,[61, 62] porphyrins,[63] single-molecule magnets[64] and in the current work, the dye molecule N3.[65, 66]

In the following section the electrospray deposition process is explained in the context of the apparatus designed and engineered at Nottingham.

5.3 Apparatus and physical processes

The molecule of interest must first be dissolved or suspended in a suitable solvent. In this work the solvent used to dissolve N3 was a 25% water, 75% methanol mixture. Another solvent mixture that works well with many molecules is toluene and methanol, which can be used to dissolve C₆₀, N@C₆₀, Zn-protoporphyrin and single-molecule magnets. The solution or suspension is then placed in a sealed reservoir from which the liquid can only escape via a 2 μm frit filter (Valco). This prevents undissolved clusters or particulates from clogging the subsequent length of narrow

PEEK (polyetheretherketone) tubing, which has an inner diameter of $860\ \mu\text{m}$. The liquid is caused to flow through the tubing by application of a positive pressure to the reservoir. In the first instrument configuration we developed, as used in Chapter 6, this was done by applying 0.5 bar N_2 to the reservoir, and in our second instrument configuration as used in Chapter 7, a syringe was used as the reservoir, and a pressure maintained by applying a small push to the plunger. Upon leaving the PEEK tubing the liquid then enters a stainless steel tube with inner diameter $250\ \mu\text{m}$, before entering an even narrower hollow stainless steel needle with inner diameter $100\ \mu\text{m}$ (New Objective, USA). This hollow stainless steel needle shall be referred to as the *emitter*. The small diameters of the tubes through which the liquid travels help to produce a very low liquid flow rate of $\sim 10\ \mu\text{l}\ \text{min}^{-1}$. The steel tube and the emitter are secured within insulated housing, and the position of this housing is controlled by a small manipulator which allows movement in x, y and z.

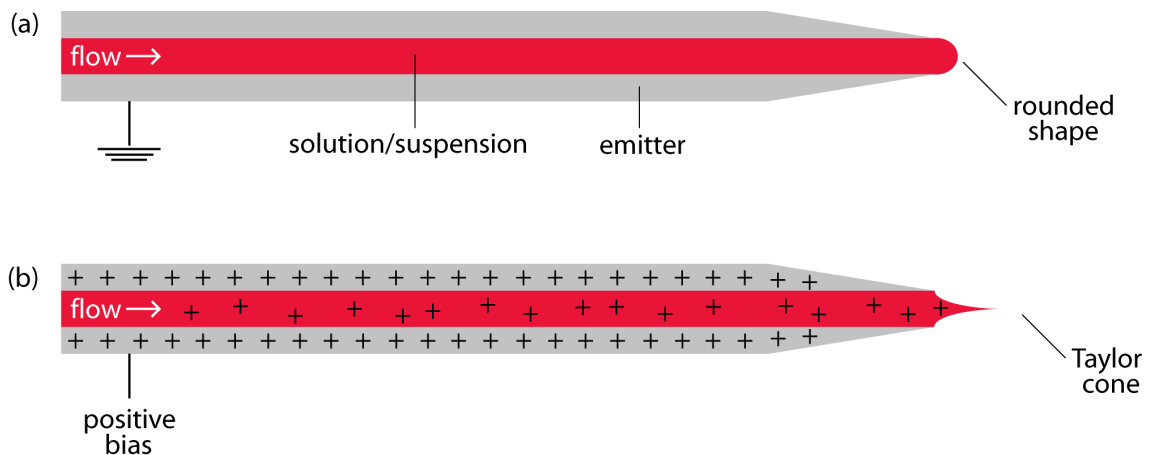


FIGURE 5.1: Schematic images showing the effect that a positive bias on the electrospay emitter has on the behaviour of the solution/suspension. In (a) the emitter is grounded and the liquid forms a rounded shape at the emitter exit due to surface tension. In (b), a large positive bias is applied to the emitter, causing the liquid at the emitter exit to change shape to a Taylor cone; here the Coulomb repulsion forces of the ionised liquid compete with its surface tension.

With the system as described thus far, the liquid then collects in a rounded droplet at the end of the emitter, as shown in Figure 5.1 (a). When the droplet's weight over-

comes the surface tension of the liquid, it falls to the floor. To initiate the electrospray process, the key step is to apply a large, positive bias to the electrically connected stainless steel tube and emitter. At the interface between the solution/suspension and the steel tubing and emitter, electrons are stripped away from solvent molecules, producing ions. These ions repel each other and also the steel tubing and emitter. In order to minimise this Coulomb repulsion, the liquid at the exit of the emitter forms a tapered shape known as a Taylor cone,[67] as shown in Figure 5.1 (b). As the emitter's electric potential is increased from zero, the liquid at the end of the emitter goes from being rounded to being this Taylor cone shape, and at a threshold voltage the Coulomb repulsion forces overcome the surface tension of the Taylor cone, and a jet of small droplets is emitted, propelled from the emitter by its electric field.

The next stage in the electrospray process is shown in Figure 5.2. While travelling through the air, neutral solvent molecules and solvent ions evaporate from the positively charged droplets, causing the volumes of the droplets to decrease and thus increasing the charge density within them. At a threshold droplet diameter and charge, defined by the Rayleigh Limit, the droplets split in what is known as *Coulomb explosion*. The Rayleigh Limit is defined in Equation 5.1:

$$q^2 = 8\pi^2\epsilon_0\gamma D^3, \quad (5.1)$$

where q is the total charge within the droplet, ϵ_0 is the permittivity of air, γ is the surface tension of the liquid and D is the droplet diameter. These smaller droplets lose solvent molecules and once again split apart. After travelling a short distance through the air, repeatedly splitting along the way, the jet becomes a plume of very small droplets. Figure 5.3 (b) shows a photograph of such a plume. The positive bias is adjusted to obtain the best possible plume; over a small range of voltages the plume changes in shape and size, and in one regime the jet even splits into two. Characteristics desired in a plume are that it is a very fine mist, spread out as much as possible at the entrance aperture/capillary, a large lateral size of the plume indicating that a lot of Coulomb explosion is occurring and thus the droplets are small, or are even single molecules. With our apparatus, a positive bias of ~ 2.3 kV was applied.

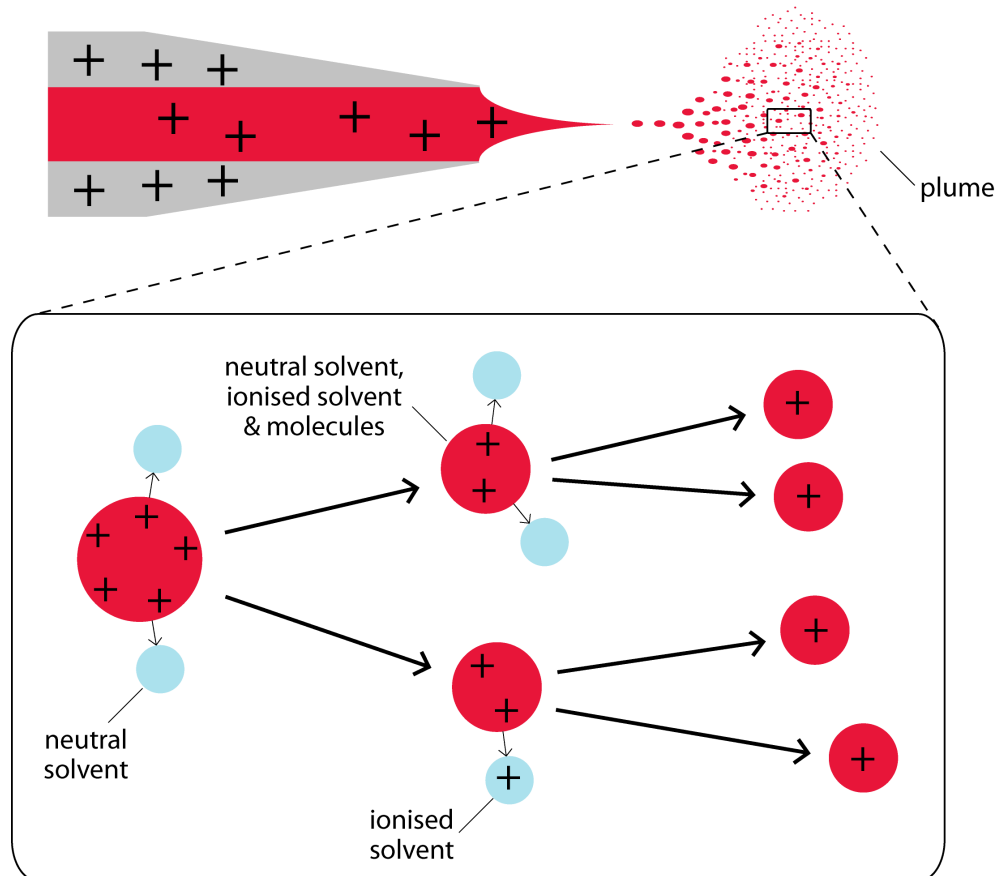


FIGURE 5.2: Schematic diagram showing the processes which create an electrospay plume once a jet of droplets has left the emitter. Multiply-charged droplets comprising neutral solvent molecules, ionised solvent molecules and the molecules being deposited, travel through air where they are bombarded by air molecules. Both neutral and charged solvent molecules evaporate from the droplets, decreasing the droplet volume, and thus increasing the charge density in the droplet. At the Rayleigh Limit, the droplet's surface tension can no longer contain its self-Coulomb repulsion, and the droplet splits. This process happens repeatedly until the droplets are very small, or are single molecules.

The plume is best viewed, as in Figure 5.3, while shining a laboratory light source upon it.

At this point in the molecules' journey they are within small droplets in air, being propelled away from the emitter. Some may even be travelling solvent-free by this point. What remains is for the droplets and molecules to travel from air to vacuum. This is done using a series of differentially pumped chambers, linked by small apertures which are grounded and increase in diameter from 0.5 mm to 1.0 mm toward the sample preparation chamber to which the UHV-ESD system is attached. The apertures are aligned centrally in-line with the emitter so that droplets and molecules travelling with a central trajectory can pass through the series of chambers and into the preparation chamber, where they are incident upon the sample. The small diameter of the apertures, along with the pumping on each chamber, allows the pressure to be reduced from atmospheric at the emitter to UHV in the preparation chamber. The deposition spot size on the sample is approximately 3-4 mm in diameter at a distance of 20 cm from the final aperture. The ions are estimated to be travelling at the speed of sound, so for N₃ this equates to the ions having a kinetic energy upon reaching the surface of 0.32 eV per molecule. The sample mounted within the preparation chamber is optically aligned by shining a laboratory light source through the final two apertures of the system.

In the first version of our electrospray apparatus, as used in Chapter 6, the entrance to the pumped chambers was a conical aperture of diameter 0.5 mm as shown in Figure 5.3 (a). Similar apertures are used to join the separately pumped chambers. In the second version of the electrospray apparatus, the entrance was adapted by changing the conical aperture for a stainless steel tube, or *entrance capillary*, as shown in Figure 5.3 (b). The entrance capillary has an inner diameter of 0.25 mm, an outer diameter of 1.6 mm and is 5 cm long. The apparatus was adapted in order to lower the pressure in the final chamber while maintaining the flux of molecules and droplets travelling through the system.

The spray travels through chambers 1, 2 and 3 as shown in Figure 5.4. Chambers 1 and 2 are pumped by scroll pumps, and chamber 3 by a 70 ls⁻¹ turbomolecular pump (Varian). The pressures in chambers 1, 2 and 3 are thought to be approximately 1,

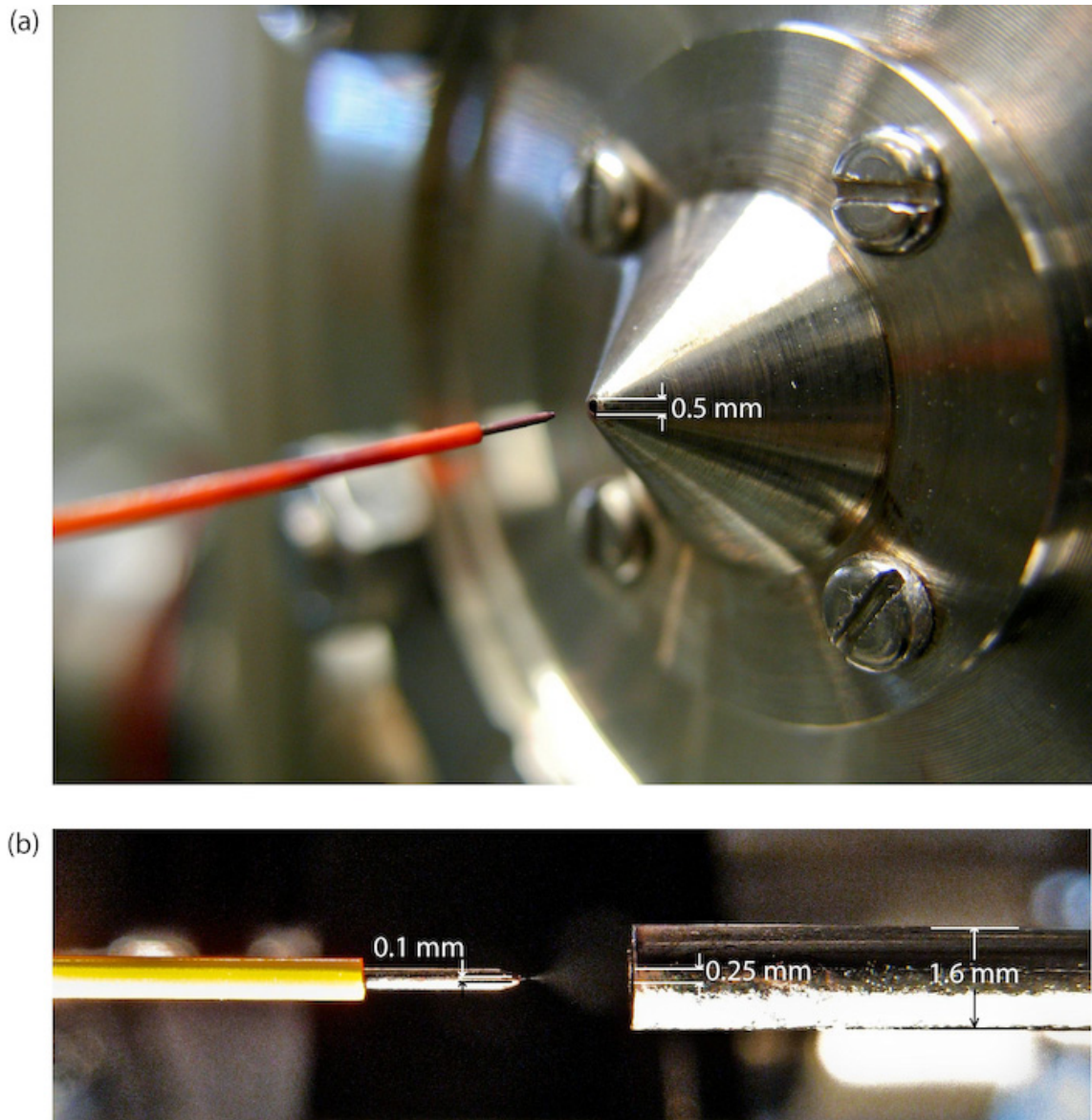


FIGURE 5.3: Photographs showing different versions of entrances to the first differentially pumped chamber. Photograph (a) shows the conical entrance aperture (diameter 0.5 mm) used in the first equipment configuration, and photograph (b) shows the entrance capillary (inner diameter 0.25 mm, length 5 cm) used in the second configuration.

10^{-2} and 10^{-5} mbar, respectively. Between chamber 3 and the preparation chamber, a UHV gate valve is used to seal off the preparation chamber entirely from air when the electro spray apparatus is not in use.

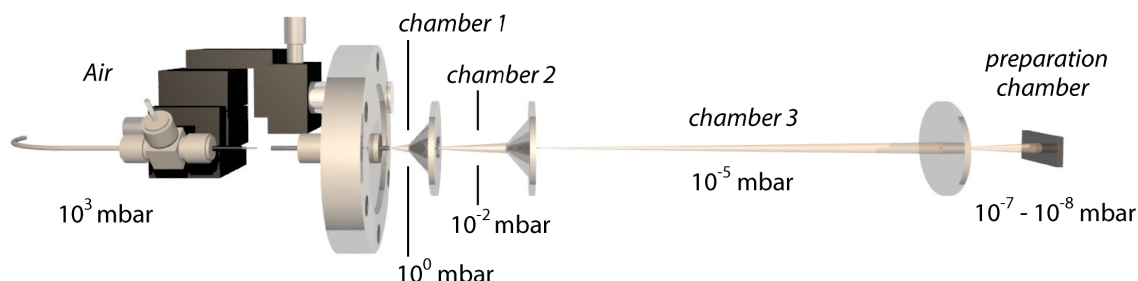


FIGURE 5.4: Schematic illustration of the electro spray system showing the molecular beam travelling from left to right as it leaves the high voltage emitter, passes via conical apertures through differentially pumped chambers, and is incident upon the sample.

The base pressures of the preparation chambers used at Nottingham and at I511-1 were approximately 5×10^{-11} mbar. With the gate valve open but the emitter voltage turned off, and thus no electro spray occurring, the pressure in the preparation chamber was 4×10^{-8} mbar with the first apparatus configuration, and 2×10^{-8} for the second. With the voltage turned on, the pressure in the preparation chamber rose to 2×10^{-7} and 5×10^{-7} for the first and second configurations, respectively. The pressure rise in the preparation chamber is due to residual solvent molecules in the molecular beam; this was revealed by performing residual gas analysis in Nottingham. Comparing the pressures recorded for both equipment configurations suggests that using the entrance capillary rather than the conical entrance aperture improves the deposition by letting in less air but more electro sprayed molecules. The increased electro spray partial-pressure is perhaps also due to improved positioning and voltage-tuning of the spray plume.

The design of an electro spray system integrating differentially pumped chambers thus makes the electro spray technique compatible for use with ultra-high vacuum systems, when studying samples with relatively inert surfaces, such as TiO_2 or Au, that can be transferred to the mid 10^{-8} mbar range without undergoing excessive contamination or reconstruction. The UHV-ESD system can therefore be used to deposit

thermally labile and non-volatile molecules to be analysed using UHV techniques such as scanning tunnelling microscopy and photoelectron spectroscopy – in-house or at synchrotron end stations. Figure 5.5 shows a photograph of the first configuration of electrospray apparatus used in this work, attached to an end station at beamline 5u1 at Daresbury SRS, UK.

The molecular coverage at the sample surface can be controlled by the length of deposition time. Coverage is not necessarily linear with deposition time, as the electrospray process depends on many factors such that the molecule flux can change over the course of minutes. A good indication of the molecule flux is the pressure in the preparation chamber. This is used when positioning the emitter in front of the entrance aperture/capillary, to find an optimum position. Another method to gauge the flux is to measure the current on the sample, as the flux of ions hitting the sample surface results in a measurable current on the order of 10 pA. During depositions, times are adjusted depending on the pressure detected in the preparation chamber and/or the current measured on the sample.

5.4 Summary

A UHV version of electrospray deposition has been developed at Nottingham, allowing thermally labile and non-volatile molecules to be studied using UHV techniques such as STM, and high resolution photoemission spectroscopy at synchrotrons. The challenge in adapting the apparatus was to produce a final preparation chamber pressure low enough for oxide or low-reactivity metal surfaces to be exposed to, while allowing a molecular beam to pass from the emitter, in air, through to vacuum. This was achieved by using a series of differentially pumped chambers, connected by small apertures, allowing the pressure towards the preparation chamber to reduce while still letting the collimated molecular beam pass through. This apparatus was used in this work to deposit N3 onto the rutile $\text{TiO}_2(110)$ and $\text{Au}(111)$ surfaces.

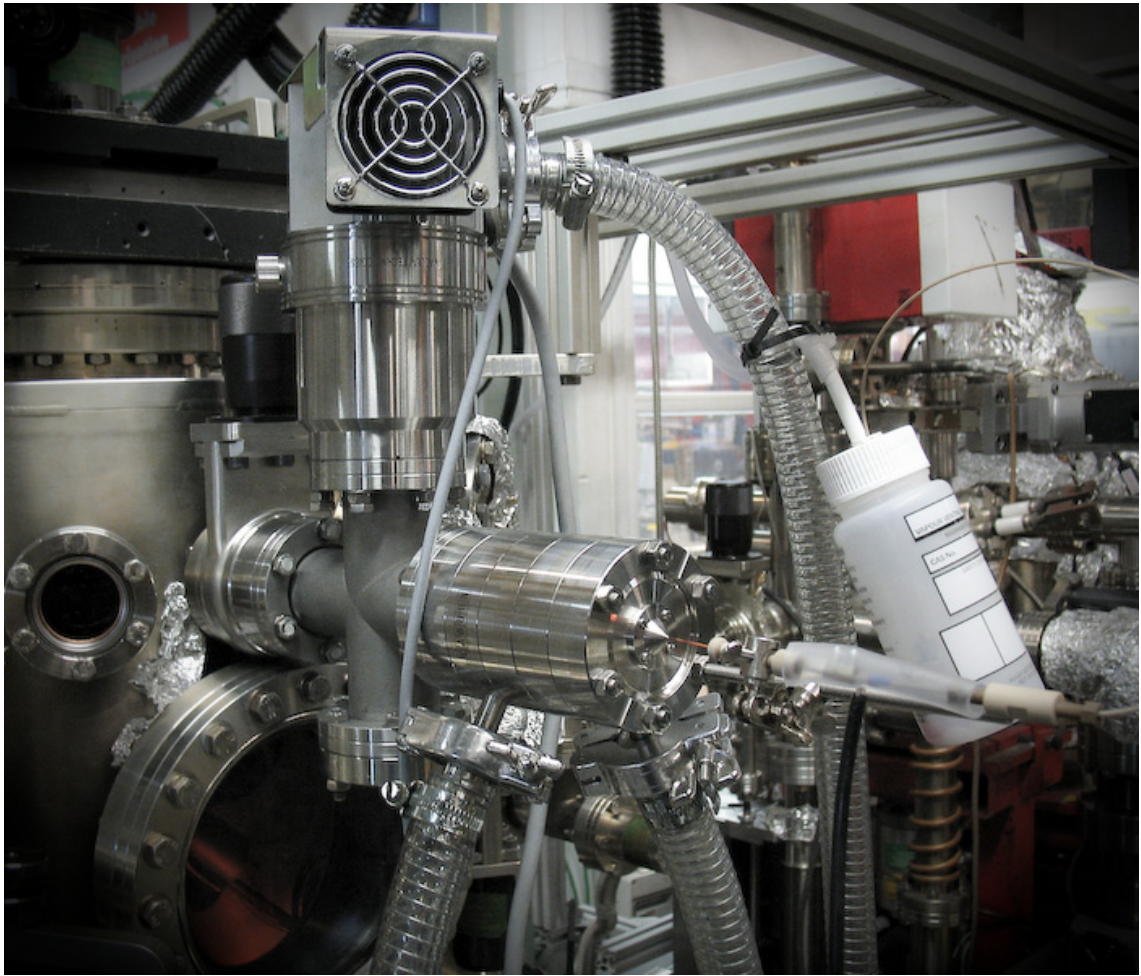


FIGURE 5.5: Photograph of the first configuration of electro spray apparatus used in this work, attached to an end station at beamline 5u1 at Daresbury SRS, UK.

CHAPTER 6

N3 on TiO₂(110)

6.1 Introduction

In this chapter the system of N3 adsorbed on rutile TiO₂(110) is explored. This system models the interface of the N3 dye adsorbed to nanostructured TiO₂ which is used in dye-sensitised solar cells (DSCs). The N3 dye, shown in Figure 6.1, is of particular importance because it is the most efficient sensitiser found for DSCs to date.[9] In the effort to develop DSCs to their full potential, it is important to understand the subtle electronic properties that enable this system to give the DSC such a high incident-photon-to-current conversion efficiency. The work described in this chapter takes steps towards elucidating our understanding of this.

The electronic structure of N3 on TiO₂ had previously been studied using photo-emission,[68, 69, 70] and charge transfer within the system had been studied using infrared transient absorption[71], and time-resolved femtosecond absorption spectroscopy[72] of *ex situ*-prepared monolayers. No *in situ*-prepared study of this system had been achieved, however, because there has previously been no UHV deposition technique available that is compatible with N3. Molecules that form a solid at room temperature are typically deposited in UHV by thermal sublimation, i.e. by heating them until they change state from a solid to a gas. The N3 molecule is however non-volatile; it cannot make the transition from a solid to a gas. This is because the molecule is thermally labile, meaning that it breaks down upon heating. Thermal sublimation is therefore not a viable deposition method for this molecule.

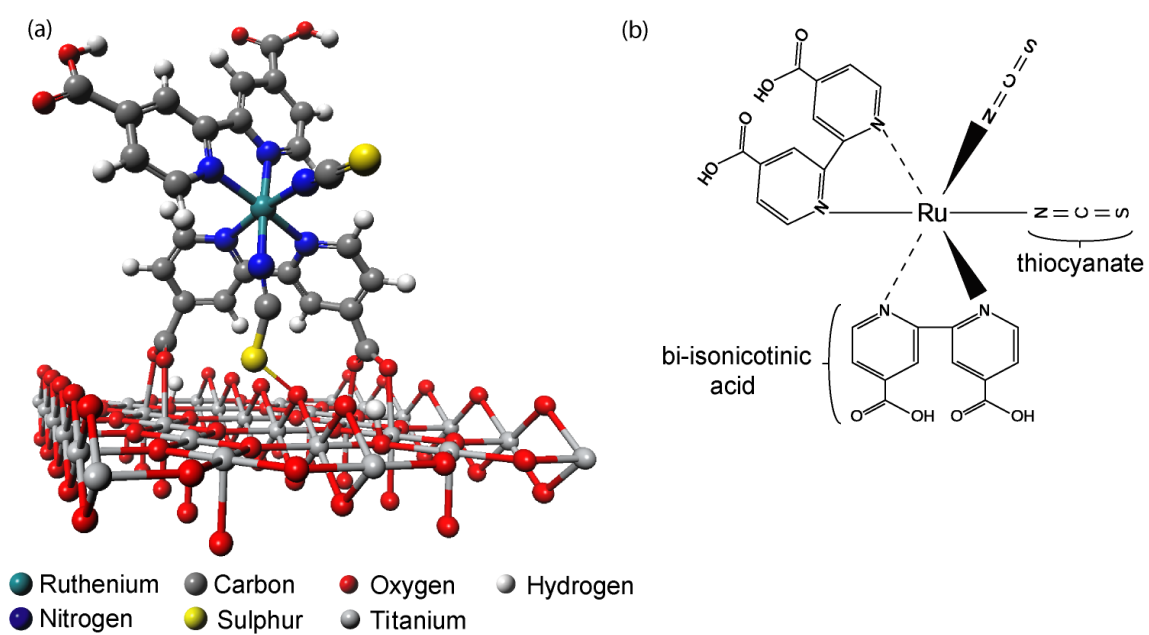


FIGURE 6.1: a) N₃ molecule adsorbed on rutile TiO₂(110), calculated using CASTEP[8] at the DFT-GGA level (see Section 6.2 for details), and b) chemical structure of the N₃ molecule.

This work represents the first *in situ* deposition of N3 on rutile TiO₂(110). Using an ultra-high vacuum (UHV) electro-spray deposition system we can form monolayers and multilayers of the dye on a well-defined TiO₂(110) surface. The electro-spray instrument is described in Chapter 5 and allows non-volatile molecules to be deposited at pressures between 1×10^{-7} and 1×10^{-9} mbar. Unlike *ex situ* deposition methods, this technique allows the surface reconstructions and cleanliness of the TiO₂(110) substrate to be preserved, excepting some hydroxylation of the bridging O atoms due to residual gases in the UHV chamber,[73] which is not expected to influence the binding of the dye via Ti atoms.

Real DSC devices are based on the adsorption of the dye to the surface of nanostructured anatase TiO₂, for which the crystal facets are predominantly the (101) surface. However, the adsorption geometry of the primary binding ligand of N3 – bi-isonicotinic acid – to the surfaces of both rutile TiO₂(110) [15] and anatase TiO₂(101) [16] is of essentially the same character, and the optical band gaps of the different phases are close at 3.05 [17] and 3.20 eV [7], respectively. The study of N3 adsorbed *in situ* on a rutile TiO₂(110) surface under UHV conditions therefore provides a unique opportunity to study the underlying chemical physics of DSCs in detail. Using a single crystal substrate as opposed to a nanostructured one, is beneficial in the surface science techniques performed here, as a well-defined periodic structure is required to get molecules in the same adsorption state to study. The rutile TiO₂(110) surface is chosen here over the anatase TiO₂(101) surface because it is easier to work with and cheaper. If anatase is annealed above 800°C by mistake it turns to rutile, and it has a maximum area of approximately 2×2 mm². In the measurements performed here, a large area is desirable because the sample needs to be swept during scans to prevent beam damage, so the larger the sample area the longer the maximum scan time.

In this chapter the geometric and electronic structure of N3 on rutile TiO₂(110) is studied using photoemission spectroscopy (PES), near-edge x-ray absorption fine structure (NEXAFS) spectroscopy, and density functional theory (DFT). The charge transfer between the molecule and substrate is investigated using the core-hole clock implementation of resonant electron spectroscopy (RES), and resonant x-ray emission spectroscopy (RXES). These techniques enable us to probe the occupied and unoc-

cupied states of the system in relation to the substrate conduction band and allow us to gain an insight into the charge-transfer processes that underpin DSCs.

6.2 Method

Experiments were carried out at the surface science undulator beamline I511-1 [38] at MAX II, MAX-lab in Lund, and at the SRS Daresbury UK, at beamline MPW6.1. All data presented here is from beamline I511-1, while PES and NEXAFS data were also collected at Daresbury for comparison. The I511-1 end station is equipped with a Scienta R4000 electron analyser which can be rotated orthogonally around the beam axis. A horizontal orientation with the analyser in-line with the light polarisation vector \mathbf{E} was used for PES, because the maximum flux of direct photoemission electrons ejected from a sample occurs in this direction. For NEXAFS and RPES however, Auger-type electrons are collected in preference over direct photoemission electrons, so for these measurements the analyser was orientated perpendicular to \mathbf{E} . The end station is also equipped with a VG Scienta XES350 x-ray emission spectrometer which was used for RXES. In all cases the sample was orientated near to normal emission, which corresponds to 7° off normal due to the grazing incidence geometry of the sample holder.

The rutile TiO₂(110) substrate (Pi-Kem, UK) was clamped to a Si or Ge crystal used for resistive heating of the substrate. Photographs of the mounted sample are shown in Figure 6.2 to help the reader to visualise the set-up. Cycles of sputtering with Ar ions, and annealing to $\sim 600^\circ\text{C}$, were used to prepare the surface. As an initial step, repeated cycles were performed in order to change the TiO₂ from an insulator to an n-type semiconductor through the introduction of bulk defects,[74] necessary to avoid sample charging. The substrate was deemed clean when it showed a negligible C 1s core-level signal, and the extent of surface defects – which induce states within the band gap – was kept in check by monitoring the valence band PES.

The N3 molecule (Solaronix SA, Switzerland) was deposited by *in situ* UHV electropray deposition, the details of which are described in Chapter 5. A solution of ~ 5 mg of N3 in 200 ml of a 3(methanol):1(water) mixture was held in a sealed reser-

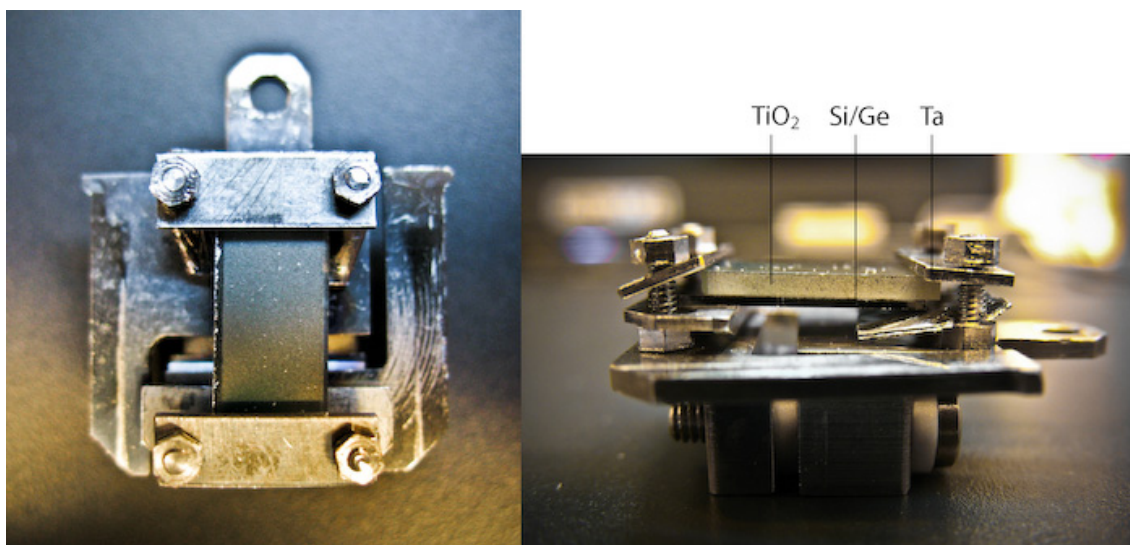


FIGURE 6.2: Photographs showing a TiO₂ substrate clamped using Ta to a Si crystal.

voir under pressure, produced either by applying 0.5 bar N₂ or by putting the liquid in a syringe and applying a gentle pressure by hand. A Taylor cone was produced by holding the electrospray emitter at a potential of 2.3 kV relative to ground. With the hand valve to the preparation chamber open but the emitter voltage turned off and thus no electrospray process occurring, the pressure in the preparation chamber was 4×10^{-8} mbar. With the voltage turned on the preparation chamber pressure rose to 2×10^{-7} mbar, the additional pressure being due to residual solvent molecules in the molecular beam. The sample was optically aligned with the electrospray system using a laboratory light source.

For the electron spectroscopy data, the total instrument resolution ranges from 40-330 meV for PES and from 90-170 meV for NEXAFS and RES. All PES spectra have been calibrated to the substrate O 1s peak at 530.05 eV,[75] and a Shirley background was subtracted before curve-fitting using Voigt functions. NEXAFS and RES spectra were taken over the N 1s absorption edge, and were measured using the electron analyser. For NEXAFS, the surface-sensitive nitrogen Auger yield was used for the monolayer, and the deeper-probing secondary electron yield was used for the multilayer. For the RES data, the photon energy was scanned over the N 1s absorption edge while measuring the valence band photoemission. NEXAFS and RES

spectra were normalised to the photon flux.

Density functional theory (DFT) calculations were carried out as an aid to understanding the experimental data. The N₃/TiO₂(110) bonding geometry was optimised using CASTEP[8] at the DFT-GGA level with a plane wave basis set cut-off of 300 eV and the Perdew Burke Ernzerhof functional. Atoms in the substrate were constrained to their bulk lattice positions, while atoms in the molecule were unconstrained and optimised using a Broyden-Fletcher-Goldfarb-Shanno algorithm.[76] The same parameters were used to obtain the free molecule geometry, which was then used with a Z+1 approximation to calculate the molecular orbitals.

For the photon spectroscopy data, electrons were resonantly excited from the N 1s core level to unoccupied levels (RXES). The sample was illuminated with a fixed photon energy of either 398.85 eV to excite to the LUMO, or 400.15 eV to excite to the LUMO+1. The energies of emitted photons were measured using the x-ray emission spectrometer, collecting over the approximate energy range of 380-420 eV. This includes both the valence band and an elastic peak if one is present. The spectrometer was set up to have an optimum geometry for collection of photons in the chosen energy range. Since the count rate for x-ray emission of surface N atoms is so low, the spectrometer was optimised using a boron nitride crystal in place of the sample. This gives a much larger signal than a monolayer or multilayer of N₃ on TiO₂, for which the N atoms are only on the surface as opposed to being in the bulk, and only comprise 6 of the molecule's 43 atoms.

The x-ray emission signal was maximised by opening the monochromator exit slit to its widest value of 500 μ m, as the more photons incident on a sample, the more are emitted. This meant that the total instrument resolution was approximately 1 eV. The spectra were calibrated to a first approximation by comparison with the valence band as measured using photoemission. That the spectra are not calibrated exactly is not a problem because the results are used here for qualitative interpretation only. For all measurements, the sample was swept continuously to avoid beam damage.

6.3 Results

The samples used to create the following spectra are classed as either *monolayer* or *multilayer*. Here a monolayer is classed as a sample having the vast majority of molecules directly adsorbed to the surface and a multilayer as having a film of molecules thick enough that the majority of photoelectrons in PES come from molecules above the first adsorbed layer. Using the O 1s and S 2p PES spectra, the multilayer is estimated to be between two and three layers thick. Binding energies of the peaks discussed are summarised in Table 6.1.

TABLE 6.1: Table of binding energies (eV) calibrated to the substrate O 1s peak at 530.05 eV.[75]

PES		Peak BEs (eV)	
		monolayer	multilayer
O 1s	TiO ₂	530.05	530.05
	C=O & COO ⁻	531.5	531.5
	C-OH	533.1	533.1
S 2p	bonded	162.4	162.4
	non-bonded	161.7	161.7
C 1s	pyridine	285.0	-
	thiocyanate	286.0	-
	carboxyl	288.6	-
Ru 3d		280.6	-
N 1s	thiocyanate	397.8	-
	pyridine	399.8	-
valence band	HOMO	1.0	-
N 1s NEXAFS			
unshifted	LUMO	0.3	-
aligned to optical data	LUMO	-1.3	-

6.3.1 Adsorption

Figure 6.3 shows the O 1s photoelectron spectra of the monolayer and multilayer, measured using $h\nu = 600$ eV. For the monolayer, the TiO₂ substrate oxygen peak

dominates the spectrum. The two smaller peaks are due to the carboxyl O in the bi-isonicotinic acid (4,4'-dicarboxy-2,2'-bipyridine) ligands of the N₃ molecule. For isolated N₃, two equally intense O 1s peaks are expected due to the equivalent number of carbonyl (C=O) and hydroxyl (C–OH) oxygen atoms (4:4). In the multilayer, these two molecular O 1s peaks are indeed approximately equal in intensity, implying that the majority of detected photoelectrons come from N₃ molecules with negligible inter-molecular and molecule-surface bonding through the bi-isonicotinic acid ligands.

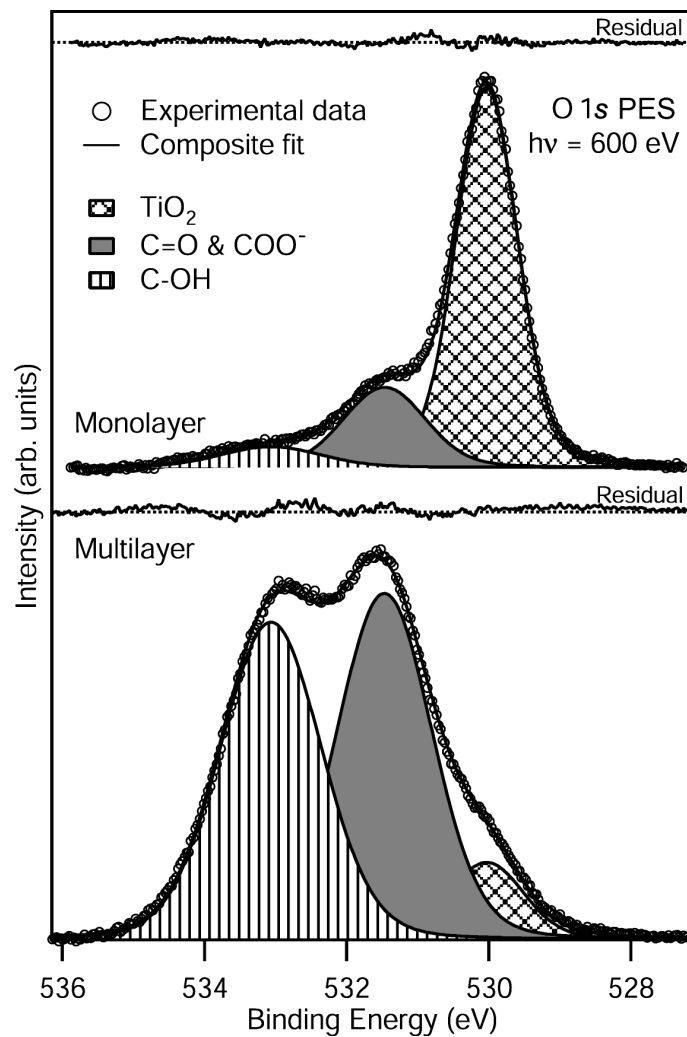


FIGURE 6.3: O 1s core-level spectra measured using $h\nu = 600$ eV. Total instrument resolution was ~ 180 and 340 meV for the mono- and multilayers respectively.

In previous studies, bi-isonicotinic acid has been found to bond to TiO₂ through deprotonation of the carboxyl (COOH) groups, in a 2M-bidentate structure.[15, 75, 77] This is a common bonding arrangement for pyridine carboxylic acids on the TiO₂ surface.[78, 79, 80] Once a carboxyl group has deprotonated, the two O atoms share an electron and are chemically equivalent. The binding energy (BE) of this O species (COO⁻) is similar to that of the carbonyl O in the isolated molecule (C=O).[15] The COO⁻&C=O:C-OH intensity ratio found for the monolayer is 3.2:1. Assuming that all molecules are bonded to the surface in an equivalent way, this is close to 3:1 which would imply that for each molecule two carboxyl groups are bonded to the surface.

Figure 6.4 shows S 2*p* photoelectron spectra of the monolayer and multilayer, measured using $h\nu = 225$ eV. Along with the O 1*s* PES spectra, the S 2*p* PES spectra are indicative of the bonding of N3 to the TiO₂ surface. S 2*p* is a doublet state with spin-orbit splitting of 1.1 eV[81]. For the monolayer spectrum, a good fit is obtained only when a pair of chemically shifted doublets are used. This implies that the S atoms exist in two different chemical environments. For the multilayer spectrum, the low BE peak dominates, so it is assumed that this represents a S atom that is not involved in bonding to the surface. The peak shifted to higher BE by 0.7 eV is therefore attributed to S atoms interacting with the surface. The ratio of these two peaks for the monolayer is 1:1.

Two possible bonding geometries are consistent with the measured data, both involving the interaction of one S atom of a thiocyanate (NCS) ligand with the surface. In the first model, both binding carboxyl groups are on the same bi-isonicotinic acid ligand, while in the second model they are on different bi-isonicotinic acid ligands. The latter is often proposed for the adsorption of N3 on the (101) surface of anatase TiO₂,[82] although no real consensus has so far been reached. For the (110) surface of rutile however, the most plausible bonding geometry is one in which both binding carboxyl groups are located on the same bi-isonicotinic acid ligand as shown in Figure 1.3 (a). This has previously been proposed for *ex situ*-prepared monolayers of N3 on nanostructured TiO₂. [70]

Figure 1.3 (a) represents a geometry optimisation of N3 on TiO₂(110), calculated using DFT. The structure has one S atom bonded to a surface bridging O atom, and

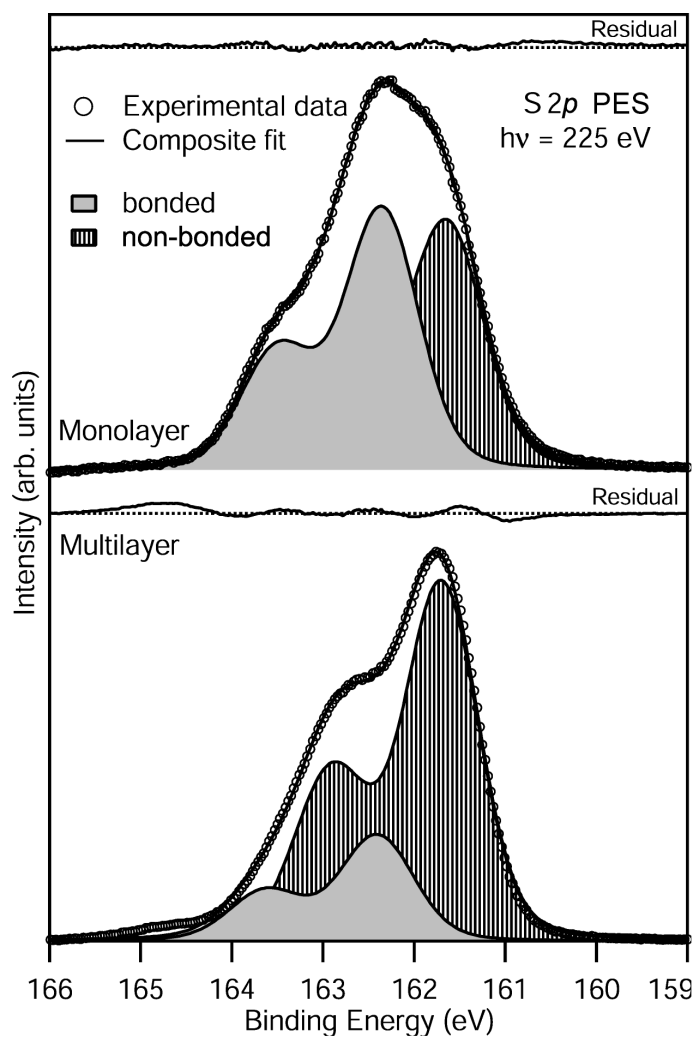


FIGURE 6.4: S 2p core-level spectra measured using $h\nu = 225$ eV. Total instrument resolution was ~ 50 and 140 meV for the mono- and multilayers respectively.

the O atoms of both carboxyl groups from one bi-isonicotinic acid ligand bonded to surface Ti atoms. This represents an overall energy 1.2 eV lower than the geometry calculated for the structure in which the two bonding carboxyl groups are on different bi-isonicotinic acid ligands, the additional energy resulting from increased strain within the molecule. The proposed model of Figure 1.3 (a) is also shown in our calculations to be 0.7 eV more stable than a geometry with no S bonded to the surface, consistent with the S 2*p* spectra shown in Figure 6.4.

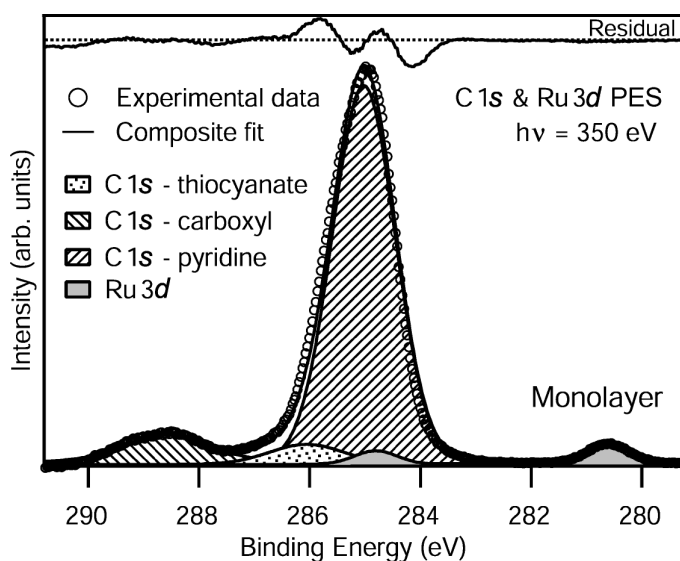


FIGURE 6.5: C 1*s* core-level spectrum measured using $h\nu = 350$ eV. Total instrument resolution was ~ 90 meV.

Figure 6.5 shows a photoelectron spectrum of the C 1*s* and Ru 3*d* states for the monolayer, measured using $h\nu = 350$ eV. There are three resolvable chemical environments for C in N3: the pyridine, carboxyl and thiocyanate groups, in an atomic ratio of 10:2:1 respectively. The ratio found for the monolayer is 10.2:1.2:1, the discrepancy most likely due to half of these groups being bonded to the surface and therefore shadowed by the rest of the molecule. Previous studies of bi-isonicotinic acid – containing the pyridine and carboxyl carbon atoms – were used to identify the peaks.[83, 46]

Ru 3*d* is a doublet state with a spin-orbit splitting of 4.2 eV[84]. The lower BE

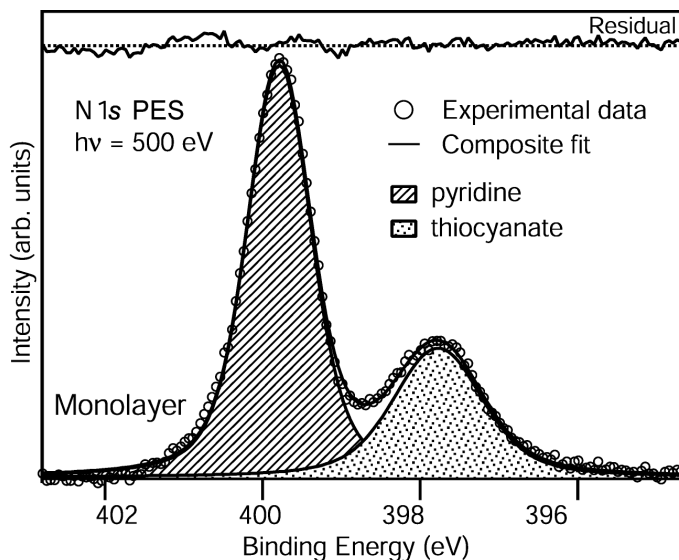


FIGURE 6.6: N $1s$ core-level spectrum measured using $h\nu = 500$ eV. Total instrument resolution was ~ 140 meV.

Ru $3d_{5/2}$ peak can be seen clearly in the spectrum at 280.6 eV. This is approximately 0.6 eV higher than metallic ruthenium[84] and is thus consistent with the Ru²⁺ oxidation state of the metal centre. This strongly suggests that the molecule has retained its molecular integrity during deposition.

Figure 6.6 shows a N $1s$ photoelectron spectrum of the monolayer, measured using $h\nu = 500$ eV. N3 has a ratio of 2(pyridine):1(thiocyanate) N atoms. This is reflected in the 2.3:1 peak intensity ratio found for the N $1s$ monolayer PES spectrum, providing further evidence that the molecules arrive at the surface in their entirety.

6.3.2 Energy level alignment

In a DSC, electrons from high-lying occupied molecular orbitals in the dye are photoexcited to previously unoccupied molecular orbitals. For subsequent electron injection into the TiO₂ substrate, the unoccupied level of the dye involved in the transfer must overlap with the TiO₂ conduction band continuum of states. Spectra representing the occupied and unoccupied states of the N3 monolayer have here been placed on a common binding energy scale following the procedure outlined in Section 4.2.

This picture is key in identifying the charge transfer processes that can occur in the model N3/TiO₂ DSC.[85, 86, 87, 88] Also of note is that the substrate conduction band edge is very close to the Fermi level, indicating little or no band bending.

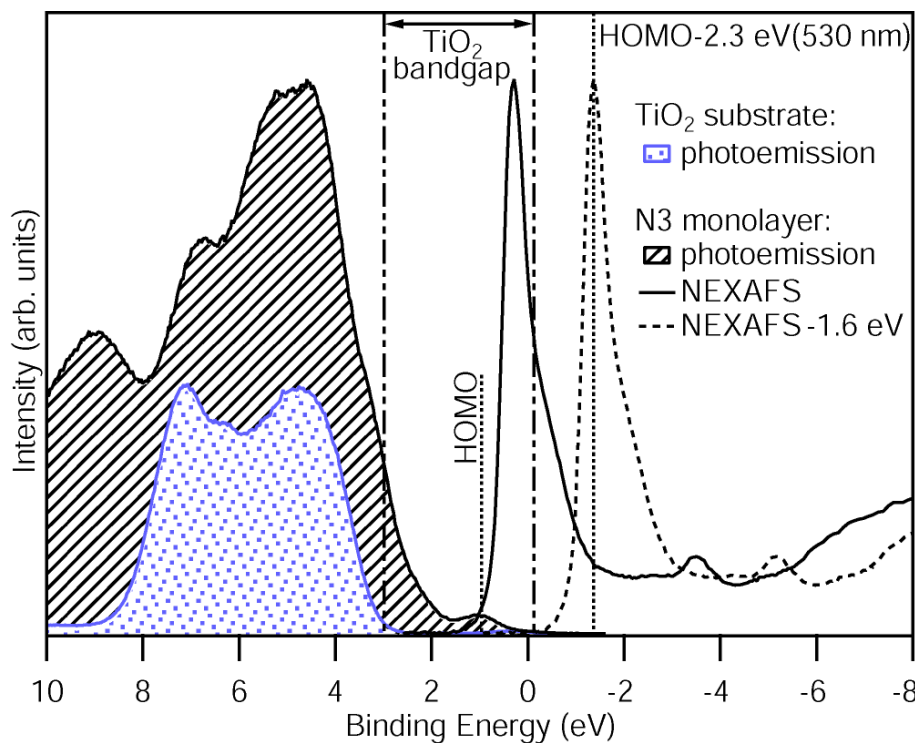


FIGURE 6.7: Valence band PES spectra of the clean substrate and of a monolayer of N3, adjacent to a N 1s NEXAFS spectrum of the N3 monolayer. The NEXAFS spectrum is also shown shifted by -1.6 eV to align with the optical HOMO-LUMO gap of 2.3 eV. The optical band gap of TiO₂[17] is also indicated. The PES spectra were measured using $h\nu = 110$ eV and had a total instrument resolution of ~ 40 meV. The NEXAFS spectrum was taken over the photon energy range $h\nu = 396.6$ - 425.0 eV and had a photon energy resolution of < 170 meV.

Figure 6.7 shows the N 1s (Auger yield) NEXAFS and valence PES spectra for a monolayer, along with the clean substrate valence PES (measured at $h\nu = 110$ eV). While the N 1s core level (Figure 6.6) consists of two peaks, the pyridine N was used to place the NEXAFS on the common BE axis, as it is clear that the N 1s NEXAFS is dominated by pyridine-like π^* orbitals as seen for the bi-isonicotinic acid ligand on its own.[89, 83] Moreover, in our DFT calculations of the N3/TiO₂ system, the lowest unoccupied molecular orbital (LUMO) is located on a bi-isonicotinic acid ligand and

the central Ru atom, with no intensity on either thiocyanate ligand.

While peaks derived from the bi-isonicotinic acid N atoms are then located energetically in the right place, any peaks deriving from thiocyanate N will appear artificially shifted by approximately 2 eV to higher BE. DFT calculations show several orbitals localised on the thiocyanate ligands which are ~ 3 eV lower in BE than the LUMO. The shoulder on the low BE side of the LUMO is attributed to these levels; the peaks would appear 2 eV higher in BE than their calculated energies, placing them ~ 1 eV lower in BE than the LUMO, as observed. This shoulder is also the only significant feature in the N 1s NEXAFS spectra that is not present for bi-isonicotinic acid on TiO₂. A similar approach has been used elsewhere in interpretation of the C 1s NEXAFS spectra of benzoic acid, based on the C 1s BE difference between the phenyl and carboxyl C atoms.[46]

The PES peak at 1.0 eV is the highest occupied molecular orbital (HOMO) and is noteworthy as it narrows the HOMO-LUMO gap as compared with the TiO₂ band gap, allowing visible light excitations which are fundamental to the DSC mechanism.[82] The HOMO is involved in the initial photoexcitation step within the real DSC.[82] Optical absorption spectra of N3 on TiO₂ show maxima which correspond to photon energies that photoexcite electrons from the HOMO to various unoccupied levels. The lowest in energy of these maxima is centred at a wavelength of 535 nm,[90] which corresponds to a photon energy of 2.3 eV. This is also the absorption maximum with the highest incident-photon-to-current conversion efficiency.[2] The final state of the 535 nm photoexcitation in the real DSC is predicted then to lie 2.3 eV lower in BE than the HOMO. The 535 nm absorption maximum is attributed to the HOMO \rightarrow LUMO transition, corresponding to a Ru(4d)NCS \rightarrow bpy(π^*)COOH transition. The spatial distribution of the HOMO and LUMO are shown in Figure 6.13 and are discussed later in the context of charge transfer dynamics.

In the present case where the unoccupied states are probed using N 1s NEXAFS, a *core* exciton (bound electron-hole pair) is created whereas in a real DSC a *valence* exciton is created. The presence of a hole in both NEXAFS and optical absorption shifts the unoccupied states to higher BE with respect to the ground state. The BE of the excitons, equivalent to the amount by which the unoccupied levels shift, is

attributed to a combination of the Coulomb interaction between the hole and excited electron, and the rehybridisation of the molecular states upon core- or valence-hole creation.[45] Comparing the HOMO-LUMO gap as measured using optical excitation (2.3 eV) to the HOMO-LUMO gap for the core-excited system (0.7 eV), the difference in energy is 1.6 ± 0.1 eV. This is indicative of the difference between the N 1s core exciton and valence exciton BEs for this molecule. This value is slightly larger than the difference in BE of 1.3 eV found for pyridine,[45] a molecule closely related to the bi-isonicotinic acid ligands of N3. Since the Coulomb attraction of the core hole is responsible for the BE of a core exciton to be larger than that of a valence exciton, this effect is perhaps greater in N3 due to less efficient screening of the N 1s core hole, caused by the metal binding to the N atoms.

Shifting the NEXAFS spectrum into alignment with the 2.3 eV optical HOMO-LUMO gap, as shown in Figure 6.7, causes the LUMO to lie above the substrate conduction band edge, and thus in a real solar cell would permit electron injection from that level into the substrate. This contrasts with the energy alignment of the core-excited system here, where the LUMO-to-substrate transition is forbidden due to overlap with the substrate band gap. In the next section, electrons excited to the LUMO are therefore used as a reference, allowing us to probe electron injection from those remaining unoccupied levels that lie above the substrate conduction band edge.[47, 87]

6.3.3 Charge transfer

In DSCs, a key step in the photovoltaic process is electron injection from the excited molecule into the substrate conduction band. Resonant electron spectroscopy (RES) and resonant x-ray emission spectroscopy (RXES) are used here to investigate molecule-to-substrate charge transfer. These techniques enable us to observe the delocalisation of charge from unoccupied molecular valence levels. The core-hole clock implementation of RES allows us to quantify an upper time limit in which this occurs. The techniques used here are described in detail in Chapter 4.

Resonant electron spectroscopy

The RES data was collected in a similar way to the NEXAFS data. In both cases the photon energy was scanned over the N 1s absorption edge, covering the lowest unoccupied levels. For NEXAFS, the electron analyser was used to measure spectra at each photon energy step of either the N Auger or a section of the secondary electron tail, whereas for RES, valence band spectra were measured. It is in this region that interesting resonant behaviour which gives information about charge transfer is seen.

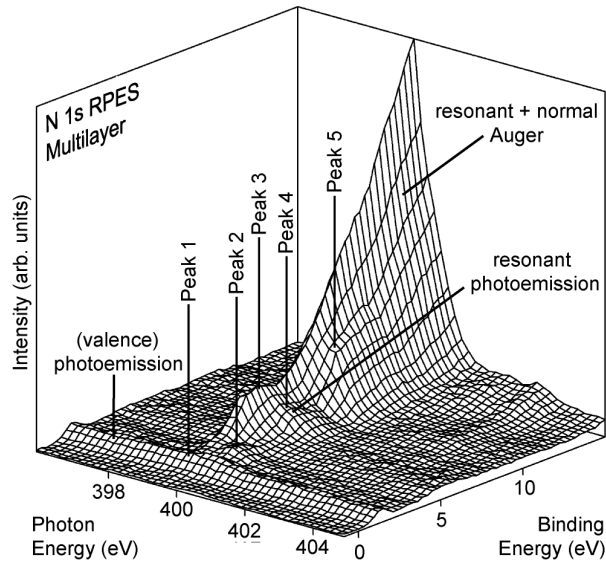


FIGURE 6.8: N 1s RES data for the N3 multilayer. Valence band spectra with a BE range of 4-20 eV were acquired over the photon energy range $h\nu = 397-405$ eV. Photon energy resolution was < 170 meV.

Figure 6.8 shows a N 1s resonant electron spectrum for the multilayer, featuring peaks arising from the processes described in Section 4.3. Peaks 2-5 in the figure are due to resonant photoemission. Normal Auger and resonant Auger peaks can not be separated here; together they are responsible for the most intense peak seen in the spectrum. As with normal Auger, the resonant Auger here disperses with constant KE. An exception to this behaviour occurs for the Auger resonant Raman (ARR) regime[47, 48] as described in Section 4.3.2. This requires that the photon energy distribution is narrower than the natural line width of the electronic energy levels, which is not the case in this experiment.

The presence of resonant photoemission and resonant Auger peaks indicates that the electron excited to an unoccupied level in x-ray absorption is still present; it has not delocalised and hence has not been injected into the substrate conduction band. This is to be expected for the multilayer. For the monolayer however, we look to the diminishing intensity of resonant peaks to indicate the extent to which charge injection to the substrate is occurring. Since resonant Auger can here not be separated from normal Auger, we are left with resonant photoemission to tell us about charge transfer.

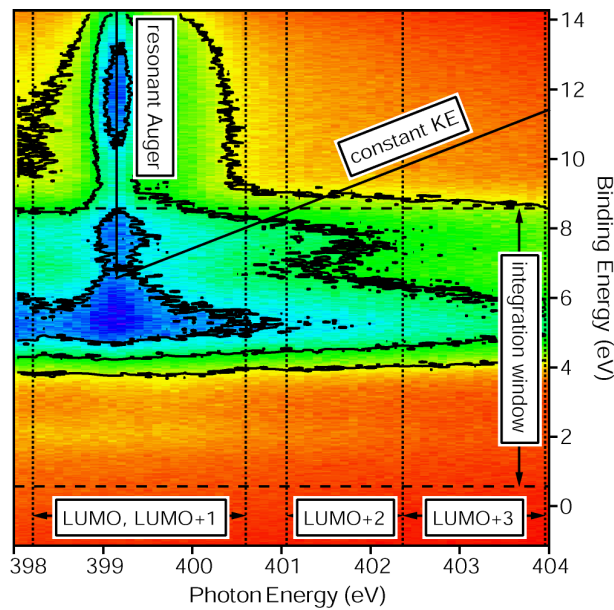


FIGURE 6.9: N $1s$ RES data for the N₃/TiO₂ monolayer. Valence band spectra with a BE range of 4-20 eV were acquired over the photon energy range $h\nu = 397$ -405 eV. Photon energy resolution was < 170 meV.

Figure 6.9 shows a 2d N $1s$ resonant electron spectrum for the monolayer. The unseparable normal and resonant Auger peaks all occur to higher BE of the ‘constant KE’ line on the figure. The line was placed at the low BE limit of the Auger peak at the LUMO, based on a curve-fit of the Auger tail minus the pre-edge structure. Any peaks to lower BE of this line then, arise from photoemission and resonant photoemission only.

As discussed in the previous section, the LUMO lies in the substrate band gap,

so electron injection from this level is forbidden. Electron injection is, however, energetically allowed from the LUMO+1, LUMO+2 and LUMO+3. As shown in Figure 6.9, integrating over a 0.6-8.6 eV BE window includes only photoemission and resonant photoemission over the LUMO+2 and LUMO+3 levels. This integration has been performed for both the multilayer and monolayer as shown in Figure 6.10. Any peaks at the LUMO+2 or LUMO+3 are due solely to resonant photoemission, as direct photoemission contributes a sloping background only.

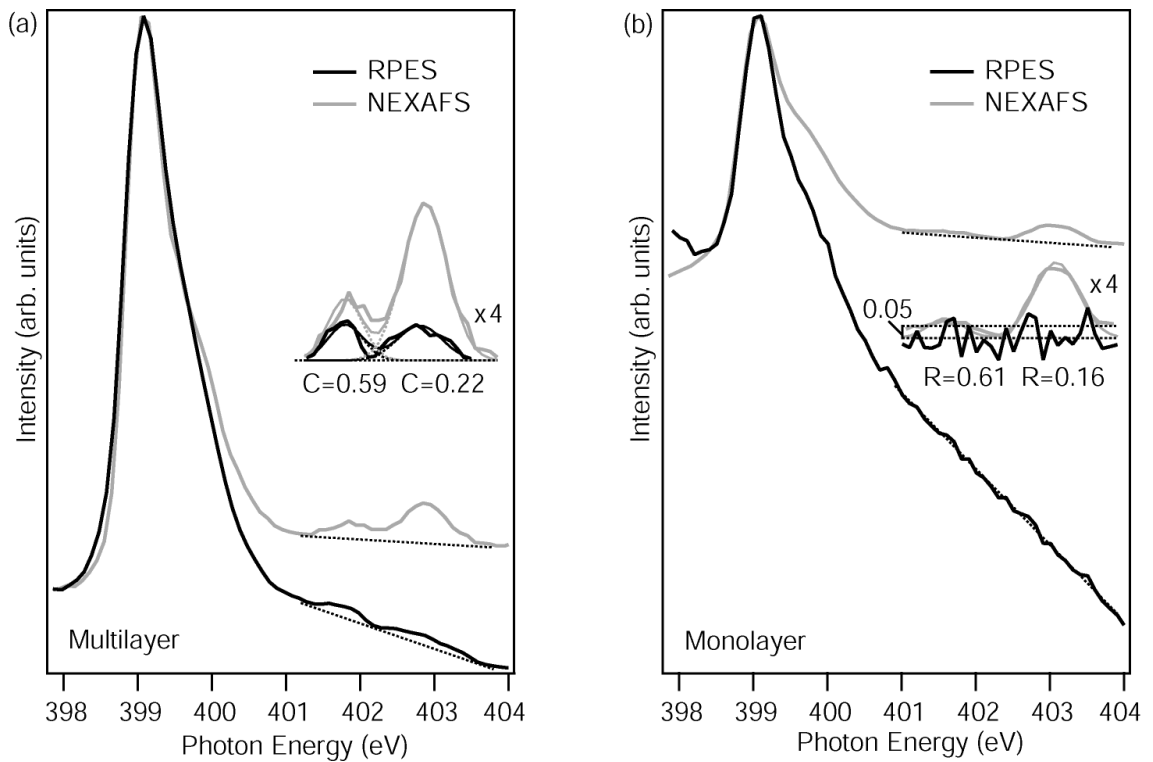


FIGURE 6.10: N 1s RES and N 1s NEXAFS spectra of the N3 (a) multilayer and (b) monolayer. The RES spectra shown here are BE integrations from 0.6-8.6 eV over the data sets, and peaks at the LUMO+2 or LUMO+3 are due solely to resonant photoemission. Also shown are 4 \times magnifications of the LUMO+2 and LUMO+3 region. The values C and R represent the RPES:NEXAFS intensity ratios of the peaks shown.

In Figure 6.10 the RES spectra are normalised to the LUMO, as are the corresponding NEXAFS spectra which are also shown. In the NEXAFS spectra, the peaks represent the unoccupied levels' full intensities, whereas for RES, the LUMO has its

full intensity but the LUMO+1, LUMO+2 and LUMO+3 may be depleted by charge transfer. For the multilayer it can be seen that the LUMO+2 and LUMO+3 are smaller in the RPES than the NEXAFS. This ratio is attributed purely to matrix element effects due to the different techniques used.[86] For the monolayer RPES however, these peaks have been reduced down to the level of noise, indicating that charge transfer is occurring from these levels.

The core-hole clock implementation of RES can be used to quantify the electron injection timescales from these levels, and is described in Section 4.3.3. The technique uses the fact that if charge transfer is occurring, it must be competing with the de-excitation of the excited state via resonant photoemission or resonant Auger. The time taken for de-excitation here can also be described as the lifetime of the N 1s core hole. Here we calculate the time taken for electron injection into the substrate from the LUMO+3, as this is the most significantly depleted peak. Denoting the intensity of the LUMO+3 as I , the electron injection time τ_{CT} for electrons moving from the LUMO+3 to unoccupied substrate states is given by equation 6.1.

$$\tau_{CT} = \tau_{chd} \frac{\frac{I_{coupled}^{participantor}}{I_{coupled}^{NEXAFS}}}{\frac{I_{isolated}^{participantor}}{I_{isolated}^{NEXAFS}} - \frac{I_{coupled}^{participantor}}{I_{coupled}^{NEXAFS}}} \quad (6.1)$$

The variables $I_{coupled}^{participantor}$ and $I_{isolated}^{participantor}$ represent the intensities of the LUMO+3 peaks in the RPES monolayer and multilayer respectively. These values are each normalised by the total cross-sections as provided by the NEXAFS intensities $I_{coupled}^{NEXAFS}$ and $I_{isolated}^{NEXAFS}$. The variable τ_{chd} is the average N 1s core-hole lifetime and is here assigned the value of 6 fs; this is the value as measured experimentally for the N₂ molecule.[91] It has been shown that core-hole lifetimes are largest for *atomic* Auger transitions and become smaller for *molecular* transitions, the exact values depending upon the electronegativity of the ligands.[92] An upper limit on the core-hole lifetime then, would be that for atomic N which has been calculated as 7.5 fs.[92]

Here $I_{coupled}^{participantor}/I_{coupled}^{NEXAFS} = 0.16$ and $I_{isolated}^{participantor}/I_{isolated}^{NEXAFS} = 0.22$, giving an upper time limit of 16 fs for the electron injection time into the substrate from this level (with an absolute upper value of 20 fs if the core-hole lifetime for atomic N rather

than N₂ is used). This is in agreement with the electron injection upper time limit for bi-isonicotinic acid on TiO₂ which has been found previously as 3 fs.[87] That $I_{\text{isolated}}^{\text{participator}}/I_{\text{isolated}}^{\text{NEXAFS}}$ is 0.22 and not 0.3 as found for bi-isonicotinic acid,[87] can perhaps be attributed to ultra-fast delocalisation of excited electrons *within* the molecule. Such intrinsic delocalisation would lead to reduced resonant photoemission even in the absence of charge-transfer to the substrate. Evidence of ultra-fast intra-molecular delocalisation has previously been found in the RES of a related ruthenium complex comprising three bipyridine ligands, for which little or no resonant photoemission was measured for resonances lying higher than the LUMO in the multilayer.[93] The $I_{\text{isolated}}^{\text{participator}}/I_{\text{isolated}}^{\text{NEXAFS}}$ ratio of 0.22 for the multilayer can therefore be interpreted as a combination of the aforementioned matrix element effect and intramolecular delocalisation. In the case of the monolayer, a fraction of the electrons that are localised in the multilayer are able to charge-transfer into the substrate, bringing the RPES/NEXAFS ratio from 0.22 down to 0.16, and it is these injected electrons that are investigated in the RPES analysis. In other words, intramolecular delocalisation is accounted for in equation 6.1 through the experimentally measured value of $I_{\text{isolated}}^{\text{participator}}/I_{\text{isolated}}^{\text{NEXAFS}}$.

In the previous section it was concluded that the LUMO is actively involved in the DSC photovoltaic process. Since in the RES technique the unoccupied levels are excitonically pulled down into the TiO₂ band gap, we are unable to probe the LUMO electron injection time directly. However, as also discussed in the previous section, the LUMO and LUMO+3 are both thought to be located on the bi-isonicotinic acid ligands, so electron injection is expected to occur on a similar timescale. This gives some insight into why the N3 DSC is so efficient.

An interesting characteristic of the RES data is that the photoemission enhancements observed at the LUMO resonance occur at different BEs to those observed at the LUMO+1 resonance. This can be seen most clearly in the multilayer (Figure 6.8). Here the enhancement of peak 1 – the HOMO – can be seen primarily at the LUMO+1 position rather than the LUMO. Similarly, peak 3 is enhanced only at the LUMO resonance while peaks 2, 4 and 5 occur only for the LUMO+1. For a simpler two-dimensional view, constant photon energy slices of Figure 6.8 are shown in Figure 6.11. Slices have been taken before the N 1s absorption edge (pre-edge, 396.9 eV),

representing the direct photoemission of the occupied valence levels, and also at the photon energies of the LUMO (399.3 eV) and the LUMO+1 (399.9 eV), illustrating additional resonant enhancements of the valence band states. To further illustrate, peaks 1 and 2 which are at a BE low enough that they have no or little Auger component are displayed in Figure 6.12. This time they are shown on a photon energy scale, where each peak has been integrated over the extent of its BE range.

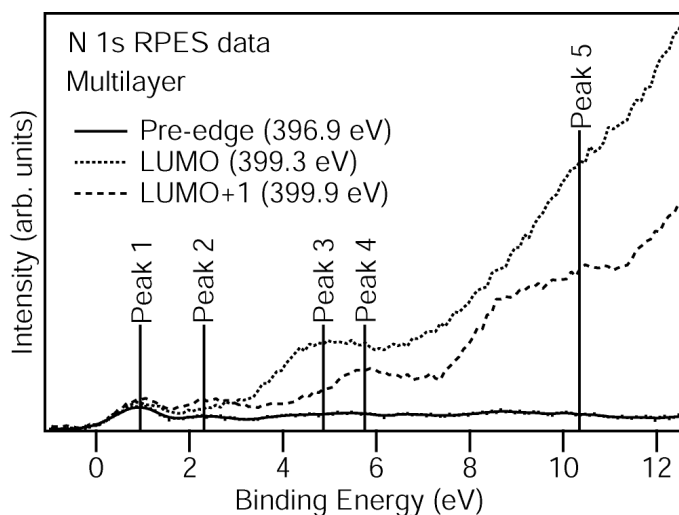


FIGURE 6.11: Photon energy slices of the multilayer RPES data shown in Figure 6.8 taken at pre-edge, LUMO and LUMO+1 photon energies, to give a clearer view of the misaligned peaks.

For resonant photoemission to occur following core-excitation (see Figure 4.3), the occupied (BE scale) and unoccupied ($h\nu$ scale) orbitals involved must have some interaction. Moreover, the largest probability for resonant photoemission will be when both electrons involved (i.e. the one that fills the core hole, and the emitted electron) are located on the same atom, specifically the site of the core hole. Resonant photoemission is in essence a special type of Auger decay, and while interatomic Auger transitions can occur,[94] the rates of these events are negligible in all but the lowest energy Auger processes. The origin of the state-dependent resonant enhancements observed for the occupied molecular orbitals observed in Figure 6.11 is therefore likely to be due to the spatial distribution of both the occupied and unoccupied orbitals involved in the core-hole decay process. More specifically, the results suggest that

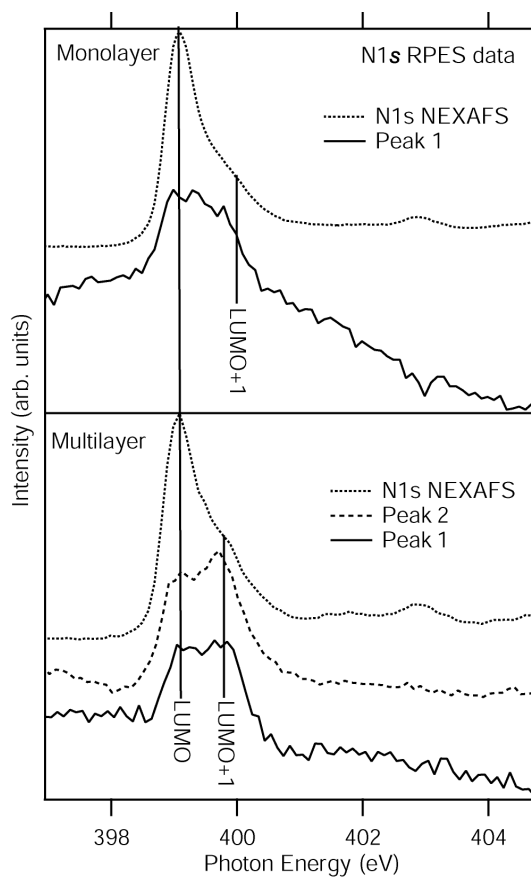


FIGURE 6.12: Peaks from the RPES monolayer and multilayer data as defined in Figure 6.11, where each peak has been integrated over the extent of its BE range.

the LUMO and LUMO+1 are located on different parts of the molecule in agreement with the previous section, where the LUMO was attributed to the bi-isonicotinic acid ligands and the LUMO+1 to the thiocyanate ligands. This is also supported by the DFT calculations (as described in Section 6.2) shown in Figure 6.13 which illustrate the spatial distribution of some of the occupied and unoccupied orbitals of a free N₃ molecule. The orbitals are labelled with their calculated energies in inverted commas, to remind the reader that these are theoretically calculated values and are not experimentally measured quantities. Shown in Figure 6.13 are the HOMO ('0.0 eV'), LUMO ('1.2 eV'), and the unoccupied level at '3.3 eV'. The latter is attributed to the LUMO+1 resonance observed at 399.9 eV in the N 1s NEXAFS for reasons outlined in the previous section.

The state-dependent enhancements of the highest occupied molecular orbitals in Figure 6.11 can be understood in terms of their spatial distribution within the molecule, and the location of the core-hole site in each of the LUMO and LUMO+1 excitations. Since the HOMO has no intensity on the N atoms of the bi-isonicotinic acid ligand, there is a negligible probability of an electron from this orbital playing any role in the participator decay (resonant photoemission) of the core hole created on excitation to the LUMO (localised as shown in Figure 6.13 on the bi-isonicotinic ligand). Indeed, there is little or no enhancement of the HOMO at the LUMO energy (399.3 eV) in Figure 6.11 above the pre-edge direct photoemission spectrum. Conversely, an electron from the HOMO can participate in the decay of the N 1s core-hole created on excitation to the LUMO+1 located on the thiocyanate ligand. A small resonant enhancement of the HOMO is therefore observed in Figure 6.11 at the LUMO+1 photon energy (399.9 eV). An analogous mechanism is proposed for the state-dependent enhancements of the other valence states observed in Figures 6.8, 6.11 and 6.12. Those occupied states located primarily on the thiocyanate ligands are able to play a role in the participator decay of the N 1s–LUMO+1 core-excited state, while those local to the bi-isonicotinic acid ligands contribute to the decay of the N 1s–LUMO state.

It is worth noting that while both the HOMO and LUMO would require some degree of overlap with the core-excited atom in order to give rise to resonant photoe-

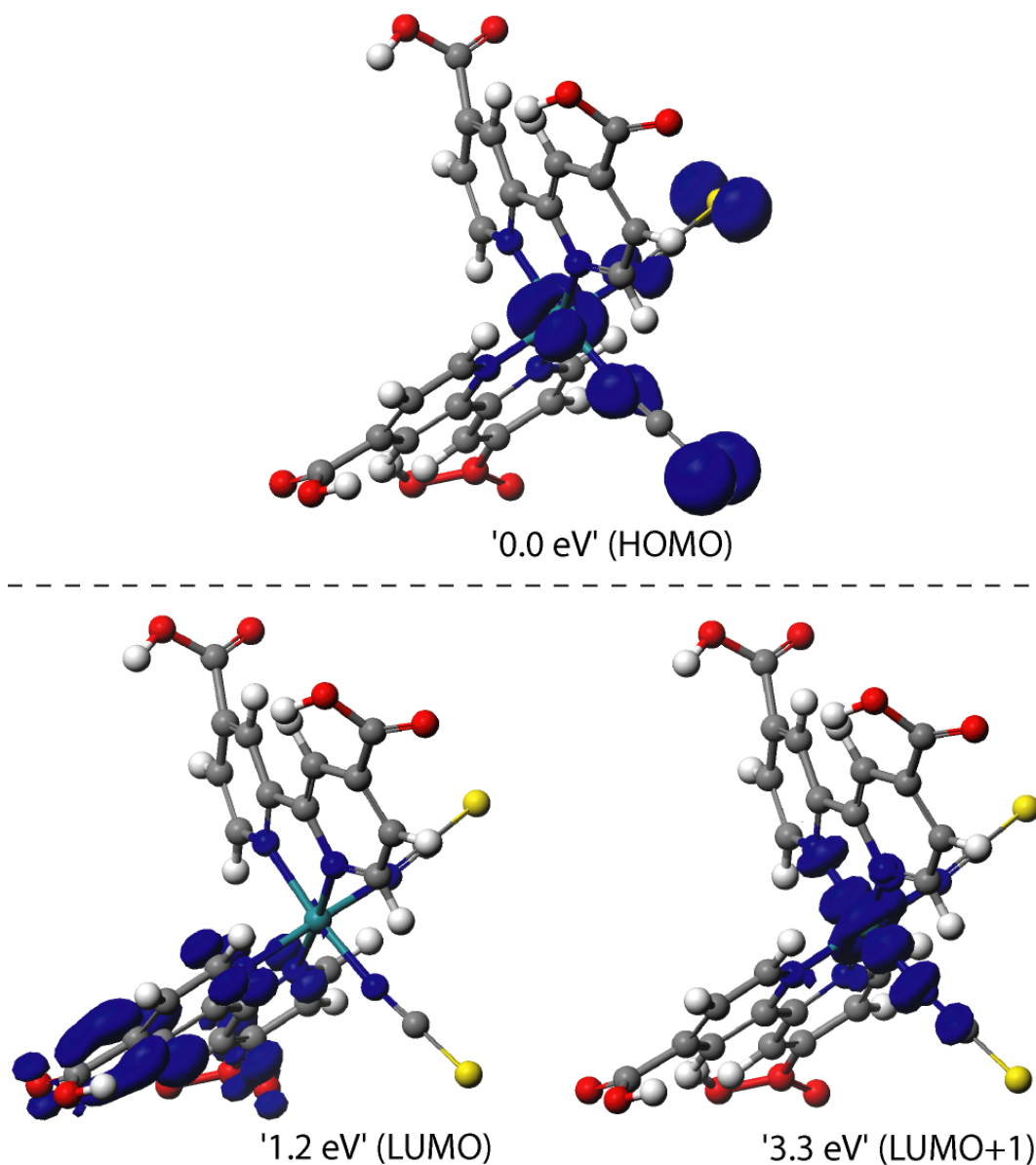


FIGURE 6.13: DFT calculations showing electron orbitals (dark blue) of a geometry-optimised free N₃ molecule. The calculated orbitals are identified with the HOMO, LUMO and LUMO+1. Since the molecule is symmetrical, the orbitals shown here on one ligand only are also present on the corresponding symmetrical ligands, and have only marginally different calculated energies. The atoms are coloured by element, with the colours as defined in Figure 1.3.

mission, only an overlap with *each other* is required for the HOMO–LUMO photoexcitation in a real solar cell. Close inspection of the calculated LUMO in Figure 6.13 reveals a small contribution on the central Ru atom of the molecule. The photoexcitation channel between the two orbitals is therefore facilitated by their overlap at the centre of the molecule.

Resonant x-ray emission spectroscopy

In preparation for taking RXES spectra, a N 1s NEXAFS spectrum was measured to assess the positions of the unoccupied levels lying close to the band gap. Photon energies were then chosen to resonantly excite electrons from the N 1s core level to the LUMO and the LUMO+1 in RXES. The RXES spectra map the valence band local to the core hole, and also feature an elastic peak which can be analysed to give information about charge transfer. The RXES technique is described in Section 4.4.

Figure 6.14 shows the N 1s NEXAFS spectrum of a multilayer of N3 on TiO₂. This figure shows how the NEXAFS spectrum was used to choose what photon excitation energies to use in RXES. The LUMO and LUMO+1 levels were chosen to be studied, and were curve-fit for the figure approximately using two Gaussians and a step-function. The results so far in this chapter have indicated that the LUMO is located on the bi-isonicotinic acid ligands and the LUMO+1 to the thiocyanate ligands of N3. If this is true then the RXES spectra measured by exciting to these levels will show those components of the valence band that interact with them. Since the resolution of the incident photon energy is large at approximately 1 eV, care must be taken that the RXES excitation energies chosen do not also excite to neighbouring unoccupied levels. For this reason, the photon energy chosen to excite to the LUMO is not the energy of the LUMO itself at 399.3 eV, but a lower energy of 398.85 eV. This gives an energy range that encompasses about half of the LUMO and a negligible amount of the LUMO+1. For the LUMO+1 a photon energy of 400.15 eV was chosen for RXES, which encompasses as much of the LUMO+1 as possible and a small amount of the LUMO.

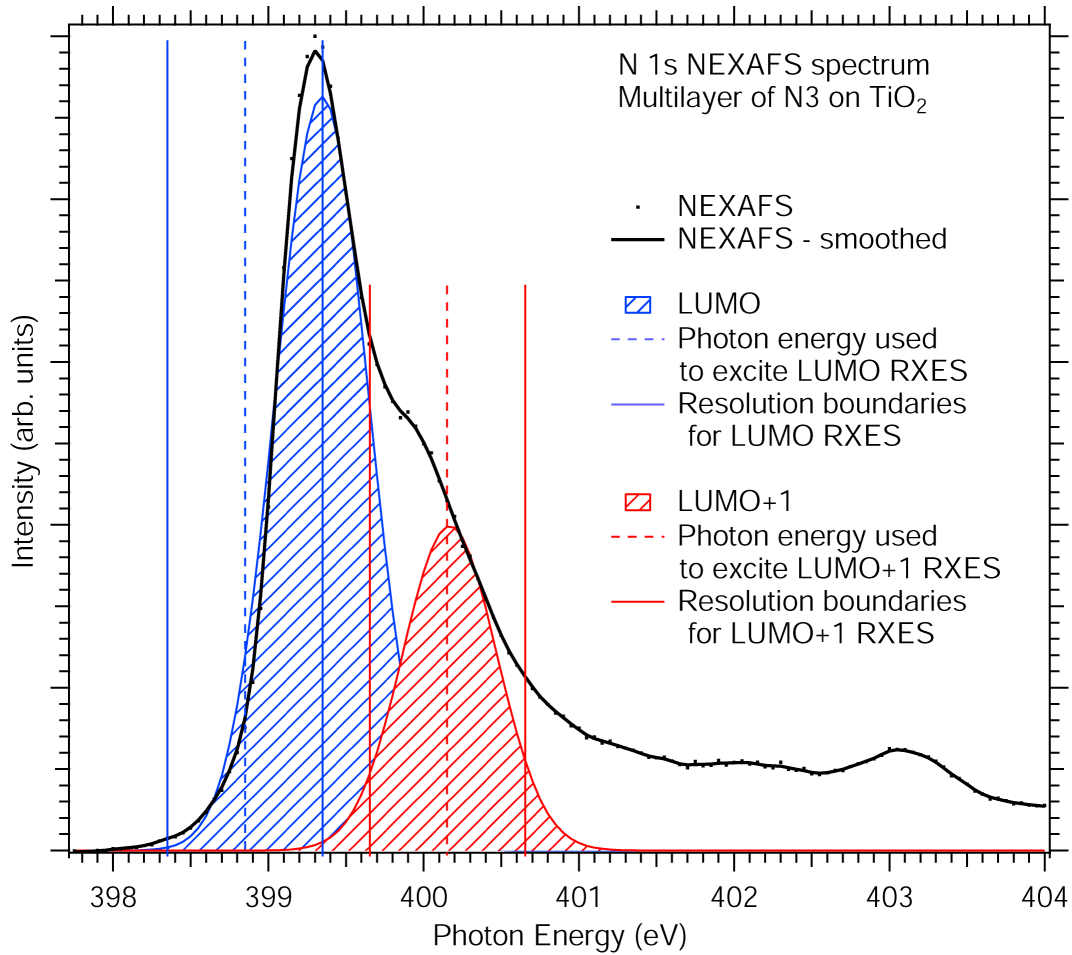


FIGURE 6.14: N $1s$ NEXAFS spectrum of the N₃ multilayer, with a photon energy resolution of ~ 1 eV. The spectrum is here analysed as a preliminary step in choosing appropriate photon energies to perform RXES. The LUMO and LUMO+1 were approximately curve-fit using two Gaussians and a step-function. The dashed lines show the photon energies chosen for RXES, and the solid lines show the boundaries of the photon energy resolution.

Figure 6.15 shows the N 1s RXES spectra taken at the LUMO resonance using $h\nu = 398.85$ eV for monolayers and multilayers of N3 on TiO₂. The monolayer and multilayer valence band photoemission spectra are also shown. The photoemission curves show the full valence band spectra whereas the RXES spectra show only the part of it that is both local to the LUMO, and has ‘*p*’ character so can interact with the 1s core level. Both of the RXES spectra show an elastic peak. This indicates that some of the electrons excited to the LUMO then return to the N 1s core level. This is expected as the LUMO overlaps with the substrate conduction band as discussed in Section 6.3.2, so electrons excited to the LUMO are not expected to delocalise through injection into the substrate.

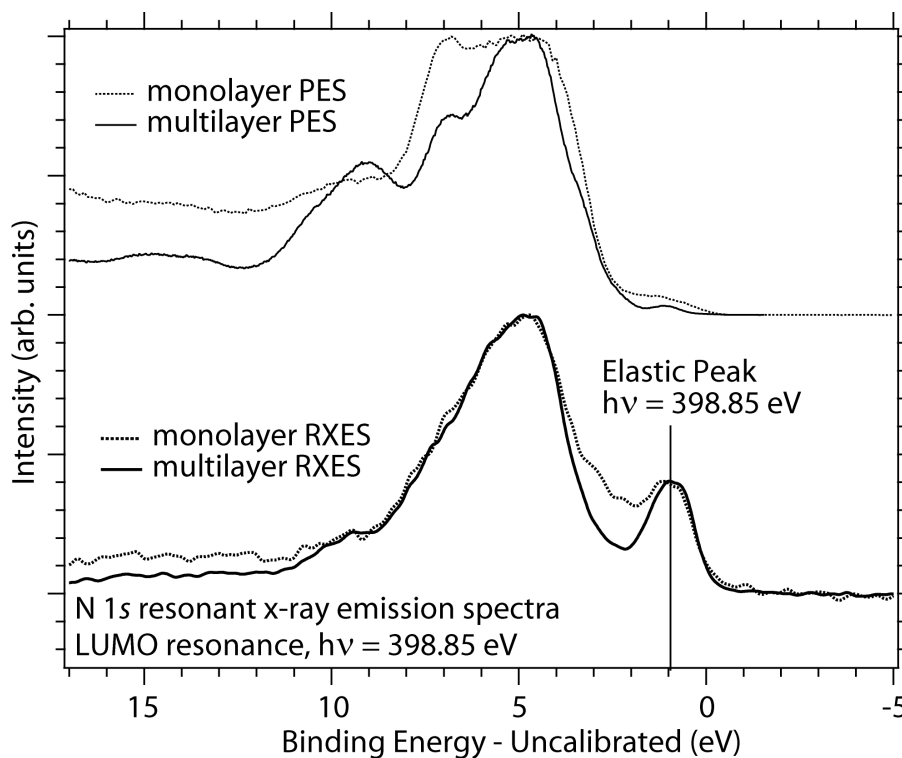


FIGURE 6.15: N 1s resonant x-ray emission spectra taken at the LUMO resonance using $h\nu = 398.85$ eV for monolayers and multilayers of N3 on TiO₂. The monolayer and multilayer valence bands as measured using photoemission spectroscopy are shown for comparison. The RXES spectra are measured on a photon energy scale but have been placed here on a binding energy scale.

Figure 6.16 shows the N 1s RXES spectra taken at the LUMO+1 resonance using $h\nu = 400.15$ eV for monolayers and multilayers of N3 on TiO₂. The monolayer and multilayer valence band photoemission spectra are also shown. While the multilayer has a clear elastic peak, the monolayer does not. There is perhaps a shoulder, but importantly, compared to the multilayer the intensity is reduced. This contrasts to the LUMO RXES spectra where the intensity at the position of the elastic peak is equal at both coverages. The absence of an equally intense elastic peak in the monolayer LUMO+1 spectrum as compared to the multilayer LUMO+1 spectrum qualitatively suggests that electrons are delocalising from the LUMO+1 in the monolayer, on a timescale comparable with the N 1s core hole lifetime (6 fs). The results of the RXES measurements thus imply that electron injection occurs from the LUMO+1. These results also support the bonding geometry conclusion that N3 attaches to rutile TiO₂(110) via one bi-isonicotinic acid ligand and one thiocyanate ligand. The attached thiocyanate ligand provides a direct route for electron injection from the LUMO+1. That a shoulder remains for the monolayer LUMO+1 elastic peak could be because electron injection from the LUMO+1 to the substrate only occurs from those half of the thiocyanate ligands that are attached to the surface.

Figure 6.17 shows RXES spectra taken of the clean TiO₂ surface using $h\nu = 398.85$ eV and $h\nu = 400.15$ eV. These spectra were taken to confirm that the elastic peaks seen in Figures 6.15 and 6.16 are not due to reflection. Since there is no feature to normalise to, they were backgrounded and then normalised by the average of the values divided by for the other RXES spectra, taking into account the smaller time spent counting in this case. In both spectra, an unidentified broad peak is seen with low intensity. The intensity is, however, negligible when compared to the elastic peaks in Figures 6.15 and 6.16. When molecules are deposited onto the clean surface, it is not expected that the reflectivity of the surface would increase for any reason.

6.4 Conclusions

UHV electrospray deposition has been used to deposit monolayers and multilayers of N3 on the rutile TiO₂(110) surface, *in situ*. PES has been used to characterise

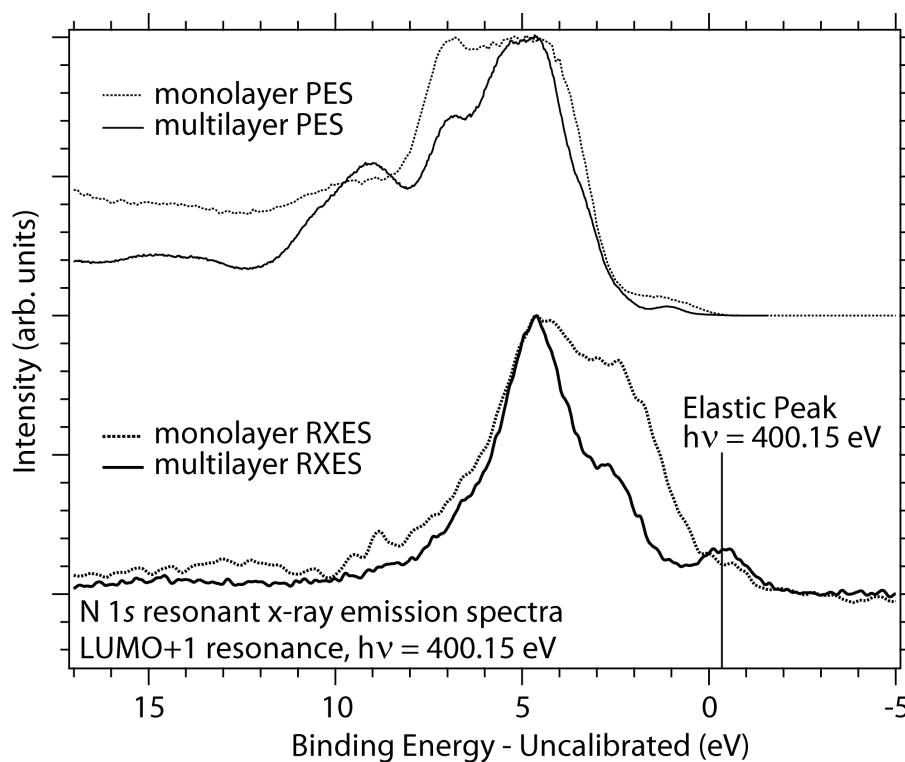


FIGURE 6.16: N 1s resonant x-ray emission spectra taken at the LUMO+1 resonance using $h\nu = 400.15$ eV for monolayers and multilayers of N₃ on TiO₂. The monolayer and multilayer valence bands as measured using photoemission spectroscopy are shown for comparison. The RXES spectra are measured on a photon energy scale but have been placed here on a binding energy scale.

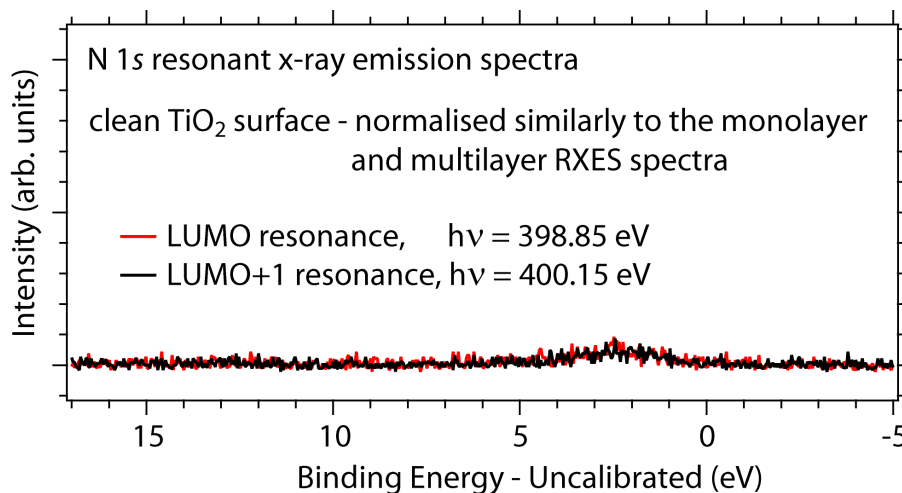


FIGURE 6.17: RXES spectra taken of the clean TiO₂ surface using $h\nu = 398.85$ eV and $h\nu = 400.15$ eV. Since there is no feature to normalise to, they were backgrounded and then normalised by the average of the values divided by for the other RXES spectra, taking into account the smaller time spent counting in this case.

core and valence levels of the system, which were then used to deduce the bonding geometry of a monolayer of N3 chemisorbed to TiO₂(110). We find that the carboxyl groups of one bi-isonicotinic acid ligand deprotonate so that its O atoms bond to Ti atoms of the substrate, and one of the thiocyanate groups bonds via a S atom to an O atom of the substrate. DFT calculations indicate that this geometry is energetically more favourable than the bonding of one carboxyl group from each bi-isonicotinic acid ligand.

The energetic alignment of the system was determined by placing the valence PES and N 1s NEXAFS of an N3 monolayer onto a common binding energy scale. The band gap of the TiO₂ was aligned using valence PES of the clean substrate. The 535 nm optical absorption maximum of N3 on TiO₂ was attributed to the HOMO→LUMO transition in a working solar cell. This was used to compare the energetics as they would appear for photoexcitation from the valence band (as occurs in the working N3 DSC) with those found for photoexcitation from the N 1s core level, for which the unoccupied levels appear at a higher BE. This comparison allowed quantification of the difference in BE of a core and valence exciton for this system, found to be 1.6 eV.

The core-hole clock implementation of RES was used to find that electron injection

from the LUMO+3 to the substrate occurs in < 16 fs, in agreement with previous studies of bi-isonicotinic acid and related molecules on TiO₂ which found charge transfer to occur in < 3 fs. The LUMO and LUMO+3 are both thought to be located on the bi-isonicotinic acid ligands, so electron injection in the real DSC is expected to be on a similar timescale.

In the RES data, resonant photoemission peaks are seen only for certain occupied-unoccupied level combinations due to the spatial distribution of the molecular orbitals, and their overlap with each other and the core-hole site. Combined with DFT calculations we can understand this process for the state-dependent enhancement of the HOMO at the excitation energies of the LUMO and LUMO+1 resonances. The HOMO and LUMO+1 are localised on the central Ru atom and thiocyanate ligands, while the LUMO is localised largely on the bipyridine (π^*) and carboxyl groups.

RXES was used to measure the valence band structure local to the LUMO and to the LUMO+1. Qualitative analysis of the elastic peak feature seen for each spectrum suggests that electron injection occurs from the LUMO+1.

CHAPTER 7

N3 on Au(111)

7.1 Introduction

In this chapter the system of N3 adsorbed on Au(111) is explored. In the previous chapter, work about N3 on TiO₂ was presented with reference in particular to the Grätzel dye-sensitised solar cell. In such a device - where a nanocrystalline film of a wide band gap semiconductor (such as TiO₂) is made light-sensitive by adsorbing a monolayer of dye - electrons in the highest occupied molecular orbital (HOMO) of the dye are promoted to the lowest unoccupied molecular orbital (LUMO) by photoexcitation. In N3 these orbitals are located on the thiocyanate (NCS) and bi-isonicotinic acid ligands, respectively,[95, 82, 65] as illustrated in Figure 6.13. N3 has been shown to bond to the surface of TiO₂ via the deprotonation of the bi-isonicotinic acid ligand[65] to form a so-called 2M-bidentate anchor to the surface. This provides a strong chemical coupling to facilitate the charge transfer of electrons from the LUMO (which is located on this ligand) to the conduction band of the oxide. But this represents only half of the story since the process leaves a hole in the HOMO (located on the NCS ligands) which needs to be replenished. In a typical DSC this is often achieved with a liquid electrolyte but recently a solid state solution to this problem was proposed by adsorbing the dye molecules onto a gold layer itself adsorbed on the TiO₂ surface;[24, 25] this device is discussed in Section 1.4. The exact nature of how the solid state device works is still under investigation. One theory is that the Au forms islands and/or networks on the TiO₂, rather than forming a uniform thickness

barrier layer as originally proposed. This would allow the dye molecules to interact simultaneously with the Au islands and/or networks and the TiO₂ surface. In dyes such as N3 where the spatial distribution of the HOMO and LUMO are separated onto different ligands of the molecules, a gold layer could offer a route to the efficient replenishment of electrons.

Previous studies on N3 (see previous chapter), the N3 ligand bi-isonicotinic acid,[15, 89] and other pyridine carboxylic acids[78, 79, 80] on TiO₂ have all been shown to bond to the surface via the oxygen atoms of the deprotonated carboxyl groups. On the Au(111) surface however, bi-isonicotinic acid bonds less strongly than on TiO₂, possibly via one or more carboxyl groups, but certainly without any deprotonation.[85, 86] It is therefore reasonable to expect that N3 would bond to the Au(111) surface instead via the sulphur atoms of the thiocyanate ligands (NCS). Indeed, the interaction of sulphur-containing molecules with the gold surface is well established[96, 97] and underpins much of the field of self-assembled monolayers. Such an adsorption geometry would place the molecule HOMO adjacent to the Au(111) surface and in the context of DSCs would be ideally located for electron replenishment.

This work represents the first study of N3 adsorbed on the Au(111) surface. Using an *in situ* UHV electro spray deposition system, as described in Chapter 5, we can form low and high coverages of the dye on the Au(111) surface. In this chapter the geometric and electronic structure of N3 on Au(111) is studied using photoemission spectroscopy (PES), near-edge x-ray absorption fine structure (NEXAFS) spectroscopy, and scanning tunnelling microscopy (STM). The charge transfer between the molecule and substrate is investigated using resonant electron spectroscopy (RES). These techniques enable us to probe the occupied and unoccupied states of the system in relation to the substrate conduction band.

7.2 Method

Photoemission spectroscopy experiments were carried out at the surface science undulator beamline I511-1[38] at MAX II, MAX-lab in Lund. The I511-1 end station is equipped with a Scienta R4000 electron analyser which was orientated in-line with

the light polarisation vector \mathbf{E} . The sample was orientated near to normal emission, which corresponds to 7° off normal due to the grazing incidence geometry of the sample holder.

The photoemission measurements were performed using a single crystal Au(111) substrate of dimensions 10 mm diameter \times 2.5 mm (Metal Crystals and Oxides Ltd., UK). A loop of tungsten wire was passed through the crystal, which acted as a mount and also served to heat the crystal. A thermocouple wire was attached within a small cavity in the crystal, used to monitor the temperature. Cycles of sputtering using 1 keV Ar ions, and annealing to $\sim 600^\circ\text{C}$, were used to prepare the surface. The substrate was deemed clean when it showed a negligible C 1s core-level signal.

The N3 molecule (Solaronix SA, Switzerland) was deposited by *in situ* UHV electrospray deposition, from a solution of ~ 5 mg of N3 in 200 ml of a 3(methanol):1(water) mixture. The deposition of N3 using this method is described in Section 6.2 of the previous chapter.

For the electron spectroscopy data, the total instrument resolution ranges from 65-195 meV. All spectra have been calibrated to the Fermi level. For the core levels, depending on the shape of the background and magnitude of the Shirley step background, a line or polynomial background was subtracted if needed before subtracting a Shirley background if necessary. Curve fitting was then performed using Gaussian functions. For all measurements, the sample was swept continuously at a rate of at least $1.25 \mu\text{m/s}$, following beam damage studies to determine a safe exposure time.

The STM measurements were performed at Nottingham using a 4 mm \times 8 mm mica substrate covered with a layer of Au 1500 Å thick (Agilent, USA). The sample was prepared by sputtering using 1 keV Ar ions, and annealing to $\sim 500^\circ\text{C}$. Images of the surface were acquired using a scanning tunnelling microscope housed within a UHV system, using electrochemically etched tungsten tips, and operating in constant current mode at room temperature.[98] Images of the surface taken after the sputter-anneal cycle show the characteristic $(22 \times \sqrt{3})$ herringbone reconstruction of the Au(111) surface.[99] The N3 was then deposited onto the surface using the same UHV electrospray deposition method as above.

7.3 Results

Photoemission spectra were recorded for low and high coverages of N3 on Au(111), corresponding to deposition times of 15 and 30 mins, respectively. Coverage is not necessarily linear with deposition time, as the electrospray process depends on many factors such that the deposition rate changes over the course of minutes. In the previous chapter where the sample was N3 on TiO₂, the coverage could be quantified more accurately by comparing the O 1s molecule and substrate peak heights, and also by observing the S 2p spectra which showed a clear change as coverage was increased. Here the best photoemission indicator of coverage is the valence band. Figure 7.1 shows the valence band photoelectron spectra of the clean Au surface and the low and high coverages of N3, measured using $h\nu = 110$ eV. It can be seen that the low coverage valence band shape is only slightly modified with respect to the valence band for clean Au. The high N3 coverage, however, has a very different shape in which the Au peaks are largely buried by the N3 molecule peaks.

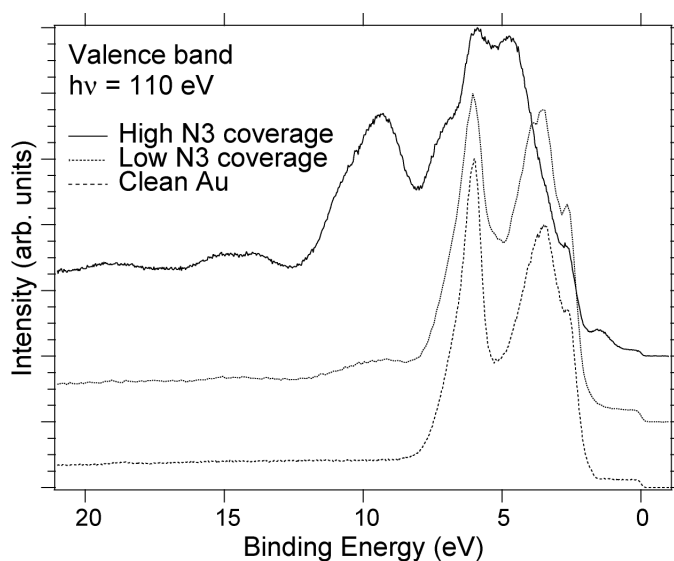


FIGURE 7.1: Valence band photoemission spectra of clean Au, and of low and high coverages of N3 on Au, measured using $h\nu = 110$ eV. Total instrument resolution was < 65 meV.

7.3.1 Adsorption

Binding energies (BEs) of the x-ray photoemission spectroscopy (XPS) peaks discussed hereafter are summarised in Table 7.1. Figure 7.2 shows the O 1s photoelectron spectra of the low and high coverages, measured using $h\nu = 620$ eV. Both coverages show two separate peaks at 531.4 and 533.1 eV. These are due to the O being in two different chemical environments, which are identified as the carbonyl (C=O) and hydroxyl (C—OH) groups respectively.[15] The hydroxyl oxygen does not deprotonate at low coverages, as evidenced by the unity peak ratio. This is in contrast to the adsorption of N3 on TiO₂,[65] which shows a 3:1 peak ratio due to deprotonation of two of the carboxyl groups. The O atoms may interact with the substrate but do not form strong covalent bonds as in the case of deprotonated O atoms.

TABLE 7.1: Table of BEs and [Gaussian full-width at half-maxima] (eV), calibrated to the Fermi level.

Core level	Peak BEs and [Gaussian FWHM]					
	(eV)					
O 1s both coverages	531.4 [1.7]	533.1 [1.9]
S 2p low coverage	161.0 [0.5]	162.1 [1.3]	164.3 [1.4]
S 2p high coverage	161.0 [0.5]	162.1 [1.1]	164.3 [1.4]
N 1s both coverages	396.9 [1.0]	398.0 [0.9]	399.9 [0.9]
C 1s & Ru 3d low coverage	280.9 [0.7]	284.8 [1.1]	285.8 [1.1]	287.0 [1.5]	288.6 [2.2]	
C 1s & Ru 3d high coverage	280.8 [0.7]	284.9 [1.1]	285.7 [1.1]	286.8 [1.5]	288.6 [2.2]	

Figure 7.3 shows the S 2p photoelectron spectra of the low and high coverages, measured using $h\nu = 220$ eV. S 2p is a doublet state and here the best fits have been obtained using a spin-orbit split of 1.18 eV. Both coverages require three doublets in order to obtain a good curve-fit. The doublets are assigned to bonding environments by comparing the high and low coverage spectra, comparing normal and grazing emission spectra of the low coverage, and comparison with studies of N3 on TiO₂,[65] and of atomic S on Au(111).[100]

The low BE doublet at 161.0 eV is significantly more intense for the low coverage, so is attributed to a surface S-Au interaction. The peaks comprising the doublet are narrow with a full-width at half-maximum (FWHM) of 0.5 eV, implying a well-defined

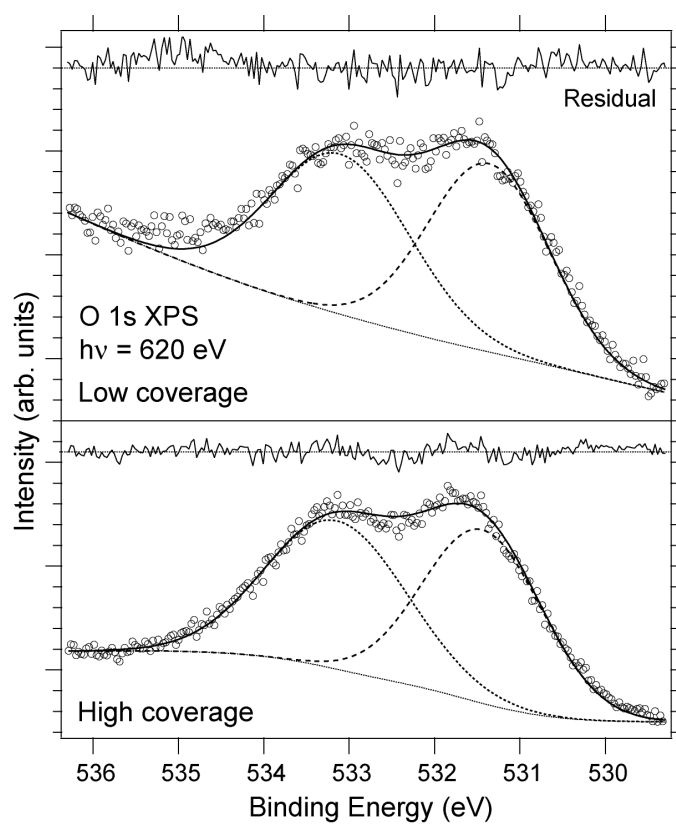


FIGURE 7.2: O 1s core-level photoemission spectra measured using $h\nu = 620$ eV. Total instrument resolution was < 195 meV.

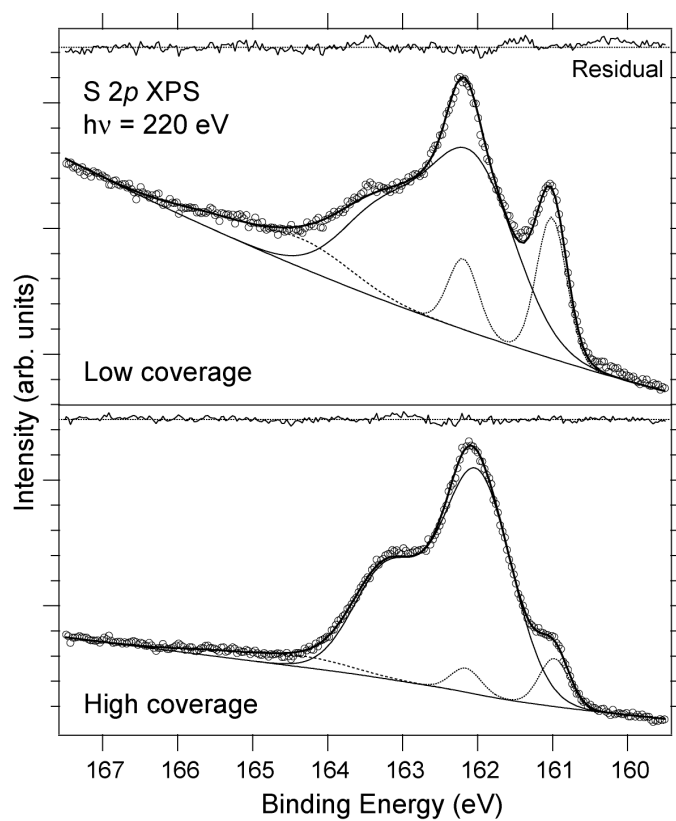


FIGURE 7.3: S 2p core-level photoemission spectra measured using $h\nu = 220$ eV. Total instrument resolution was < 75 meV.

chemical environment. In studies of atomic S on Au(111),[100] a low BE doublet is seen at 160.8 eV which, supported by low-energy electron diffraction studies, is attributed to S bonding to threefold hollow sites of the Au(111) surface. (BEs are referenced, as here, to the Fermi level.) Since this BE is very close to that of the S-Au doublet found here at 161.0 eV, and taking into account the coverage dependence, the doublet is assigned to being due to a S-Au bond. It could also be specific to Au(111) threefold hollow sites but further experimental investigation would be needed to confirm this.

The middle BE doublet at 162.1 eV dominates the high coverage spectrum and is also large in the low coverage spectrum. In both coverages the doublet is broad, with FWHMs of 1.1 and 1.3 eV for high and low coverages, respectively. These large widths imply more than one S chemical environment which have similar but unresolvable BEs. That the middle BE doublet is dominant for both low and high coverage can be accounted for if it contains a component of both non-bonded S and S bonded to Au. For atomic S on Au(111) there is a doublet at 161.6 eV corresponding to S atoms bound to Au(111) sites other than three-fold hollow,[100] so it is possible that here the middle BE doublet has a similar bonded component. For N₃ on TiO₂,[65] non-bonded S was found to have a BE of 161.7 eV, and the same BE would be expected here. With this peak assignment, at high coverage the middle BE doublet is expected to be mostly due to non-bonded atoms, and at low coverage a mixture of non-bonded and bonded atoms. If these components were at slightly different BEs, this would result in the low coverage having a broader FWHM than the high coverage, which is the case here. This assignment of peaks is also supported by comparison of normal and grazing emission spectra described below.

Finally, there is a high BE doublet at 164.3 eV, which is also broad with a FWHM of 1.4 eV. The intensity of this peak is small, so only a small minority of the S atoms are present in this state. The intensity is larger at low coverage than high coverage so it is thought to be due to a surface interaction. For atomic S on Au(111), there is a high BE doublet at 163.4 eV which at low coverage corresponds to S₂ species. It is possible that here, S atoms from different N₃ molecules bond together at the Au surface. This is not unusual in the context of some alkylthiols on Au(111) which form

S headgroup dimers at the surface.[97] Due to the geometry of the N3 molecule, we would not expect this process to occur very often on the surface, in agreement with the low intensity of this peak.

Figure 7.4 shows normal emission (NE) and grazing emission (GE) S 2*p* photoelectron spectra of the low N3 coverage, measured using $h\nu = 220$ eV. Here NE and GE correspond to electron take-off angles of 90° and 20° respectively, relative to the surface plane. At NE the low BE doublet is more intense than at GE, confirming that it is due to a surface interaction. The middle BE doublet has a relatively higher intensity at GE, confirming that it has a non-bonded component.

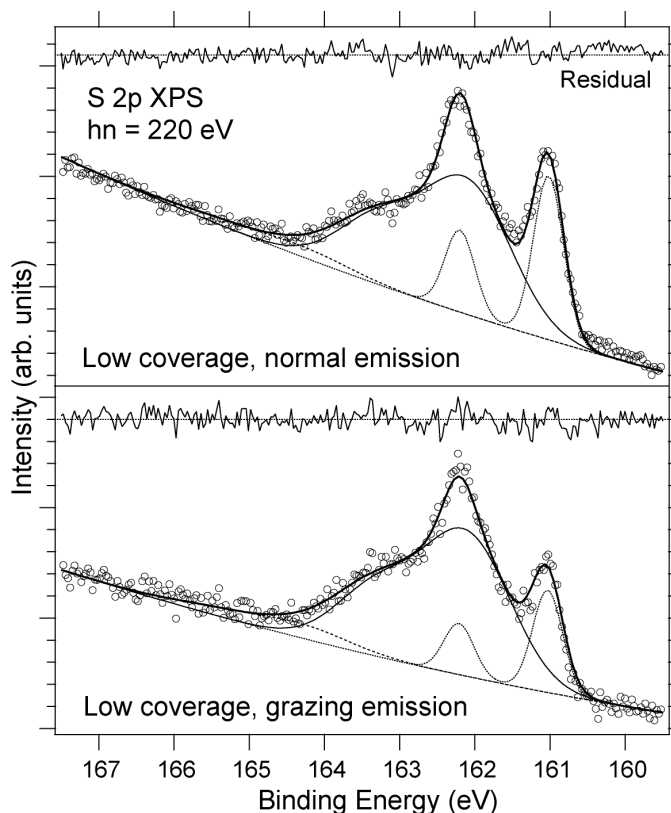


FIGURE 7.4: S 2*p* core-level photoemission spectra comparing normal and grazing emission, measured using $h\nu = 220$ eV. Total instrument resolution was < 125 meV.

Figure 7.5 shows the N 1*s* photoelectron spectra of the low and high coverages, measured using $h\nu = 500$ eV. In N3 there are 2 N atoms in the bi-isonicotinic acid ligands for every 1 in the thiocyanate ligands. The intense, high BE peak at 399.9

eV is more than twice the intensity of the other two peaks together, and is identified as the bi-isonicotinic acid N. The lower two BE peaks at 398.0 and 396.9 eV are thus attributed to the thiocyanate N. A study of N₃ on TiO₂ showed the highest two of these three peaks, at similar energies of 399.8 and 397.8 eV.[65] The additional low BE thiocyanate shoulder found in this case is attributed to thiocyanate N that has been shifted to lower BE due to strong chemical bonding of that thiocyanate ligand to the Au surface via the S atom. The ratios of the peaks in the S 2*p* and N 1*s* low coverage spectra support this: in the low coverage S 2*p* spectrum, the low BE doublet attributed to a strong S-Au bond comprises 20.4% of the total measured intensity, and in the low coverage N 1*s* spectrum, the low BE peak represents 22.2% of the intensity from the thiocyanate N atoms.

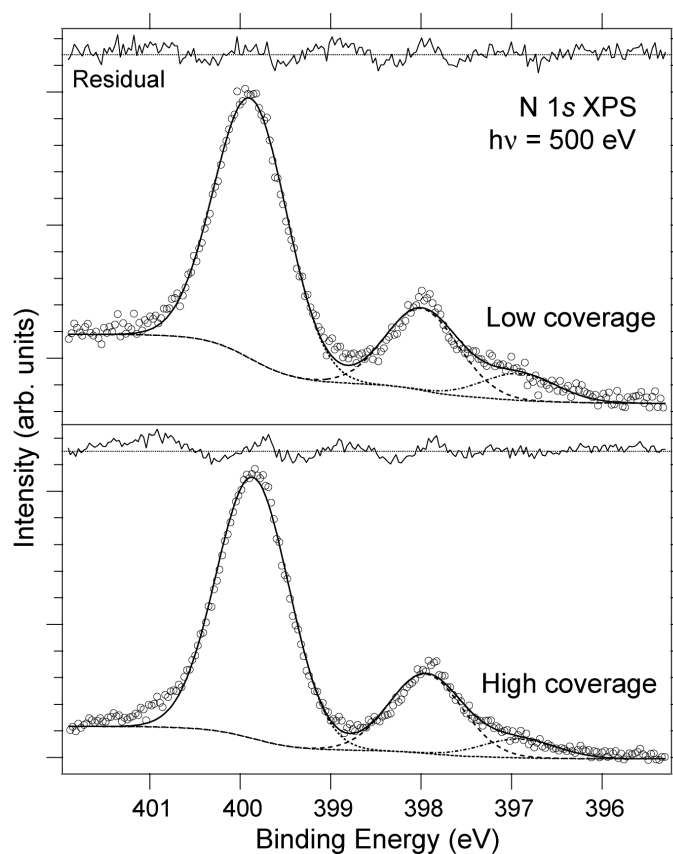


FIGURE 7.5: N 1*s* core-level photoemission spectra measured using $h\nu = 500$ eV. Total instrument resolution was < 145 meV.

Figure 7.6 shows the C 1s and Ru 3d photoelectron spectra of the low and high coverages, measured using $h\nu = 380$ eV. The peak at 280.8 eV is Ru $3d_{5/2}$, with the corresponding Ru $3d_{3/2}$ part of the doublet being hidden 4.2 eV higher[84] among the C 1s peaks. The remaining C 1s spectra have been curve-fit using four peaks. Since the spectra are complicated, the FWHM of each peak has been constrained to be the same at low and high coverage, resulting in the fits shown. The pyridine and carboxyl peaks are recognisable from previous studies of bi-isonicotinic acid on Au/TiO₂. [86]

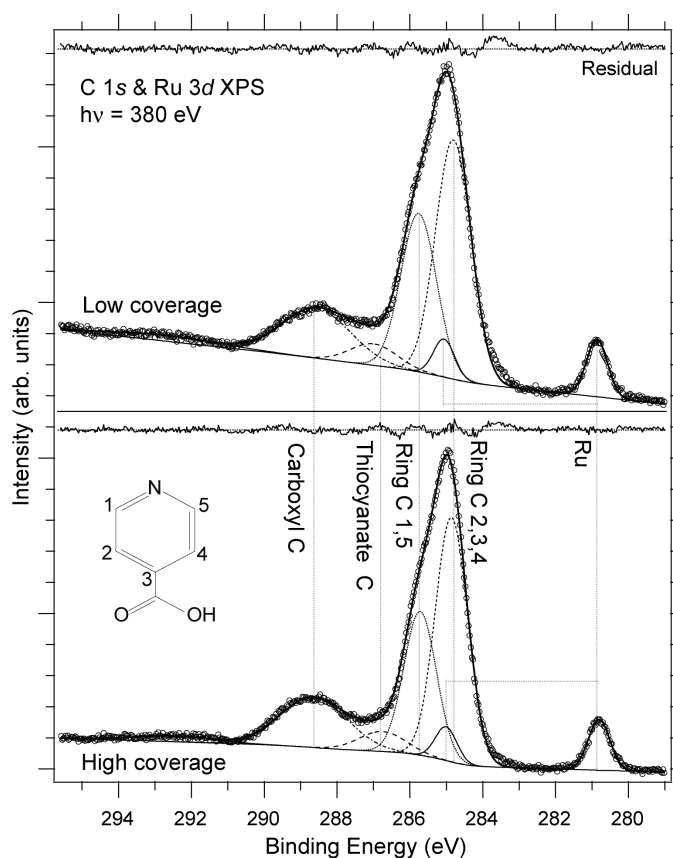


FIGURE 7.6: C 1s core-level photoemission spectra measured using $h\nu = 380$ eV. Total instrument resolution was < 110 meV.

The most intense peak in the spectrum at ~ 285 eV is mainly due to C atoms in the pyridine ring. Here we can resolve those ring C atoms that neighbour a N atom (atoms 1 and 5 in Figure 7.6) and those which do not (atoms 2, 3 and 4). These components were additionally constrained to have the same FWHM, placing them at

BEs of 285.8 and 284.8 eV respectively. This resolution of two peak components for pyridine ring C was found previously using angle-resolved XPS of isonicotinic acid on TiO₂,^[75] which allowed identification of the two peaks here.

The peak at 288.6 eV is due to carboxyl C atoms, and the remaining peak at 286.9 eV due to thiocyanate C atoms. Based on the stoichiometry of the N₃ molecule, the ratio of (2,3,4)pyridine:(1,5)pyridine:carboxyl:thiocyanate C atoms for N₃ is 6:4:2:1. Here the ratios found were 6.0:4.0:2.4:0.7 and 6.0:4.0:2.5:0.7 for the low and high coverages, respectively. The feature at ~ 292 eV is thought to be a shake-up.

Figure 7.7 shows the STM images of N₃ deposited onto the mica-supported Au(111) surface. Large area scans of the surface with low molecular coverage, such as the example shown in Figure 7.7 (a), reveal that N₃ adsorbs preferentially to produce a herringbone pattern mimicking that of the underlying substrate reconstruction. The characteristic Au(111) herringbone reconstruction^[99] is easily identifiable in STM and consists of pairs of bright lines which bend through 120° and follow the $[11\bar{2}]$ crystallographic axis of the surface. The adsorbed molecules reproduce the morphological features of the herringbone reconstruction with a broad row of molecules being imaged in place of the two bright lines normally observed. As the coverage is increased up to a full monolayer the bare Au regions between the lines are filled in to produce a molecular overlayer with no discernable long range order (shown in Figure 7.7 (b)). The lack of three-dimensional island growth during the submonolayer to monolayer growth regime indicates that the molecule-substrate interaction (mediated by the S-Au interaction) dominates over the molecule-molecule interaction, and that molecules impinging upon the surface are free to diffuse. Figure 7.7 (c) shows a region of low coverage, where the section enclosed by the marked rectangle has been analysed in Figure 7.7 (d), showing the mean of the line profiles taken widthwise across the rectangle. The expected periodicity of the herringbone reconstruction has been superimposed upon the averaged line profile demonstrating a good agreement with the observed position of the molecular rows and confirming their similar periodicity. Measurement of the apparent height of the periodic features facilitates the discrimination between clean Au(111) and low coverage regions of the surface. The undulation of the herringbone is 0.2 Å, an order of magnitude smaller than that of

the adsorbed molecules, making it possible to determine that the region shown in image 7.7 (a) contains adsorbed molecules ordered by the Au(111) reconstruction.

The XPS and STM data, together describe how N₃ adsorbs to the Au(111) surface. The XPS spectra show that N₃ bonds to Au via the S atoms of the thiocyanate ligands, most likely accompanied by a physisorption interaction from the bi-isonicotinic acid ligands. The different components in the S 2*p* spectra imply that S atoms bond to at least two types of Au(111) adsorption site, and that they may also bond to S atoms of neighbouring N₃ molecules at the Au surface. STM images indicate that the N₃ molecules adsorb preferentially to the maxima of the Au(111) herringbone reconstruction. These are areas of high electron density, so it is perhaps unsurprising that S atoms interact most strongly here.

Previous experiments have shown that the HOMO of N₃ is located on the thiocyanate ligands.[95, 82, 65] For N₃ adsorbed on Au then, this places the HOMO of N₃ on the part of the molecule chemically bound to the Au surface. Thus, in a solid state DSC the HOMO would be ideally located to receive electrons from the Au, replacing those electrons lost through the HOMO-LUMO photoexcitation and subsequent charge injection into the TiO₂. Additionally, in a DSC where the Au atoms form islands/networks on the TiO₂ surface, N₃ molecules could also bond to the TiO₂ via at least one bi-isonicotinic acid ligand,[70, 65] ideally placing the LUMO for electron injection.

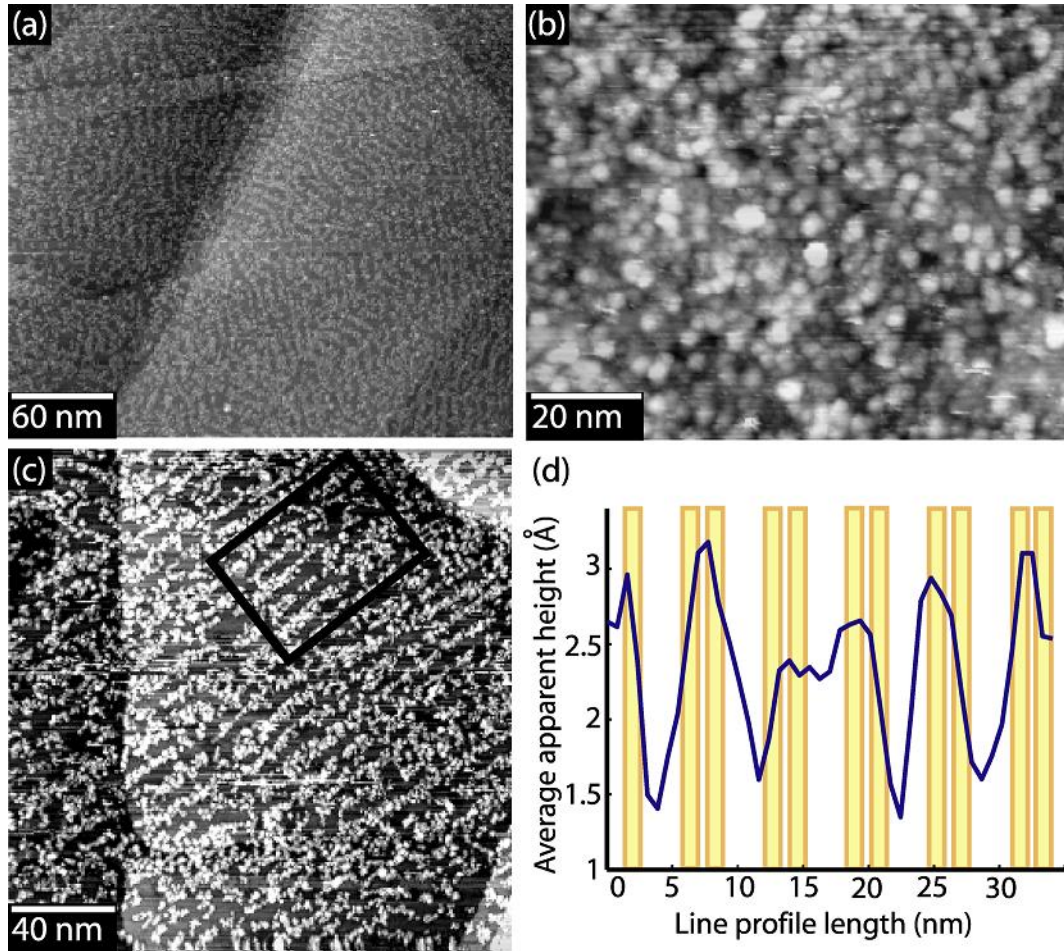


FIGURE 7.7: STM images of N3 deposited onto the mica-supported Au(111) reconstruction. (a) Sub-monolayer N3 coverage ($V_{sample} = +2.50$ V, $I_{tunnel} = 0.03$ nA, 300 nm \times 258 nm); (b) monolayer N3 coverage ($V_{sample} = +2.50$ V, $I_{tunnel} = 0.03$ nA, 100 nm \times 79 nm); (c) sub-monolayer N3 coverage ($V_{sample} = +2.50$ V, $I_{tunnel} = 0.03$ nA, 200 nm \times 200 nm), indicating an area for which the average height profile is shown in (d). The maxima of the Au(111) herringbone reconstruction undulations are also shown superimposed on (d).

7.3.2 Energy level alignment

Figure 7.8 illustrates those occupied and unoccupied states near the Fermi level of the Au and of the low N₃ coverage. The N 1s NEXAFS and valence PES spectra for the low N₃ coverage are shown, along with the clean Au valence PES (measured at $h\nu = 110$ eV). The Au conduction band is also shown schematically. The valence PES spectrum for the high N₃ coverage is also shown as this illustrates the position of the HOMO well. The pyridine N was used to place the NEXAFS on the common BE scale, using the process described in Section 4.2. While peaks derived from the bi-isonicotinic acid N atoms are then located energetically in the right place, any peaks deriving from thiocyanate N will appear artificially shifted by approximately 2 eV to higher BE. In the previous chapter, the LUMO, LUMO+2 and LUMO+3 were identified as being located on the bi-isonicotinic acid ligands, and the LUMO+1 on the thiocyanate ligands, and that identification also applies here.

The figure shows where the occupied and unoccupied levels of the molecule and the Au are, energetically, with respect to each other, enabling identification of the charge transfer processes that can occur within this system.[85, 86, 87, 88] The PES peak at 1.4 eV is the highest occupied molecular orbital (HOMO). In order for the Au to replenish electrons to N₃ HOMO holes, the HOMO must overlap with energy levels in the Au that are occupied with electrons. It is trivial to note that since Au is a conductor, the N₃ HOMO overlaps with the Au valence band (which is occupied with electrons). The Au is thus energetically aligned with N₃ in a way that it can replenish electrons that have transferred out of the N₃ molecule.

The spatial distribution of the N₃ HOMO, as shown in Figure 6.13, is on the thiocyanate ligands and the central Ru atom. Following the analysis in the previous section which showed that N₃ bonds to Au through S atoms, this means that the thiocyanate ligand is ideally located in order to replenish electrons directly from the Au surface to which it is bonded.

The nature of the NEXAFS technique means that a core hole is created, rather than a valence hole as occurs following photoexcitation in a real DSC. This causes the unoccupied levels shown in Figure 7.8 to shift to higher BE than they would

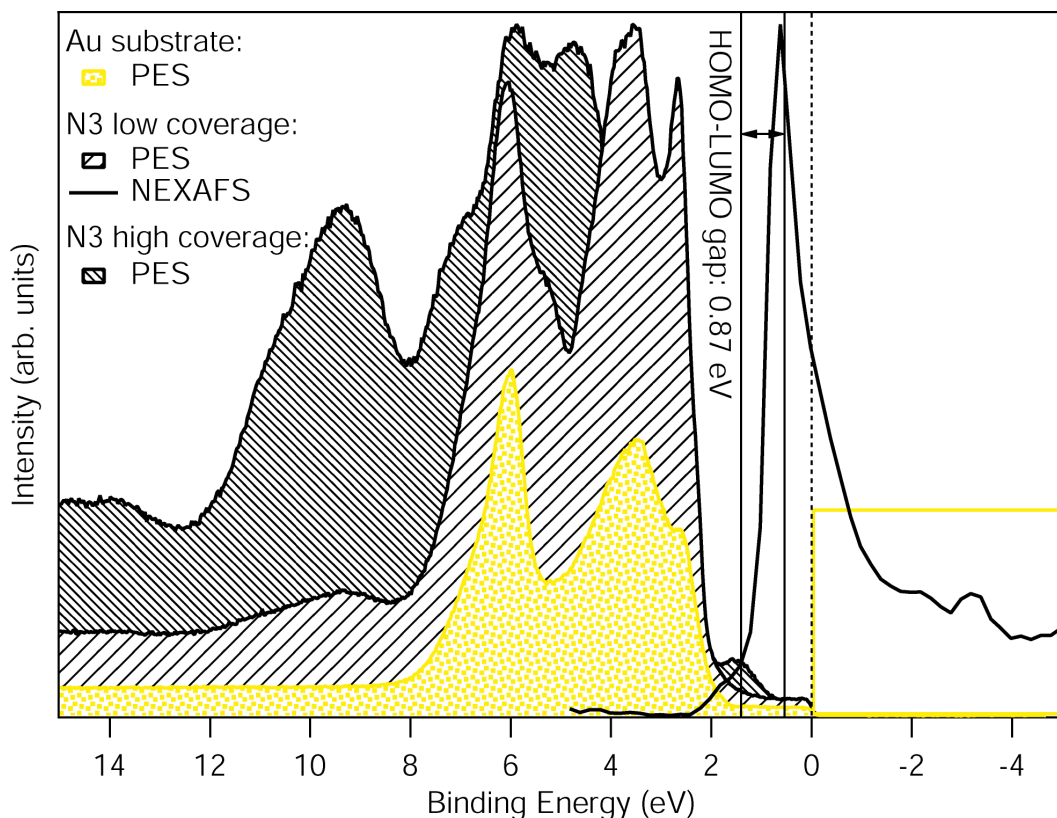


FIGURE 7.8: Valence band PES spectra of the clean Au substrate, a low coverage of N3 and a high coverage of N3, adjacent to a N $1s$ NEXAFS spectrum of the low N3 coverage. Also the Au conduction band is shown schematically. The HOMO-LUMO gap of 0.9 eV is indicated. The position of the HOMO was determined by curve-fitting following a polynomial background subtraction. The PES spectra were measured using $h\nu = 110$ eV and had a total instrument resolution of < 65 meV. The NEXAFS spectrum was taken over the photon energy range $h\nu = 397$ -406 eV and had a photon energy resolution of < 100 meV.

otherwise be in the real DSC. In Section 6.3.2, the magnitude of this shift for N₃ was shown to be 1.6 ± 0.1 eV.

7.3.3 Charge transfer

Using resonant electron spectroscopy (RES), one can probe the charge transfer between the substrate conduction band and any unoccupied adsorbate levels that overlap energetically with this. In the case of N₃ on Au, the particular charge transfer route of interest is that from the Au valence band to the molecule HOMO. The RES technique can only be used to observe charge transfer from an energy level that is *usually* unoccupied; since the HOMO is usually *occupied*, the technique cannot be applied to observe charge transfer between these specific levels.

However, charge transfer between *any* molecule level and the Au surface would have to travel through the molecule's thiocyanate ligand (unless the charge tunneled from another unbonded part of the molecule to the surface). Observations of charge transfer via the thiocyanate ligands, from any levels, would give an indication of the coupling strength between the ligand and the surface. Here then are presented RES and NEXAFS spectra, the aim being to observe charge transfer between *any* of the molecule levels and the Au surface.

Figure 7.9 shows the N 1s NEXAFS and RES spectra for the low coverage of N₃ on Au and for a multilayer of N₃. RES is discussed in Section 4.3. The multilayer RES spectrum has been integrated over a 0.6-8.6 eV BE window, and the low coverage over a 4.0-14.0 eV BE (uncalibrated) window; these include only photoemission and resonant photoemission over the LUMO+2 and LUMO+3 levels. Any peaks at the LUMO+2 or LUMO+3 are due solely to resonant photoemission, as direct photoemission contributes a sloping background only. The RES spectra are normalised to the LUMO, the relative intensity of which is not expected to change with coverage since it overlaps energetically with the Au valence band and thus does not have empty states to transfer electrons to. The NEXAFS spectra are also normalised to the LUMO. In the NEXAFS spectra, the peaks represent the unoccupied levels' full intensities, whereas for RES, the LUMO has its full intensity but the LUMO+1,

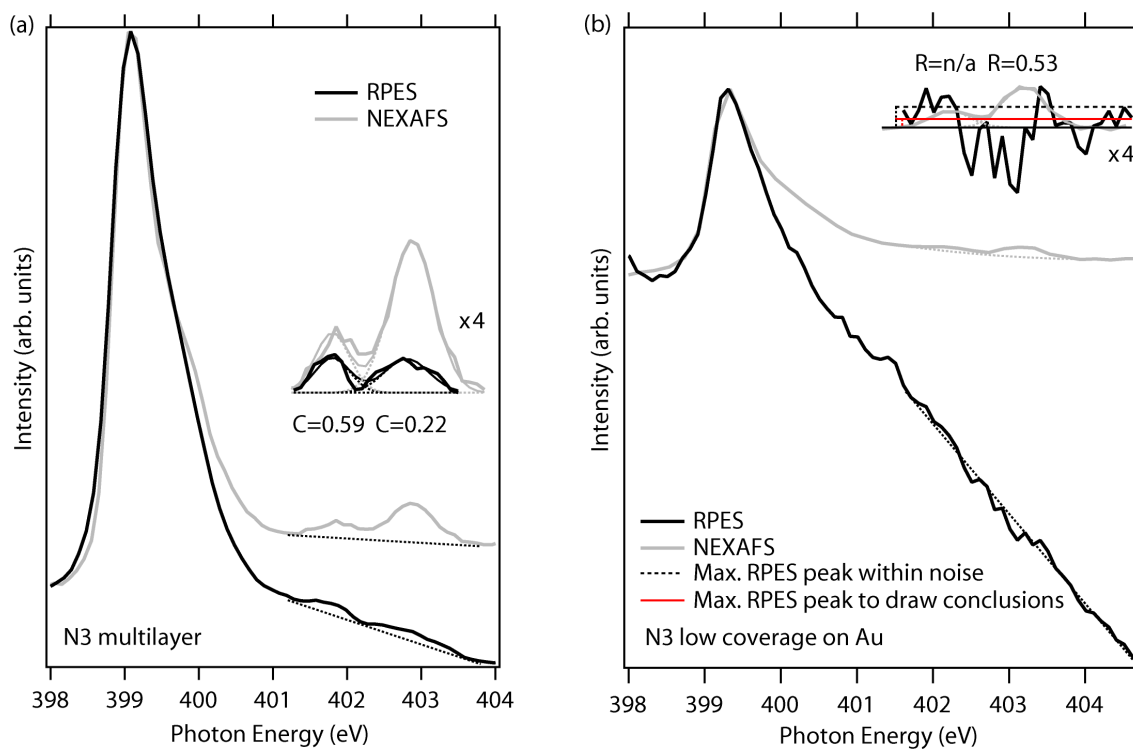


FIGURE 7.9: N $1s$ RES and N $1s$ NEXAFS spectra of the N3 (a) multilayer on TiO₂ and (b) low coverage on Au. The multilayer RES spectrum shown here has been integrated over a 0.6-8.6 eV BE range, and the low coverage over a 4.0-14.0 eV BE (uncalibrated) range, so that peaks at the LUMO+2 or LUMO+3 are due solely to resonant photoemission. Also shown are 4 \times magnifications of the LUMO+2 and LUMO+3 region. The values C and R represent the RPES:NEXAFS intensity ratios of the peaks shown. The dashed black line in (b) indicates an estimate of the largest magnified LUMO+3 peak that could be hidden within this level of noise. The red line indicates the intensity below which the peak would have to be confidently fit in order to ascertain whether there is charge transfer between the LUMO+3 and the Au. Photon energy resolution of the NEXAFS and RES spectra was < 170 meV.

LUMO+2 and LUMO+3 may be depleted by charge transfer. Even for the multilayer though, where no charge transfer can occur, the resonant photoemission peaks are smaller than the NEXAFS peaks corresponding to the same unoccupied levels. This is attributed purely to matrix element effects due to the different techniques used.[86]

In Figure 7.9 (a) the data is taken from the N3 on TiO₂ multilayer since this spectrum had better statistics than the high coverage N3 on Au RES spectra that were taken. For a multilayer, it should not matter what surface the molecule is on. In Figure 7.9 (b), the RES spectrum, which represents a total measuring time of five hours, has too much noise to confirm the intensities at the LUMO+2 and LUMO+3 energies. In order to say whether there is any charge transfer occurring, the ratio of the RPES:NEXAFS peaks for the low coverage must be smaller than that for the multilayer, which for the LUMO+3 is 0.22. Since the NEXAFS peak at the LUMO+3 has good signal-to-noise, its intensity can be measured to good precision, and used with the 0.22 ratio to determine that the LUMO+3 RPES peak would need to be smaller than the height indicated by the red line shown on the figure, in order to confirm the occurrence of charge transfer. Since the noise is large, it cannot be said with confidence that a hidden LUMO+3 peak would be the height of the red line or smaller, and so in this case an estimate is not made for the timescale of charge transfer.

7.4 Conclusions

The adsorption of the dye molecule N3 on the Au(111) surface, using UHV electro-spray deposition, has been studied using PES and STM. The PES data, in particular the S 2*p* spectra, have been interpreted to conclude that N3 bonds to Au(111) via S atoms, and adsorbs preferentially at the faulted regions of the Au(111) herringbone reconstruction. Approximately 20% of the S atoms form a particularly strong bond, possibly to the three-fold hollow sites of the Au surface.

The energy level alignment of N3 with the Au(111) surface has been constructed using PES and NEXAFS spectroscopy, illustrating the overlap between the N3 HOMO and the Au valence band. The HOMO, which becomes the site of a hole following

photoexcitation in a DSC, is located on the thiocyanate ligands which are here shown to bond via S atoms to the Au surface.

This study is fundamental to understanding the use of N₃ in a solid state DSC that uses a metallic electrode such as Au to replenish electrons lost by the dye.

CHAPTER 8

Summary

In order to understand the behaviour of a large and complicated system such as a dye-sensitised solar cell (DSC), it is often helpful to isolate one small part of the system, simplify it, and study this less complex system. In this thesis two model systems were studied, each consisting of molecules on a surface. The dye molecule N3 was studied on the rutile $\text{TiO}_2(110)$ and $\text{Au}(111)$ surfaces. The former models a solar cell that is currently the most efficient of its kind and the latter models a potential solar cell technology that has not yet been developed. These are put in context in Chapter 1.

In both cases, the dye molecules were deposited onto the surfaces using a newly-developed ultra-high vacuum (UHV) electrospray deposition system. Large and fragile molecules such as N3 cannot be deposited using the typical method of thermal sublimation, so development of the electrospray deposition system was a necessary step in studying these systems in an ultra-high vacuum environment right from the deposition stage. The electrospray deposition system enables a coverage-controlled *in situ* deposition of molecules onto a surface in UHV and is explained in detail in chapter 5.

Once prepared, the samples were studied using mainly electron and photon spectroscopic methods at synchrotrons. Chapter 2 gives an overview of synchrotrons and how they work. Other techniques performed include scanning tunnelling microscopy (STM) and density functional theory (DFT) which were carried out at Nottingham. Both systems were studied using techniques to find out about the adsorption of

molecules to surfaces, as described in Chapter 3, and the charge transfer between molecules and surfaces, as described in Chapter 4.

The results for N3 on $\text{TiO}_2(110)$ are presented in Chapter 6. The core-level photoemission spectra revealed that N3 bonds to rutile $\text{TiO}_2(110)$ by deprotonation of the carboxyl groups of one bi-isonicotinic acid ligand so that its oxygen atoms bond to titanium atoms of the substrate, and one of the thiocyanate groups bonds via a sulphur atom to an oxygen atom of the substrate. Supporting DFT calculations indicate that this geometry is energetically more favourable than the bonding of one carboxyl group from each bi-isonicotinic acid ligand. RXES was used to measure the valence band structure local to the LUMO and to the LUMO+1.

Valence band photoemission and N $1s$ x-ray absorption spectra of N3 on $\text{TiO}_2(110)$ were aligned on a common binding energy scale to enable a quantitative analysis of the bandgap region. A consideration of the energetics in relation to optical absorption was used to identify the main photoexcitation channel between the highest occupied and lowest unoccupied molecular orbitals in this system. The 535 nm optical absorption maximum of N3 on TiO_2 was attributed to the HOMO \rightarrow LUMO transition in a working solar cell. This was used to compare the energetics as they would appear for photoexcitation from the valence band (as occurs in the working N3 DSC) with those found for photoexcitation from the N $1s$ core level, for which the unoccupied levels appear at a higher BE. This comparison allowed quantification of the difference in BE of a core and valence exciton for this system, found to be 1.6 eV.

The charge transfer between N3 and $\text{TiO}_2(110)$ was studied using resonant photoemission spectroscopy and resonant x-ray emission spectroscopy. The core-hole clock implementation of RES was used to find that electron injection from the LUMO+3 to the substrate occurs in < 16 fs, in agreement with previous studies of bi-isonicotinic acid and related molecules on TiO_2 which found charge transfer to occur in < 3 fs. The LUMO and LUMO+3 are both thought to be located on the bi-isonicotinic acid ligands, so electron injection in the real DSC is expected to be on a similar timescale. In the RES data, resonant photoemission peaks were seen only for certain occupied-unoccupied level combinations due to the spatial distribution of the molecular orbitals, and their overlap with each other and the core-hole site. Com-

bined with DFT calculations we can understand this process for the state-dependent enhancement of the HOMO at the excitation energies of the LUMO and LUMO+1 resonances. The HOMO and LUMO+1 are localised on the central Ru atom and thiocyanate ligands, while the LUMO is localised largely on the bipyridine (π^*) and carboxyl groups. Qualitative analysis of the elastic peak feature found in the RXES spectra suggested that electron injection occurs from the LUMO+1.

The results for N3 on Au(111) are presented in Chapter 7. The core-level photoemission spectra showed that N3 bonds to Au(111) via sulphur atoms with no deprotonation of the carboxylic groups. The STM images show that at low coverage the molecules decorate the Au(111) herringbone reconstruction and form uniform monolayers as the coverage is increased. The energy level alignment of N3 with the Au(111) surface has been constructed using valence band photoemission and N 1s x-ray absorption spectroscopy, illustrating the overlap between the N3 HOMO and the Au valence band. The HOMO, which becomes the site of a hole following photoexcitation in a DSC, is located on the thiocyanate ligands which are here shown to bond via S atoms to the Au surface. This study is fundamental to understanding the use of N3 in a solid state DSC that uses a metallic electrode such as Au to replenish electrons lost by the dye.

8.1 List of publications

- **Resonant photoemission and resonant inelastic x-ray scattering comparative study of charge-transfer dynamics in real solar cell molecules**
James N. O'Shea, Louise C. Mayor, Karina Schulte, A. Pietzsch, and F. Hen-
nies.
Manuscript in preparation, intended for J. Chem. Phys. (2009)
- **Charge transfer of a Ru(II) dye complex on the Au(111) surface: Resonant photoemission and x-ray absorption**
Louise C. Mayor, Graziano Magnano, Christopher J. Satterley, and James O'Shea.
Manuscript in preparation, intended for J. Chem. Phys. (2009)
- **X-ray absorption and photoemission spectroscopy of Zn-protoporphyrin adsorbed on rutile TiO₂(110) prepared by *in situ* electro-spray deposition**
Anna Rienzo, Louise C. Mayor, Graziano Magnano, Christopher J. Satterley,
Evren Ataman, Joachim Schnadt, Karina Schulte, and James N. O'Shea.
Manuscript submitted to Surf. Sci. (2009)
- **Adsorption of a Ru(II) dye complex on the Au(111) surface: Photoemission and scanning tunneling microscopy**
Louise C. Mayor, Alex Saywell, Graziano Magnano, Christopher J. Satterley,
Joachim Schnadt, and James N. O'Shea.
J. Chem. Phys **130**, 164704 (2009)
- **Direct measurement of electrical conductance through a self-assembled molecular layer**
F. Song, J. W. Wells, K. Handrup, Z. S. Li, S. N. Bao, K. Schulte, M. Ahola-
Tuomi, L. C. Mayor, J. C. Swarbrick, E. W. Perkins, L. Gammelgaard, and Ph.
Hofmann.
Nature Nanotechnology **4**, 373 (2009)

- **Photoemission, resonant photoemission, and x-ray absorption of a Ru(II) complex adsorbed on rutile TiO₂(110) prepared by *in situ* electrospray deposition**
Louise C. Mayor, J. Ben Taylor, Graziano Magnano, Anna Rienzo, Christopher J. Satterley, James N. O'Shea, and Joachim Schnadt.
J. Chem. Phys. **129**, 114701 (2008)
- **Molecular damage in bi-isonicotinic acid adsorbed on rutile TiO₂(110)**
James N. O'Shea, J. Ben Taylor, Louise C. Mayor, Janine C. Swarbrick, and Joachim Schnadt.
Surface Science **602** (9), 1693 (2008)
- **Charge-Transfer Dynamics at Model Metal-Organic Solar Cell Surfaces**
J. Ben Taylor, Louise C. Mayor, Janine C. Swarbrick, James N. O'Shea, and Joachim Schnadt.
J. Phys. Chem. C, **111** (44), 16646 (2007)
- **Electrospray deposition of fullerenes in ultra-high vacuum: in situ scanning tunneling microscopy and photoemission spectroscopy**
Christopher J. Satterley, Luís M. A. Perdigão, Alex Saywell, Graziano Magnano, Anna Rienzo, Louise C. Mayor, Vinod R. Dhanak, Peter H. Beton, and James N. O'Shea.
Nanotechnology **18**, 455304 (2007)
- **Adsorption and charge transfer dynamics of bi-isonicotinic acid on Au(111)**
J. Ben Taylor, Louise C. Mayor, Janine C. Swarbrick, James N. O'Shea, Cristina Isvoranu, and Joachim Schnadt.
J. Chem. Phys. **127**, 134707 (2007)

- **Electrospray deposition of carbon nanotubes in vacuum**

James N. O'Shea, John B. Taylor, Janine C. Swarbrick, Graziano Magnano,
Louise C. Mayor and Karina Schulte.

Nanotechnology **18** 035707 (2007)

8.2 List of acronyms

ARR – Auger resonant Raman

BE – binding energy

CASTEP – Cambridge sequential total energy package

DSC – dye-sensitised solar cell

DFT – density functional theory

ESD – electrospray deposition

FWHM – full width at half maximum

GE – grazing emission

GGA – generalised gradient approximation

HOMO – highest occupied molecular orbital

KE – kinetic energy

LUMO – lowest unoccupied molecular orbital

N3 – cis-bis(isothiocyanato)bis(2,2'-bipyridyl-4,4'-dicarboxylato)-ruthenium(II)

NE – normal emission

NEXAFS – near-edge absorption fine structure

PEEK – polyetheretherketone

PES – photoemission spectroscopy

RES – resonant electron spectroscopy

RPES – resonant photoemission spectroscopy

RXES – resonant x-ray emission spectroscopy

SRS – synchrotron radiation source

STM – scanning tunnelling microscopy

UHV – ultra-high vacuum

UV – ultraviolet

XES – x-ray emission spectroscopy

List of Figures

1.1	Spectrum showing the amount of electromagnetic radiation at the top of the earth's atmosphere and at sea level.	3
1.2	Schematic diagram showing the structure of a Grätzel cell and the physical steps by which it absorbs electromagnetic radiation from the sun and transforms it into electrical energy.	5
1.3	a) N ₃ molecule adsorbed on rutile TiO ₂ (110), calculated using CASTEP[8] at the DFT-GGA level (see Section 6.2 for details), and b) chemical structure of the N ₃ molecule.	7
1.4	Incident-photon-to-current efficiency as a function of wavelength for TiO ₂ and N ₃ -sensitised TiO ₂	8
1.5	Schematic figure illustrating the different theories regarding the Au layer in the McFarland and Tang cell.	12
1.6	A dye-sensitised solar cell.[31]	14
2.1	Hubble space telescope image of the M87 galaxy showing synchrotron radiation	17
2.2	Schematic image of a synchrotron,[36] showing the (1) electron gun, (2) linear accelerator, (3) booster ring, (4) storage ring, (5) beamline and (6) end station.	18
2.3	An undulator insertion device. An array of magnets guide electrons in a gently undulating path, causing them to emit forward-pointing radiation.[37]	19
2.4	Schematic figure of the I511 beamline at the MAX-II synchrotron in MAX-lab, Sweden.	21
2.5	Photograph of the I511 beamline at the MAX-II synchrotron in MAX-lab, Sweden.	22
2.6	Photograph of the I511-1 surface science end station.	23
2.7	Schematic figure illustrating that when the synchrotron beam is at (a) grazing incidence to the sample surface, as opposed to (b) normal incidence, the emitted photons and electrons originate from higher up in the sample.	26

3.1	Image of an N3 molecule adsorbed to the rutile TiO ₂ (110) surface, produced from density functional theory calculations which are described in Section 3.5; specific parameters for this particular calculation are given in Section 6.2.	27
3.2	Structure of the (a) TiO ₂ (110) and (b) Au(111) crystal planes.	28
3.3	Definition of terms for bound electrons.	30
3.4	Electronic energy level diagrams depicting the photoemission process for a molecule.	34
3.5	Comparison of Auger yield and fluorescence yield as a function of atomic number. Figure adapted from Reference [40].	35
3.6	Electronic energy level diagrams depicting the shake up and shake off loss processes in photoemission spectroscopy.	36
3.7	Wide scan electron spectrum, taken using photoemission spectroscopy.	38
3.8	High resolution N 1s photoelectron spectrum.	40
3.9	Hemispherical electron analyser.	41
3.10	Photograph showing the Scienta R4000 hemispherical electron analyser used in this work.	42
3.11	Steps to calibrate the binding energy of a photoelectron spectrum.	45
3.12	Universal curve showing the inelastic mean free path of an electron in a solid as a function of its kinetic energy. Figure adapted from Reference [41].	46
3.13	Energy level diagrams depicting the processes involved in NEXAFS spectroscopy for a molecule.	48
3.14	Experimental N 1s NEXAFS spectrum taken for a monolayer of N3 on TiO ₂ . The N 1s core level and a schematic energy level diagram are superimposed, showing that no photoexcitation and subsequent decay events can occur when $h\nu$ is too small, but that when the photon energy is on-resonance, photoexcitation can occur (leading to decay events being detected).	49
3.15	Energy level diagrams depicting the x-ray emission process for a molecule.	51
3.16	N 1s x-ray emission spectrum taken for a multilayer of N3 on TiO ₂ (110). The data was collected on a photon energy scale, and this has been converted to a binding energy scale by referencing to the binding energy of the N 1s core level, and reversing the scale.	52
3.17	Geometry-optimised free N3 molecule showing the HOMO in blue, calculated using CASTEP[8].	54
3.18	Schematic figure of an STM[44].	57
3.19	STM images showing (a) a sub-monolayer and (b) a monolayer of N3 on Au(111).	58

4.1	Part (a) shows valence band photoemission spectra of the clean $\text{TiO}_2(110)$ surface and of a monolayer of N3 adsorbed to this surface, adjacent to a N $1s$ NEXAFS spectrum of the N3 monolayer, converted from a photon energy scale to a binding energy scale. Part (b) shows schematic electronic energy level diagrams to illustrate how the different spectra are related.	62
4.2	Schematic figure to illustrate how a NEXAFS spectrum can be put on a binding energy scale.	63
4.3	Electron excitation and de-excitation processes in resonant electron spectroscopy.	66
4.4	N $1s$ resonant electron spectroscopy data for a multilayer of N3. . . .	69
4.5	Schematic figure identifying the processes behind the different peaks seen in a resonant electron spectrum.	70
4.6	Electron excitation and de-excitation processes in resonant x-ray emission spectroscopy.	76
4.7	Resonant x-ray emission spectra for a monolayer of N3 on TiO_2	78
4.8	Resonant x-ray emission spectra for a multilayer of N3 on TiO_2	79
5.1	Schematic images showing the effect that a positive bias on the electro-spray emitter has on the behaviour of the solution/suspension. . .	83
5.2	Schematic diagram showing the processes which create an electro-spray plume once a jet of droplets has left the emitter.	85
5.3	Photographs showing different versions of entrances to the first differentially pumped chamber.	87
5.4	Schematic illustration of the electro-spray system showing the molecular beam travelling from left to right as it leaves the high voltage emitter, passes via conical apertures through differentially pumped chambers, and is incident upon the sample.	88
5.5	Photograph of the first configuration of electro-spray apparatus used in this work, attached to an end station at beamline 5u1 at Daresbury SRS, UK.	90
6.1	a) N3 molecule adsorbed on rutile $\text{TiO}_2(110)$, calculated using CASTEP[8] at the DFT-GGA level (see Section 6.2 for details), and b) chemical structure of the N3 molecule.	92
6.2	Photographs showing a TiO_2 substrate clamped using Ta to a Si crystal. . .	95
6.3	O $1s$ core-level spectra measured using $h\nu = 600$ eV.	98
6.4	S $2p$ core-level spectra measured using $h\nu = 225$ eV.	100
6.5	C $1s$ core-level spectrum measured using $h\nu = 350$ eV.	101
6.6	N $1s$ core-level spectrum measured using $h\nu = 500$ eV.	102

6.7	Valence band PES spectra of the clean substrate and of a monolayer of N3, adjacent to a N 1s NEXAFS spectrum of the N3 monolayer. The NEXAFS spectrum is also shown shifted by -1.6 eV to align with the optical HOMO-LUMO gap of 2.3 eV.	103
6.8	N 1s RES data for the N3 multilayer.	106
6.9	N 1s RES data for the N3/TiO ₂ monolayer.	107
6.10	N 1s RES and N 1s NEXAFS spectra of the N3 (a) multilayer and (b) monolayer.	108
6.11	Photon energy slices of the multilayer RPES data shown in Figure 6.8 taken at pre-edge, LUMO and LUMO+1 photon energies, to give a clearer view of the misaligned peaks.	111
6.12	Peaks from the RPES monolayer and multilayer data as defined in Figure 6.11, where each peak has been integrated over the extent of its BE range.	112
6.13	DFT calculations showing electron orbitals (dark blue) of a geometry-optimised free N3 molecule. The calculated orbitals are identified with the HOMO, LUMO and LUMO+1. Since the molecule is symmetrical, the orbitals shown here on one ligand only are also present on the corresponding symmetrical ligands, and have only marginally different calculated energies. The atoms are coloured by element, with the colours as defined in Figure 1.3.	114
6.14	N 1s NEXAFS spectrum of the N3 multilayer, with a photon energy resolution of ~ 1 eV. The spectrum is here analysed as a preliminary step in choosing appropriate photon energies to perform RXES. . . .	116
6.15	N 1s resonant x-ray emission spectra taken at the LUMO resonance using $h\nu = 398.85$ eV for monolayers and multilayers of N3 on TiO ₂	117
6.16	N 1s resonant x-ray emission spectra taken at the LUMO+1 resonance using $h\nu = 400.15$ eV for monolayers and multilayers of N3 on TiO ₂	119
6.17	RXES spectra taken of the clean TiO ₂ surface using $h\nu = 398.85$ eV and $h\nu = 400.15$ eV.	120
7.1	Valence band photoemission spectra of clean Au, and of low and high coverages of N3 on Au, measured using $h\nu = 110$ eV.	125
7.2	O 1s core-level photoemission spectra measured using $h\nu = 620$ eV. . . .	127
7.3	S 2p core-level photoemission spectra measured using $h\nu = 220$ eV. . . .	128
7.4	S 2p core-level photoemission spectra comparing normal and grazing emission, measured using $h\nu = 220$ eV.	130
7.5	N 1s core-level photoemission spectra measured using $h\nu = 500$ eV. . . .	131
7.6	C 1s core-level photoemission spectra measured using $h\nu = 380$ eV. . . .	132
7.7	STM images of N3 deposited onto the mica-supported Au(111) reconstruction.	135

7.8	Valence band PES spectra of the clean Au substrate, a low coverage of N3 and a high coverage of N3, adjacent to a N 1s NEXAFS spectrum of the low N3 coverage.	137
7.9	N 1s RES and N 1s NEXAFS spectra of the N3 (a) multilayer (on TiO ₂) and (b) low coverage on Au.	139

References

- [1] M. Grätzel. Photovoltaic and photoelectrochemical conversion of solar energy. *Phil. Trans. R. Soc.*, 365:993, 2007.
- [2] M. Grätzel. Photoelectrochemical cells. *Nature*, 414:338, 2001.
- [3] The curves are based on the American Society for Testing and Materials (ASTM) Terrestrial Reference Spectra, which are standard test conditions used by the photovoltaics industry.
- [4] Author: Nick84. Wikimedia commons. http://commons.wikimedia.org/wiki/File:Solar_spectrum_ita.svg, July 2009.
- [5] Titanium dioxide - wikipedia, the free encyclopedia. http://en.wikipedia.org/wiki/Titanium_dioxide, August 2009.
- [6] W. West. First hundred years of spectral sensitization. Proc. Vogel Cent. Symp. *Photogr. Sci. Eng.*, 18:35, 1974.
- [7] B. O'Regan and M. Grätzel. A low-cost, high-efficiency solar cell based on dye-sensitized colloidal TiO₂ films. *Nature*, 353:737, 1991.
- [8] M. D. Segall, P. J. D. Lindan, M. J. Probert, C. J. Pickard, P. J. Hasnip, S. J. Clark, and M. C. Payne. First-principles simulation: ideas, illustrations and the CASTEP code. *J. Phys. Cond. Matt.*, 14:2717, 2002.
- [9] M. Grätzel. Conversion of sunlight to electric power by nanocrystalline dye-sensitized solar cells. *J. Photochem. Photobiol. A*, 164:3, 2004.

- [10] M. K. Nazeeruddin, A. Kay, I. Rodicio, R. Humphry-Baker, E. Müller, P. Liska, N. Vlachopoulos, and M. Grätzel. Conversion of Light to Electricity by cis-X₂Bis(2,2'-bipyridyl-4,4'-dicarboxylate)ruthenium(II) Charge-Transfer Sensitizers (X = Cl⁻, Br⁻, I⁻, CN⁻, and SCN⁻) on Nanocrystalline TiO₂ Electrodes. *J. Am. Chem. Soc.*, 115:6382, 1993.
- [11] M. K. Nazeeruddin, P. Pechy, T. Renouard, S. M. Zakeeruddin, R. Humphry-Baker, P. Comte, P. Liska, L. Cevey, E. Costa, V. Shklover, L. Spiccia, G. B. Deacon, C. A. Bignozzi, and M. Grätzel. Engineering of Efficient Panchromatic Sensitizers for Nanocrystalline TiO₂-Based Solar Cells. *J. Am. Chem. Soc.*, 123:1613, 2001.
- [12] H. Tsubomura, M. Matsumura, Y. Noyamaura, and T. Amamiya. Dye sensitized zinc oxide: aqueous electrolyte: platinum photocell. *Nature*, 261:402, 1976.
- [13] M. Grätzel. Solar Energy Conversion by Dye-Sensitized Solar Cells. *Inorg. Chem.*, 44:6841, 2005.
- [14] M. Matsumura. *PhD thesis*. Osaka University, Japan, 1979.
- [15] L. Patthey, H. Rensmo, P. Persson, K. Westermark, L. Vayssieres, A. Stashans, Å. Petersson, P. A. Brühwiler, H. Siegbahn, S. Lunell, and N. Mårtensson. Adsorption of bi-isonicotinic acid on rutile TiO₂(110). *J. Chem. Phys.*, 110:5913, 1999.
- [16] A. Thomas, W. Flavell, C. Chatwin, S. Rayner, D. Tsoutsou, A. Kumarasinghe, D. Brete, T. Johal, S. Patel, and J. Purton. Adsorption of bi-isonicotinic acid on anatase TiO₂(101) and (001) studied by photoemission and NEXAFS spectroscopy. *Surf. Sci.*, 592:159, 2005.
- [17] D.Č. Cronmeyer. Electrical and Optical Properties of Rutile Single Crystals. *Phys. Rev.*, 87:876, 1952.

- [18] P. Wang, B. Wenger, R. Humphry-Baker, J. E. Moser, J. Teuscher, W. Kantlehner, J. Mezger, E. V. Stoyanov, S. M. Zakeeruddin, and M. Grätzel. Charge separation and efficient light energy conversion in sensitized mesoscopic photoelectrochemical cells based on binary ionic liquids. *J. Am. Chem. Soc.*, 127:6850, 2005.
- [19] S. A. Haque, E. Palomares, H. M. Upadhyaya, L. Otley, R. J. Potter, A. B. Holmes, and J. R. Durrant. Flexible dye sensitised nanocrystalline semiconductor solar cells. *Chem. Commun.*, 24:3008, 2003.
- [20] U. Bach, D. Lupo, P. Comte, J. E. Moser, F. Weissörtel, J. Salbeck, H. Spreitzer, and M. Grätzel. Solid state dye sensitized mesoporous TiO₂ solar cells with high photon-to-current conversion efficiencies. *Nature*, 395:583, 1998.
- [21] B. O'Regan and D. T. Schwartz. Solid state photoelectrochemical cells based on dye sensitization. *AIP Conf. Proc.*, 404:129, 1997.
- [22] V. P. S. Perera, P. K. D. D. P. Pitigala, P. V. V. Jayaweera, K. M. P. Bandaranayake, and K. Tennakone. Dye-sensitized solid-state photovoltaic cells based on dye multilayersemiconductor nanostructures. *J. Phys. Chem. B*, 107:13758, 2003.
- [23] M. Grätzel. Dye-sensitized solar cells. *J. Photochem. Photobiol. C*, 4:145, 2003.
- [24] E. W. McFarland and J. Tang. A photovoltaic device structure based on internal electron emission. *Nature*, 421:616, 2003.
- [25] M. Grätzel. Applied physics: Solar cells to dye for. *Nature*, 421:586, 2003.
- [26] L. Zhang, R. Persaud, and T. E. Madey. Ultrathin metal films on a metal oxide surface: Growth of Au on TiO₂ (110). *Phys. Rev. B*, 56:10549, 1997.
- [27] T. Minato, T. Susaki, S. Shiraki, H. S. Kato, M. Kawai, and K. Aika. Investigation of the electronic interaction between TiO₂(110) surfaces and Au clusters by PES and STM. *Surf. Sci.*, 566:1012, 2004.

- [28] T. Okazawa, M. Kohyama, and Y. Kido. Electronic properties of Au nanoparticles supported on stoichiometric and reduced TiO₂(110) substrates. *Surf. Sci.*, 600:4430, 2006.
- [29] R. Koole, O. Liljeroth, S. Oosterhout, and D. Vanmaekelbergh. Chemisorption determines the photovoltage of a Ti/TiO₂/Au/Dye internal electron emission photovoltaic cell. *J. Phys. Chem. B.*, 109:9205, 2005.
- [30] C. H. Henry. Limiting efficiencies of ideal single and multiple energy gap terrestrial solar cells. *J. Appl. Phys.*, 51:4494, 1980.
- [31] John P. Algae technology makes solar cells 3x as efficient. <http://www.celsias.com/article/algae-technology-makes-solar-cells-3x-efficient/>, August 2009.
- [32] Toyota. Toyota dream house papi. <https://toyotahome-net.com/papi/tur/index.html>, August 2009.
- [33] K. Zweibel. The terawatt challenge for thin-film PV. *Technical Report NREL/TP-52038350*, 2005.
- [34] STScI. Hubblesite - newscenter - a cosmic searchlight (07/06/2000) - release images. http://hubblesite.org/newscenter/archive/releases/2000/20/image/a/format/large_web/, July 2009.
- [35] David Attwood. *Soft X-rays and Extreme Ultraviolet Radiation – Principles and Applications*. Cambridge University Press, Cambridge, 2007.
- [36] Author: ‘Synchrotron’. Wikipedia. http://en.wikipedia.org/wiki/File:Australian_Synchrotron_schema.jpg, July 2009.
- [37] Hasylab. <http://hasylab.desy.de>, January 2009.
- [38] R. Denecke, P. Vaterlein, M. Bassler, N. Wassdahl, S. Butorin, A. Nilsson, J. E. Rubensson, J. Nordgren, N. Mårtensson, and R. Nyholm. Beamline I511 at MAX II, capabilities and performance. *J. Elec. Spec. Rel. Phen.*, 101-103:971, 1999.

- [39] E. Bequerel. Recherches sur les effets de la radiation chimique de la lumière solaire, au moyen des courants électriques. *C. R. Acad. Sci.*, 9:145, 1839.
- [40] <http://en.wikipedia.org/wiki/User:Slashme> David Richfield. Wikimedia commons. [http://en.wikipedia.org/wiki/File:Auger_Yield .svg](http://en.wikipedia.org/wiki/File:Auger_Yield.svg), January 2009.
- [41] M. P. Seah and W. A. Dench. Quantitative electron spectroscopy of surfaces: A standard data base for electron inelastic mean free paths in solids. *Surf. Interface Anal.*, 1:2, 1979.
- [42] A. Nilsson. X-ray emission studies of adsorbates. *J. Elec. Spec. Rel. Phen.*, 93:143–152, 1998.
- [43] K. Capelle. A Bird’s-Eye View of Density-Functional Theory (Version 5). *cond-mat*, page 0211443, 2006.
- [44] Michael Schmid. Wikimedia commons. http://en.wikipedia.org/wiki/File:ScanningTunnelingMicroscope_schematic.png, January 2009.
- [45] J. Schnadt, J. Schiessling, and P.A. Brühwiler. Comparison of the size of excitonic effects in molecular π systems as measured by core and valence spectroscopies. *Chem. Phys.*, 312:39, 2005.
- [46] J. Schnadt, J. N. O’Shea, L. Patthey, J. Krempaský, N. Mårtensson, and P. A. Brühwiler. Alignment of valence photoemission, x-ray absorption, and substrate density of states for an adsorbate on a semiconductor surface. *Phys. Rev. B*, 67:235420, 2003.
- [47] P. A. Brühwiler, O. Karis, and N. Mårtensson. Charge-transfer dynamics studied using resonant core spectroscopies. *Rev. Mod. Phys.*, 74:703, 2002.
- [48] W. Wurth and D. Menzel. Ultrafast Electron Dynamics at Surfaces Probed by Resonant Auger Spectroscopy. *Chem. Phys.*, 251:141, 2000.

- [49] B. B. Smith and A. J. Nozik. A Wave Packet Model for Electron Transfer and Its Implications for the Semiconductor-Liquid Interface. *J. Phys. Chem. B*, 103:9915, 1999.
- [50] C. O. Almbladh. Effects of incomplete phonon relaxation on x-ray emission edges in simple metals. *Phys. Rev. B*, 16:4343, 1977.
- [51] G. D. Mahan. Emission spectra and phonon relaxation. *Phys. Rev. B*, 15:4587, 1977.
- [52] C. O. Almbladh, A. L. Morales, and G. Grossmann. Theory of Auger core-valence-valence processes in simple metals. I. Total yields and core-level lifetime widths. *Phys. Rev. B*, 39:3489, 1989.
- [53] J. B. Fenn, M. Mann, C. K. Meng, S. F. Wong, and C. M. Whitehouse. Electrospray ionization for mass spectrometry of large biomolecules. *Science*, 246:64, 1989.
- [54] C. M. Whitehouse, R. N. Dreyer, M. Yamashita, and J. B. Fenn. Electrospray interface for liquid chromatographs and mass spectrometers. *Anal. Chem.*, 57:675, 1985.
- [55] The Nobel Foundation. Nobelprize.org – chemistry 2002. http://nobelprize.org/nobel_prizes/chemistry/laureates/2002/, July 2009.
- [56] J. B. Fenn, M. Mann, C. K. Meng, S. F. Wong, and C. M. Whitehouse. Electrospray ionization for mass-spectrometry of large biomolecules. *Science*, 246:64, 1989.
- [57] A. Jaworek. Electrospray droplet sources for thin film deposition. *J. Mater. Sci.*, 42:266, 2007.
- [58] M. Knudsen. Die Gesetze der Molekularströmung und der inneren Reibungsströmung der Gase durch Röhren. *Annalen der Physik*, 333:75, 1908.

- [59] M. Knudsen. Experimentelle Bestimmung des Druckes gesättigter Quecksilberdämpfe bei 0° und höheren Temperaturen. *Annalen der Physik*, 334:179, 1909.
- [60] J. N. O'Shea, J. B. Taylor, J. C. Swarbrick, G. Magnano, L. C. Mayor, and K. Schulte. Electrospray deposition of carbon nanotubes in vacuum. *Nanotechnology*, 18:035707, 2007.
- [61] C. J. Satterley, L. M. A. Perdigão, A. Saywell, G. Magnano, A. Rienzo, L. C. Mayor, V. R. Dhanak, P. H. Beton, and J. N. O'Shea. Electrospray deposition of fullerenes in ultra-high vacuum: in situ scanning tunneling microscopy and photoemission spectroscopy. *Nanotechnology*, 18:455304, 2007.
- [62] A. Saywell, G. Magnano, C. J. Satterley, L. M. A. Perdigão, N. R. Champness, P. H. Beton, and J. N. O'Shea. Electrospray Deposition of C60 on a Hydrogen-Bonded Supramolecular Network. *J. Phys. Chem. C*, 2008.
- [63] A. Rienzo, L. C. Mayor, G. Magnano, C. J. Satterley, E. Ataman, J. Schnadt, K. Schulte, and J. N. O'Shea. X-ray absorption and photoemission spectroscopy of Zn-protoporphyrin adsorbed on rutile $\text{TiO}_2(110)$ prepared by *in situ* electro-spray deposition. *Manuscript submitted to Surf. Sci*, 2009.
- [64] Manuscript in preparation.
- [65] L. C. Mayor, J. B. Taylor, G. Magnano, A. Rienzo, C. J. Satterley, J. N. O'Shea, and J. Schnadt. Photoemission, resonant photoemission, and x-ray absorption of a Ru(II) complex adsorbed on rutile $\text{TiO}_2(110)$ prepared by in situ electro-spray deposition. *J. Chem. Phys.*, 129:114701, 2008.
- [66] L. C. Mayor, A. Saywell, G. Magnano, C. J. Satterley, J. Schnadt, and J. N. O'Shea. Adsorption of a Ru(II) dye complex on the Au(111) surface: Photoemission, and scanning tunneling microscopy. *J. Chem. Phys.*, 130:164704, 2009.

- [67] A. M. Gañán-Calvo. Cone-jet analytical extension of Taylor's electrostatic solution and the asymptotic universal scaling laws in electrospraying. *Phys. Rev. Lett.*, 79:217, 1997.
- [68] H. Rensmo, S. Södergren, L. Patthey, K. Westermark, L. Vayssieres, O. Kohle, P.A. Brühwiler, A. Hagfeldt, and H. Siegbahn. The electronic structure of the cis-bis(4,4'-dicarboxy-2,2'-bipyridine)-bis(isothiocyanato) ruthenium(II) complex and its ligand 2,2'-bipyridyl-4,4'-dicarboxylic acid studied with electron spectroscopy. *Chem. Phys. Lett.*, 274:51, 1997.
- [69] H. Rensmo, K. Westermark, S. Södergren, O. Kohle, P. Persson, S. Lunell, and H. Siegbahn. XPS studies of Ru-polypyridine complexes for solar cell applications. *J. Chem. Phys.*, 111:2744, 1999.
- [70] E. M. J. Johansson, M. Hedlund, H. Siegbahn, and H. Rensmo. Electronic and Molecular Surface Structure of Ru(tcterpy)(NCS)₃ and Ru(dcbpy)₂(NCS)₂ Adsorbed from Solution onto Nanostructured TiO₂: A Photoelectron Spectroscopy Study. *J. Phys. Chem. B*, 109:22256, 2005.
- [71] R. J. Ellingson, J. B. Asbury, S. Ferrere, H. N. Ghosh, J. R. Sprague, T. Lian, and A. J. Nozik. Dynamics of Electron Injection in Nanocrystalline Titanium Dioxide Films Sensitized with [Ru(4,4'-dicarboxy-2,2'-bipyridine)₂(NCS)₂] by Infrared Transient Absorption. *J. Phys. Chem. B*, 102:6455, 1998.
- [72] P. Mylperkiö, G. Benkö, J. Korppi-Tommola, A. P. Yartsev, and V. Sundström. A study of electron transfer in Ru(dcbpy)₂(NCS)₂ sensitized nanocrystalline TiO₂ and SnO₂ films induced by red-wing excitation. *Phys. Chem. Chem. Phys.*, 10:996, 2008.
- [73] S. Wendt, R. Schaub, J. Matthiesen, E.K. Vestergaard, E. Wahlström, M.D. Rasmussen, P. Thostrup, L.M. Molina, E. Lgsgaard, I. Stensgaard, B. Hammer, and F. Besenbacher. Oxygen vacancies on TiO₂(110) and their interaction with H₂O and O₂: A combined high-resolution STM and DFT study. *Surf. Sci.*, 598:226, 2005.

- [74] U. Diebold. The surface science of titanium dioxide. *Surf. Sci. Rep.*, 48:53, 2003.
- [75] J. Schnadt, J. N. O'Shea, L. Patthey, J. Schiessling, J. Krempaský, M. Shi, N. Mårtensson, and P. A. Brühwiler. Structural study of adsorption of isonicotinic acid and related molecules on rutile TiO₂(110) II: XPS. *Surf. Sci.*, 544:74, 2003.
- [76] The Broyden-Fletcher-Goldfarb-Shanno method is a method to solve an unconstrained nonlinear optimisation problem. See for example Reference [101].
- [77] J. Schnadt, J. Schiessling, J. N. O'Shea, S. M. Gray, L. Patthey, M. K. J. Johansson, M. Shi, J. Krempaský, J. Åhlund, P. G. Karlsson, P. Persson, N. Mårtensson, and P. A. Brühwiler. Structural study of adsorption of isonicotinic acid and related molecules on rutile TiO₂(110) I: XAS and STM. *Surf. Sci.*, 540:39, 2003.
- [78] J. N. O'Shea, Y. Luo, J. Schnadt, L. Patthey, H. Hilleheimer, J. Krempaský, D. Nordlund, M. Nagasono, and N. Mårtensson. Hydrogen-bond induced surface core-level shift in pyridine carboxylic acids. *Surf. Sci.*, 486:157, 2001.
- [79] J. N. O'Shea, J. Schnadt, P. A. Brühwiler, H. Hilleheimer, N. Mårtensson, L. Patthey, J. Krempaský, C. Wang, Y. Luo, and H. Ågren. Hydrogen-Bond Induced Surface Core-Level Shift in Isonicotinic Acid. *J. Phys. Chem. B.*, 105:1917, 2001.
- [80] J. N. O'Shea, J. C. Swarbrick, K. Nilson, C. Puglia, B. Brena, Y. Luo, and V. R. Dhanak. Molecular ordering in isonicotinic acid on rutile TiO₂(110) investigated with valence band photoemission. *J. Chem. Phys.*, 121:10203, 2004.
- [81] Albert C. Thompson, David T. Attwood, Eric M. Gullikson, Malcolm R. Howells, Jeffrey B. Kortright, Arthur L. Robinson, James H. Underwood, Kwang-Je Kim, Janos Kirz, Ingolf Lindau, Piero Pianetta, Herman Winick, Gwyn P. Williams, James H. Scofield, and Douglas Vaughan. *Centre for X-ray Optics*

- Advanced Light Source - X-ray Data Booklet*. Lawrence Berkeley National Laboratory, California, 2001.
- [82] M. Grätzel and A. Hagfeldt. Molecular Photovoltaics. *Acc. Chem. Res.*, 33:269, 2000.
- [83] J. N. O'Shea, J. B. Taylor, L. C. Mayor, J. C. Swarbrick, and J. Schnadt. Molecular damage in bi-isonicotinic acid. *Surf. Sci. In press*, 2008.
- [84] J. C. Fuggle and N. Mårtensson. Core-Level Binding Energies in Metals. *J. Elec. Spec. Rel. Phen.*, 21:275, 1980.
- [85] J. B. Taylor, L. C. Mayor, J. C. Swarbrick, J. N. O'Shea, C. Isvoranu, and J. Schnadt. Adsorption and charge transfer dynamics of bi-isonicotinic acid on Au(111). *J. Chem. Phys.*, 127:134707, 2007.
- [86] J. B. Taylor, L. C. Mayor, J. C. Swarbrick, J. N. O'Shea, and J. Schnadt. Charge-Transfer Dynamics at Model Metal-Organic Solar Cell Surfaces. *J. Phys. Chem. C*, 111:16646, 2007.
- [87] J. Schnadt, P. A. Brühwiler, L. Patthey, J. N. O'Shea, S. Södergren, M. Odelius, R. Ahuja, O. Karis, M. Bäessler, P. Persson, H. Siegbahn, S. Lunell, and N. Mårtensson. Experimental evidence for sub-3-fs charge transfer from an aromatic adsorbate to a semiconductor. *Nature*, 418:620, 2002.
- [88] J. Schnadt, J. N. O'Shea, L. Patthey, L. Kjeldgaard, J. Åhlund, K. Nilsson, J. Schiessling, J. Krempaský, M. Shi, O. Karis, C. Glover, H. Siegbahn, N. Mårtensson, and P. A. Brühwiler. Excited-state charge transfer dynamics in systems of aromatic adsorbates on TiO₂ studied with resonant core techniques. *J. Chem. Phys.*, 119:12462, 2003.
- [89] P. Persson, S. Lunell, P. A. Brühwiler, J. Schnadt, S. Södergren, J. N. O'Shea, O. Karis, H. Siegbahn, N. Mårtensson, M. Bäessler, and L. Patthey. N1s x-ray absorption study of the bonding interaction of bi-isonicotinic acid adsorbed on rutile TiO₂(110). *J. Chem. Phys.*, 112:3945, 2000.

- [90] P. Myllyperkiö, G. Benkö, J. E. I. Korppi-Tommola, A. P. Yartsev, and V. Sundström. A study of electron transfer in Ru(dcbpy)₂(NCS)₂ sensitized nanocrystalline TiO₂ and SnO₂ films induced by red-wing excitation. *Phys. Chem. Chem. Phys.*, 10:996, 2007.
- [91] B. Kempgens, A. Kivimäki, M. Neeb, H. M. Köppe, A. M. Bradshaw, and J. Feldhaus. A high resolution N 1s photoionisation study of the N₂ molecule in the near-threshold region. *J. Phys. B*, 29:5389, 1996.
- [92] M. Coville and T. D. Thomas. Molecular effects on inner-shell lifetimes: Possible test of the one-center model of Auger decay. *Phys. Rev. A*, 43:6053, 1991.
- [93] K. Westermark, H. Rensmo, J. Schnadt, P. Persson, S. Södergren, P.A. Brühwiler, S. Lunell, and H. Siegbahn. Electron dynamics within Ru-2,20-bipyridine complexes an N1s core level excitation study. *Chem. Phys.*, 285:167, 2002.
- [94] J. A. D. Matthew and Y. Komninos. Transition rates for interatomic Auger processes. *Surf. Sci.*, 53:716, 1975.
- [95] H. Rensmo, S. Lunell, and H. Siegbahn. Absorption and electrochemical properties of ruthenium(II) dyes, studied by semiempirical quantum chemical calculations. *J. Photochem. Photobiol. A*, 114:117, 1998.
- [96] G.J. Kluth, C. Carraro, and R. Maboudian. Direct Observation of Sulfur Dimers in Alkanethiol Self-Assembled Monolayers on Au. *Phys. Rev. B.Science*, 59:R10449, 1999.
- [97] P. Fenter, A. Eberhardt, and P. Eisenberger. Self-Assembly of n-Alkyl Thiols as Disulfides on Au(111). *Science*, 266:1216, 1994.
- [98] I. Horcas, R. Fernandez, J.M. Gomez-Rodriguez, J. Colchero, J. Gomez-Herrero, and A.M. Baro. WSXM: A software for scanning probe microscopy and a tool for nanotechnology. *Rev. Sci. Instrum.*, 78:013705, 2007.

- [99] J. V. Barth, H. Brune, G. Ertl, and R. J. Behm. Scanning tunneling microscopy observations on the reconstructed Au(111) surface - atomic structure, long-range superstructure, rotational domains, and surface-defects. *J. Phys. Rev. B.*, 42:9307, 1990.
- [100] J. A. Rodriguez, J. Dvorak, T. Jirsak, G. Liu, J. Hrbek, Y. Aray, and C. González. Coverage Effects and the Nature of the Metal-Sulfur Bond in S/Au(111): High-Resolution Photoemission and Density-Functional Studies. *J. Phys. Rev. B.*, 42:9307, 1990.
- [101] J. Nocedal and S. J. Wright. *Numerical Optimization (2nd ed.)*. Springer-Verlag, Berlin, New York, 2006.